Wideband Reconfigurable Intelligent Surfaces

by

Jalaledin Tayebpour

A thesis
presented to the University of Waterloo
in fulfillment of the
thesis requirement for the degree of
Doctor of Philosophy
in
Electrical Engineering

Waterloo, Ontario, Canada, 2025

© Jalaledin Tayebpour

Examining Committee Membership

The following served on the Examining Committee for this thesis. The decision of the Examining Committee is by majority vote.

External Examiner:	Sean Victor Hum Professor, Dept.of Electrical and Computer Engineering, University of Toronto
Supervisor:	Raafat R.Mansour Professor, Dept. of Electrical and Computer Engineering, University of Waterloo
Internal Member:	Slim Boumaiza Professor, Dept. of Electrical and Computer Engineering, University of Waterloo
Internal Member:	Omar M.Ramahi Professor, Dept. of Electrical and Computer Engineering, University of Waterloo

Internal-External Member: Eihab Abdel-rahman

Professor, Dept. of System Design Engineering, University of Waterloo

Author's Declaration

I hereby declare that I am the sole author of this thesis. This is a true copy of the thesis, including any required final revisions, as accepted by my examiners.

I understand that my thesis may be made electronically available to the public.

Abstract

Reconfigurable intelligent surfaces (RISs) have emerged as one of the most significant innovations in wireless communications, offering a novel approach to meeting the escalating demand for higher data rates, seamless coverage, and energy-efficient connectivity in next-generation networks. Unlike conventional wireless systems that rely on active and power-hungry components, RIS leverages nearly passive reflecting elements arranged in a planar array, whose electromagnetic responses can be dynamically reconfigured. By enabling programmable control over the incident wavefront, RIS introduces a new paradigm in which the wireless environment itself becomes a controllable entity. This capability not only enhances system performance but also reduces overall power consumption and hardware complexity, positioning RIS as a key enabler for sixth-generation (6G) and beyond communication technologies.

This thesis provides a comprehensive investigation into the principles, design methodologies, and system-level benefits of RIS technology. The research begins with an in-depth review of the current state of the art, highlighting both theoretical foundations and practical implementations of RIS. Building on this foundation, the work develops novel design strategies for reconfigurable unit cells intended for RIS applications. Several geometries are explored with the goal of achieving tunable reflection phase profiles, wide operational bandwidth, and multi-polarization capability. The designs integrate semiconductor switches and micro-electromechanical systems (MEMS) actuators, demonstrating the feasibility of programmable reconfigurability while addressing practical fabrication challenges .

To validate the proposed concepts, the designed unit cells are extended into array structures, where their performance is evaluated through both simulation and experimental testing. A practical prototype of a 1-bit reflectarray is fabricated and tested in an anechoic

antenna chamber. The prototype demonstrates the key required functionalities, including beam steering, wideband operation, and dual-polarization control. These results confirm the potential of RIS to dynamically manipulate electromagnetic propagation in real-world scenarios. Furthermore, the thesis addresses critical implementation issues related to the scalability of RIS, the integration of control circuitry, and the trade-offs between design complexity and achievable performance.

The findings presented in this research underscore the innovative role of RIS in reshaping the architecture of wireless communication systems. By turning the propagation environment into an intelligent and programmable medium, RIS has the potential to significantly improve spectral efficiency, energy utilization, and overall network adaptability. The contributions of this thesis extend the understanding of RIS operation, provide novel unit cell structures, and deliver practical insights for prototyping and implementation. In doing so, this work not only advances academic knowledge in the field but also offers practical guidelines for industrial adoption of RIS in future wireless systems. Ultimately, this research highlights the promise of RIS as a cornerstone technology for realizing the vision of 6G and beyond.

Acknowledgments

I would like to thank professor Raafat Mansour for giving me the opportunity to work as a PhD student in his research group. We spent tremendous amount of time discussing various aspects of the research projects together. I am grateful for his patience and interest to advise me from the first day of my PhD program when I was hesitant coping with challenges, to the day of my defense when I was confident about my achievements. He always played a key role to inspire me during this time.

I would like to appreciate professor Slim Boumaiza, professor Omar Ramahi, professor Eihab Abdel-rahman and professor Sean Victor Hum for serving as committee members for my PhD defense, reviewing my thesis and providing valuable feedback. During the PhD program that was the most enjoyable time in my life I had the pleasure of having a great group of colleagues in the CIRFE lab. I would like to thank all of them.

I am thankful to our lab manger, Dr. Luis Gutierrez for mentoring me on using various equipment within the CIRFE lab. He was always available when I requested for help. I would like to extend my appreciation to staff members of ECE department for their great supports.

Dedication

This thesis is dedicated to my wife and my son, whose love and encouragement sustained me, and to my parents, whose sacrifices and constant support made this journey possible.

Table of Contents

Examining Committee ii

Author's Declaration iv

Abstract v

Acknowledgments vii

Dedication viii

List of Figures xiii

List of Tables xviii

1 Introduction 1

1.1 Motivation 1

1.2 Objectives 5

1.3 Thesis Outline 6

2 Literature Review **8**

2.1 Introduction 8

2.2 Reconfigurable Intelligent Surfaces 9

2.2.1 Engineered surfaces and the generalized law of reflection and refraction 9

2.2.2 Metasurfaces: Definition and Applications 12

2.2.3 From Metasurfaces to Reconfigurable Intelligent Surfaces 13

2.2.4 Functionalities of RIS: Beyond Passive Reflection 14

2.3 Recent Advancements in RIS Design 17

2.3.1 Beamforming applications 17

2.3.2 Anomalous reflection 21

2.4 Summary 24

3 Design Methodology of Reconfigurable Intelligent Surfaces (RISs) **26**

3.1 Introduction 26

3.2 RIS Design for Beamforming Applications 27

3.2.1 Ray optic approach 27

3.2.2 1-bit array design 31

3.2.3 Wave optic approach 32

3.3 RIS Design for Anomalous Reflection Applications 35

4 Reconfigurable Arrays Using Semiconductor Switches **40**

4.1 Introduction 40

4.2 Wideband Dual-Polarized RRA Design 41

4.2.1 Primary proposed structure 44

4.2.2 Modified proposed structure 54

4.3 Wideband Dual-Polarized RTA Design 69

4.3.1 Unit cell design 70

4.3.2 Array simulation 76

4.4 Conclusion 77

5 Reconfigurable Arrays Using MEMS Actuator **80**

5.1 Introduction 80

5.2 Unit Cell Design Using MEMS Actuators 81

5.3 The Proposed Unit Cell Structure 83

5.3.1 Design and simulation 83

5.3.2 Fabrication and Measurement 89

5.4 Array Simulation 92

5.5 Discussion and Conclusion 95

6 Conclusion and Future Work **99**

6.1 Conclusion 99

6.2 Future Work 101
6.2.1 New unit cell structure design and development 101
6.2.2 Higher order phase quantization and analog control 102
6.2.3 Fabrication and measurement of the transmitarray (RTA) 102
6.2.4 Scaling to larger apertures and anomalous reflection 102
6.2.5 Fabrication of MEMS based arrays 102
6.2.6 Application driven demonstrations 103

References **104**

List of Figures

1.1 The evolution of cellular networks toward 6G [6]. 3

1.2 RIS application in the next generation of wireless system. [11]. 4

2.1 Application of RIS in a smart radio environment. [14]. 10

2.2 Classification of periodic planar structures [17]. 12

2.3 Different functionalities of reflective/refractive structures [14]. 15

2.4 Two key functions of RIS. (a) Anomalous reflection (b) Beamforming [11]. 17

2.5 The proposed unit cell using a varactor diode in [38]. 19

2.6 (a) Proposed structure in [42]. (b) Proposed unit cell using MEMS switches in [44]. 20

2.7 The proposed 2-bit unit cell in [46]. 21

2.8 (a) Proposed RIS in [48]. (b) Proposed RIS in [49]. 22

2.9 (a) Proposed RIS by NTT DOCOMO in [50]. (b) Proposed RIS in [52]. . . 23

2.10 (a) 1-bit array implemented in [54]. (b) 2-bit array proposed in [55]. 25

3.1 Two main perspective in reflective surface design. (a) Ray optics. (b) Wave optic. [11]. 28

3.2 Geometry of reflectarray with source position 29

3.3 Required phase distributions for two directions. (a) $(\theta_0, \phi_0) = (0°, 0°)$. (b) $(\theta_0, \phi_0) = (30°, 0°)$. 30

3.4 Required quantized phase distributions for two directions. (a) $(\theta_0, \phi_0) = (0°, 0°)$. (b) $(\theta_0, \phi_0) = (30°, 0°)$. 32

3.5 Geometry of reflectarray with a horn antenna source [29]. 33

3.6 The 1-bit array structure illuminated with a plane wave source. 35

3.7 Different phase distributions over the array surface with corresponding radiation pattern. 38

3.8 Single-beam radiation and beam steering obtained by applying different patterns on a 2-bit array. 39

4.1 The electric field distribution of the patch dominant modes. 44

4.2 (a). The square patch unit cell with two excitation mechanism. (b) Field distribution of each mode with and without the other mode excitation mechanism. (c) Reflection magnitude/phase under y-polarized incident wave (related to TM_{01}). (d) Reflection magnitude/phase under x-polarized incident wave (related to TM_{10}). 46

4.3 (a) The process of achieving two states. (b) Incident and reflected waves in two states for both polarizations. 47

4.4 The proposed unit cell structure. (a) 3-D view. (b) Layer description . . . 49

4.5 (a) S-parameters of the proposed unit cell. (b) Phase difference between two states. 51

4.6 (a) Array structure. (b) Required phase distribution for $(\theta_0, \phi_0) = (0°, 0°)$. (c) Required phase distribution for $(\theta_0, \phi_0) = (30°, 0°)$). 52

4.7 (a) Radiation pattern at $\theta_0 = 0^0$, x-polarization. (b) Radiation pattern at $\theta_0 = 0^0$, y-polarization. (c) 3-D radiation pattern at $\theta_0 = 0^0$. (d) Radiation pattern at $\theta_0 = 30^0$, x-polarization. (e) Radiation pattern at $\theta_0 = 30^0$, y-polarization. (f) 3-D radiation pattern at $\theta_0 = 30^0$. 53

4.8 The proposed modified structure. 54

4.9 S-parameters of the proposed unit cell at (a) normal incidence and (b) oblique incidence. Phase difference between two states at (c) normal incidence and (d) oblique incidence. 57

4.10 (a) 3-D view of the modified array. Required phase for (b) $\theta_0 = 0^0$. (c) $\theta_0 = 30^0$. (d) $\theta_0 = 50^0$ 59

4.11 (a) Top and bottom layers of the fabricated array. (b) Fabricated prototype. (c) The DC circuit board of the array. 60

4.12 Antenna under test (AUT) in the anechoic chamber. (a) Front view. (b) Back view. 61

4.13 Simulated and measured radiation pattern for three arrays. (a) $\theta_0 = 0°$, x-polarization. (b) $\theta_0 = 0°$, Y-polarization. (c) $\theta_0 = 30°$, x-polarization. (d) $\theta_0 = 30°$, y-polarization. (e) $\theta_0 = 50°$, x-polarization. (f) $\theta_0 = 50°$, y-polarization. 62

4.14 (a) Measured gains for x-polarization. (b) Measured gains for y-polarization. (c) Gain vs.frequency for x-polarization. (d) Gain vs.frequency for y-polarization 64

4.15 Simulated radiation pattern under RHCP incident wave. (a) $\theta_0 = 0°$. (b) $\theta_0 = 30°$ 66

4.16 The proposed unit cell in an array under plane wave excitation. 68

4.17 The far-field pattern of the array with two different phase distributions. . . 69

4.18 (a) 3D view of the ME-dipole structure. (b) Electric and magnetic currents resulting from the excited electric field on the aperture. 71

4.19 Dual polarized ME-dipole antenna. 72

4.20 The proposed TR unit cell. (a) 3-D view. (b) Layer description. 73

4.21 Active PIN diodes for both polarizations in (a) State 1 with positive DC bias, and (b) State 2 with negative DC bias. 74

4.22 Simulation results of the proposed unit cell under y-polarized incident wave. (a) Transmission magnitude. (b) Transmission phase. 75

4.23 (a) The array structure in CST. (b) Required phase for $\theta_0 = 0°$. (c) Required phase for $\theta_0 = 30°$. 77

4.24 Simulated gain of the array. (a) $\theta = 0°$, x-polarization. (b) $\theta = 0°$, y-polarization. (c) $\theta = 30°$, x-polarization. (d) $\theta = 30°$, y-polarization. 78

5.1 Typical topologies using MEMS actuators. (a) MEMS actuators utilized as unit cells. (b) Fixed unit cells integrated with MEMS actuators. 82

5.2 Schematic of an ELC resonator with lumped element model. 84

5.3 The proposed unit cell structure using MEMS actuator. 85

5.4 Simulated reflection magnitude and phase of the proposed structure. (a) Reflection magnitude. (b) Reflection phase. 86

5.5 . Electric field strength at Hact=0.1mm. (a) 12.6 GHz. (b) 13 GHz. 87

5.6 (a) Waveguide simulation set up. (b) Reflection magnitude. (c) Reflection phase. 88

5.7 (a) Top layer of the ELC resonator. (b) Bottom layer of the ELC resonator. (c) Fabricated MEMS actuator. (d) SEM picture of the MEMS actuator. . 90

5.8 (a) Fabricated MEMS actuator on the alumina substrate. (b) Waveguide measurement set up. 91

5.9 Measured (a) reflection magnitude and (b) reflection phase of the proposed structure. 92

5.10 (a) Array structure usign the proposed unit cell. Discrete movement of actuators for (b) 1-bit phase distribution and (c) 2- bit phase distribution. 94

5.11 (a) 1-bit phase distribution. (b) 2-bit phase distribution. (c) analog phase distribution. (d) Simulated radiation patterns for $\theta_0 = 0^0$. 96

5.12 (a) 1-bit phase distribution. (b) 2-bit phase distribution. (c) analog phase distribution. (d) Simulated radiation patterns for $\theta_0 = 30^0$. 97

List of Tables

4.1 Dimensions of the proposed unit cell. 49

4.2 Dimensions of the modified proposed unit cell. 55

4.3 Comparison between the proposed RRA and related works 67

4.4 Dimensions of the proposed unit cell. 73

5.1 Dimensions of the proposed unit cell. 85

5.2 Performance comparison with related works 93

Chapter 1

Introduction

1.1 Motivation

Mobile networks have progressed substantially from the first generation (1G) to the fourth generation (4G), with each generation introducing key innovations to meet growing demands for higher data rates, improved reliability, and wider connectivity [1]. 1G, introduced in the early 1980s, supported basic analog voice communication but was limited in quality, capacity, and security. The 1990s saw the arrival of 2G, which transitioned to digital communication, offering enhanced voice quality, encrypted transmissions, and services like SMS and MMS. 3G introduced packet-switched data, enabling mobile internet, video calling, and multimedia messaging, with data rates reaching several Mbps—laying the groundwork for broadband mobility. The emergence of 4G marked a major leap with its all-IP architecture, delivering significantly higher data rates (up to 100 Mbps on mobile and 1 Gbps for stationary users), lower latency, and support for HD video streaming, VoIP, and other high-bandwidth applications, thereby enabling seamless and high-performance

mobile experiences [2].

With the exponential rise of connected devices, real-time applications, and the need for ubiquitous connectivity, 5G was developed to address the limitations of previous generations. It offers three key performance categories: enhanced mobile broadband (eMBB), ultra-reliable low-latency communication (URLLC), and massive machine-type communications (mMTC) [3]. 5G supports peak data rates up to 10 Gbps, end-to-end latencies under 1 ms, and the ability to connect over a million devices per square kilometer. Features such as network slicing, beamforming, and edge computing integration further enable applications in autonomous vehicles, industrial automation, remote healthcare, and smart cities, representing a paradigm shift toward highly flexible, intelligent, and service-oriented mobile networks [4].

The next generation of wireless networks, 6G, is envisioned as an innovative leap toward intelligent, ubiquitous connectivity driven by artificial intelligence (AI). Unlike previous generations, 6G will adopt an AI-native architecture, embedding machine learning and distributed intelligence throughout all network layers to enable real-time adaptation, dynamic optimization, and autonomous management [5]. This built-in intelligence will be essential to support emerging applications such as holographic communication, real-time digital twins, and ultra-reliable low-latency services. Use cases like augmented reality, telepresence, remote healthcare, and autonomous systems will impose extreme requirements in terms of latency (sub-millisecond), reliability (up to 99.99999%), and data rates (exceeding 1 Tbps) [6]. Meeting these demands requires integrating disruptive technologies such as terahertz and visible light communication, full-duplex radios, and 3D network topologies.

To ensure seamless connectivity, 6G will shift from cell-based structures to user-centric, cell-less designs that allow fluid transitions across heterogeneous networks. By merging

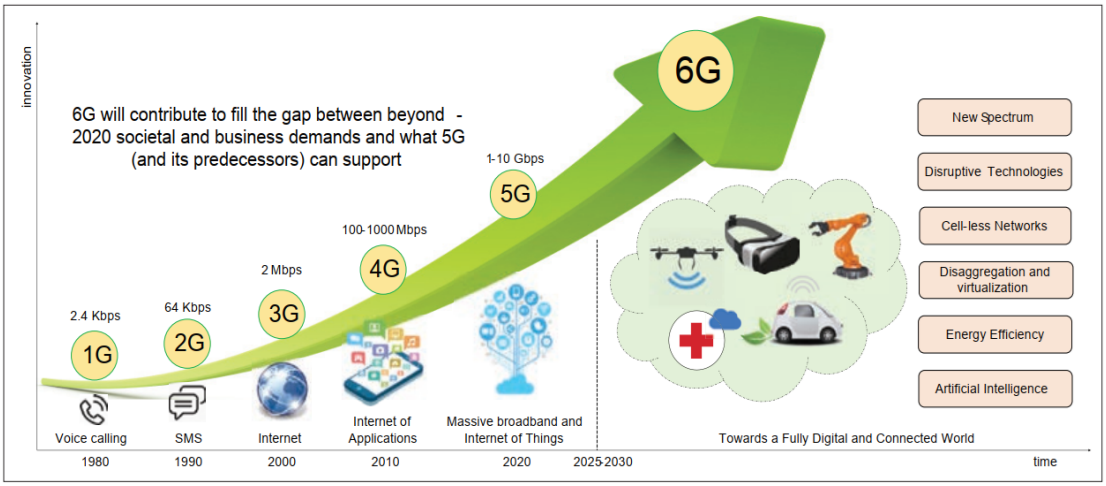


Figure 1.1: The evolution of cellular networks toward 6G [6].

communication, sensing, and edge intelligence into a unified framework, 6G aims to function as a proactive, context-aware platform—effectively serving as the digital nervous system of a hyper-connected and intelligent society [7].

Among the promising technologies being considered for 6G networks [8], reconfigurable intelligent surfaces (RISs) represent a paradigm shift in wireless communication by enabling the control and customization of the radio environment itself [9]. Unlike conventional relays or massive MIMO, RIS structures consist of large arrays of low-cost, nearly passive reflective (or transmissive) elements—typically implemented as metasurfaces—that can independently adjust the phase, amplitude, and polarization of incident electromagnetic waves, thereby dynamically shaping the wireless propagation channel. RISs can be mounted on building facades, indoor walls, or ceilings to create a programmable and adaptive wireless environment [10]. Critically, because they do not require active radio-frequency (RF) chains or sophisticated feeding networks, they offer ultra-low power consumption, minimal hardware complexity, and ease of deployment—making them ideal for

energy-constrained scenarios such as IoT, edge devices, and green 6G networks [11], as demonstrated in Figure 1.2.

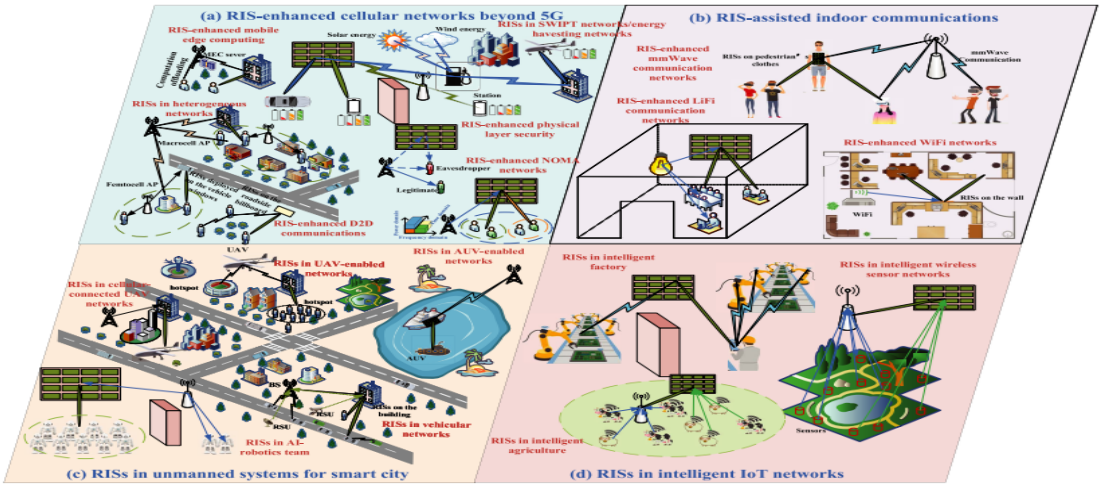


Figure 1.2: RIS application in the next generation of wireless system. [11].

RIS is particularly promising in addressing key 6G performance targets such as high spectral efficiency, ultra-reliable low-latency communication (URLLC), and energy efficiency. In dense urban or high-frequency (e.g., mmWave or THz) networks where signal blockage is a significant challenge, RISs can intelligently reflect and redirect signals to extend coverage and maintain line-of-sight conditions [12]. Advanced control algorithms, potentially aided by AI, can be used to optimize the RIS reflection parameters in real time for beamforming, interference suppression, or even secure communication through spatial signal manipulation. However, deploying RIS at scale presents challenges, including accurate channel estimation, efficient control signaling, hardware impairments, and scalability in dynamic environments. Despite these challenges, RIS is increasingly viewed not just as a communication enhancer but as a critical enabler of smart radio environments, where the propagation medium becomes an active participant in end-to-end system optimiza-

tion—marking a fundamental departure from traditional wireless design philosophy [13].

1.2 Objectives

This research targets reconfigurable intelligent surfaces (RISs) for next-generation wireless systems—especially non-line-of-sight (NLOS) scenarios that require agile beam steering and focusing. The overall goal is to propose, implement, and validate RIS building blocks and arrays that address key features such as beam scanning, wide bandwidth, and polarization diversity. Beam scanning is the fundamental characteristic of any RIS, enabling dynamic redirection of energy toward desired users or regions. In addition, wide operational bandwidth is essential for supporting high data rates, accommodating broadband waveforms, and maintaining stable performance over a wide frequency range, while dual-polarization capability (polarization diversity) increases achievable data throughput by exploiting multiple polarization channels and ensures that the RIS can effectively handle arbitrarily polarized incoming waves. These capabilities are therefore of particular interest in practical RIS design for future wireless communication systems. The specific objectives are:

- **Propose novel unit cell structures that address core RIS challenges.** Reflective and transmissive unit cells will be developed with electromagnetic responses tailored to enable reconfigurability, with emphasis placed on wideband operation, dual-polarization control, low insertion loss, compact footprint, and precise phase resolution.
- **Realize reconfiguration using semiconductor switches and MEMS actuators.** Reconfiguration will be implemented by integrating semiconductor switches (e.g., PIN

diodes) and MEMS actuators into the unit cells, with bias networks co-designed to provide reliable and simple control.

- **Design and synthesize arrays using the proposed unit cells.** Reconfigurable reflectarrays and transmitarrays (RRA/RTA) will be realized using the proposed unit cells for beam steering, anomalous reflection, and coverage enhancement, and array-level issues—including mutual coupling, efficiency, and manufacturing tolerances—will be addressed.

- **Validate through simulation, prototyping, and measurement.** Validation will be carried out through full-wave simulations, prototype fabrication, and anechoic-chamber measurements of patterns, gain, efficiency, bandwidth, polarization purity, and scanning performance.

1.3 Thesis Outline

In Chapter 1, the motivation, problem definition, objectives, and overall structure of the thesis were presented. The literature review is explored in Chapter 2, focusing on reconfigurable antennas and reconfigurable intelligent surfaces (RISs), with recent approaches classified and open challenges highlighted. In Chapter 3, a general RIS design methodology for beam steering and anomalous reflection applications is developed, and practical design rules and trade-offs are formalized. In Chapter 4, unit cell structures using semiconductor switches for reconfigurable reflectarrays and transmitarrays are proposed. The proposed structures address main challenges in reconfigurable array design which are bandwidth and ability to handle different polarization. A fabricated reflectarray using the proposed cell is demonstrated with measured validation to verify its functionality. Chapter 5 investigates

using MEMS actuator in unit cell design to achieve reconfigurability, verified by fabrication and measurements. Furthermore, reconfigurability and performance of the proposed unit cell was tested in an array-level simulation. In Chapter 6, key findings and limitations are summarized, and future directions such as unit cell design with higher phase states (2-bit) are outlined.

Chapter 2

Literature Review

2.1 Introduction

The next generation of wireless networks (6G) must meet ambitious targets for capacity, latency, reliability, and, critically, energy efficiency. Traditional solutions, such as ultra-dense base station deployment or massive MIMO, improve spectral efficiency but result in higher infrastructure costs and energy consumption. These designs treat the wireless propagation medium as an uncontrollable and often hostile part of the system, subject to multi-path fading, path loss, and interference. However, as pointed out in [14], this approach becomes increasingly inefficient and unsustainable in high-frequency bands (e.g., mmWave or THz), where propagation is easily blocked and unpredictable.

This realization has driven research into reconfigurable intelligent surfaces (RISs), a technology that enables programmable control over the wireless environment itself. An RIS comprises a large number of low-cost, nearly passive reflecting elements (e.g., metasurfaces) that can manipulate incident electromagnetic waves by adjusting their amplitude, phase, or

polarization. This capability allows RISs to dynamically reshape the propagation channel in favor of the communication objectives, offering a fundamental shift from traditional channel modeling to channel reconfiguration [11], [14].

The simplicity and ultra-low power consumption of RISs hardware make them particularly suitable for green wireless systems. Unlike amplify-and-forward (AF) relays, RIS units do not require RF chains or signal regeneration, significantly reducing energy costs while offering comparable gains in performance under optimal configurations [3]. As such, RIS-based architectures have been shown to achieve better energy efficiency than traditional relay-assisted architectures in both theoretical and simulation-based studies [9].

RIS also paves the way toward Smart Radio Environments (SREs), in which the propagation medium is transformed into a controllable and intelligent system component, as depicted in Figure 2.1. Instead of compensating for the randomness of the environment, RISs enable systems to exploit and even engineer it. This conceptual shift is supported by promising theoretical results and is envisioned to play a central role in meeting 6G's performance goals [14].

2.2 Reconfigurable Intelligent Surfaces

2.2.1 Engineered surfaces and the generalized law of reflection and refraction

In classical electromagnetic, wave interactions with material boundaries are governed by Snell's law, which dictates the angles of reflection and refraction solely based on the incident wave's angle and the refractive indices of the media. This framework assumes that the

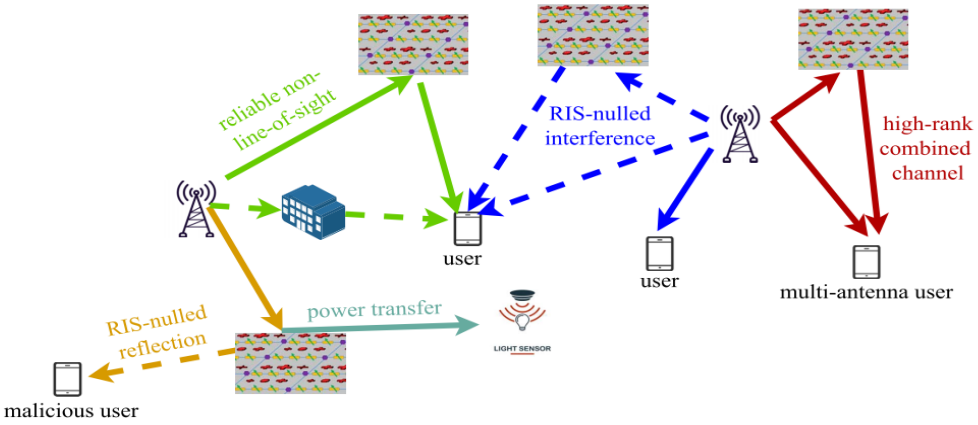


Figure 2.1: Application of RIS in a smart radio environment. [14].

surface boundary is smooth and passive, resulting in specular reflection and conventional refraction paths. However, such an assumption places inherent limits on wave control, particularly in complex wireless environments where obstacles, interference, and signal degradation are prevalent.

To transcend these constraints, researchers have explored engineered surfaces capable of reshaping the wavefront of incident electromagnetic (EM) waves. A key breakthrough in this area was the introduction of phase discontinuities at the surface level, which led to the development of the generalized laws of reflection and refraction. As demonstrated in [15], when a discontinuity induces abrupt phase changes along a surface, the direction of reflected and refracted waves deviates from classical predictions. The modified laws are expressed as:

$$\sin(\theta_t)n_t - \sin(\theta_i)n_i = \frac{\lambda_0}{2\pi}\frac{d\Phi}{dx}$$

$$\sin(\theta_r) - \sin(\theta_i) = \frac{\lambda_0}{2\pi n_i} \frac{d\Phi}{dx}$$

where $\frac{d\phi}{dx}$ denotes the spatial phase gradient imposed by the surface, and n_i and n_t are the refractive indices of the two media. This formulation allows for anomalous reflection and refraction, where waves can be directed in arbitrary directions regardless of the incident angle—paving the way for highly adaptable electromagnetic responses. A more general derivation was reported in [16] for a two-dimensional phase variation over a reflectarray surface.

To realize these engineered phase gradients, periodic surface structures are commonly employed. These are constructed from repeated electromagnetic inclusions—often metallic or dielectric scatterers—arranged on a planar substrate. The behavior of such structures depends heavily on the spatial period d relative to the wavelength λ_0, and the electromagnetic nature (resonant or non-resonant) of the unit cells. According to [17], periodic structures can be grouped into four broad categories, as illustrated in Figure 2.2. These categories are:

- **Electrically dense non-resonant sheets:** These have $d \ll \lambda_0$, are highly homogenizable, and behave like continuous impedance sheets. Examples include metallic films and dense wire grids used as reflectors or absorbers.
- **Frequency selective surfaces (FSS):** With intermediate periodicity ($\lambda_0/2 \leq d < \lambda_0$), FSSs exhibit resonance due to inductive and capacitive interactions in their geometry. They are used in filtering, reflectarrays, and antenna applications.
- **Sub-wavelength resonant arrays:** These structures feature very small elements ($d \approx \lambda_0/10$), such as mushroom-type high-impedance surfaces. They resonate due to strong capacitive coupling and offer localized phase manipulation.

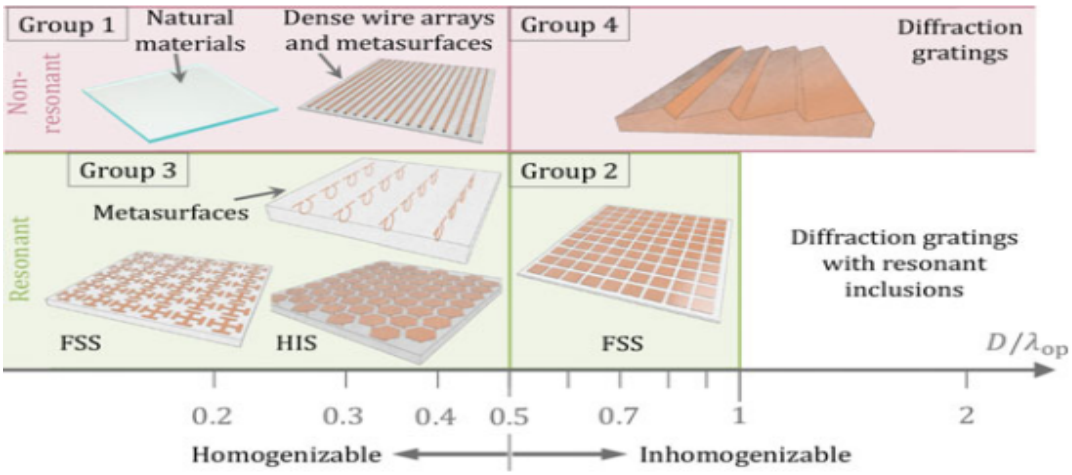


Figure 2.2: Classification of periodic planar structures [17].

- **Diffraction gratings:** Designed for $d \geq \lambda_0$, these structures intentionally exploit diffraction and are widely used in optics and beam-steering devices.

Metasurfaces are an advanced form of engineered periodic structures that typically fall within the first and third categories. Defined as electrically thin surfaces composed of sub-wavelength scatterers ($\lambda_0/30 < d < \lambda_0/2$), they enable fine-grained control over amplitude, phase, and polarization. Unlike traditional FSSs or diffraction gratings, metasurfaces can introduce complex, spatially varying responses across the surface to manipulate the wavefront with high precision.

2.2.2 Metasurfaces: Definition and Applications

Metasurfaces are the two-dimensional analogues of metamaterials, artificially structured planar materials composed of sub-wavelength scatterers that are engineered to manipulate electromagnetic (EM) waves in unprecedented ways. Unlike conventional materials, meta-

surfaces offer the ability to control the amplitude, phase, and polarization of EM waves at sub-wavelength resolution and within a thin layer—typically much thinner than the wavelength of operation [18].

Due to their compact form factor and high degree of tunability, metasurfaces have emerged as powerful tools in a wide range of applications. These include flat lenses, beam-steering devices, absorbers, polarizers, holographic plates, and wavefront shaping devices [19]. Recent advances have also enabled metasurfaces for dynamic applications such as tunable and nonlinear optics, THz modulation, and surface-wave control, making them essential components in modern optical and RF systems [20].

It should be noted that the definition of metasurfaces has been extended to include nonuniform surfaces. In these structures, the distances between adjacent inclusions and their sizes remain sub-wavelength, while the overall periodicity exceeds the half-wavelength. As a result, such surfaces may not be homogenizable, and their response must be analyzed using Bloch–Floquet theory through spatial harmonic expansion. These configurations are often referred to as metasurface-based gratings, drawing an analogy to conventional diffraction gratings [17].

2.2.3 From Metasurfaces to Reconfigurable Intelligent Surfaces

Traditional metasurfaces and reflective surfaces are composed of unit cells, which are periodic structures engineered to manipulate electromagnetic (EM) waves in specific ways. However, these structures are typically static and optimized for a single, fixed function determined at the time of fabrication. This limitation restricts their adaptability in dynamic environments or in multifunctional applications.

To overcome this limitation, researchers began incorporating tunable components, such

as varactor diodes, into metasurface architectures, enabling dynamic reconfiguration of the local electromagnetic response. By applying external control signals, the phase, amplitude, or polarization of each unit cell can be modified, allowing the surface to perform multiple functions without requiring physical redesign [21], [22]. The introduction of digital programmable surfaces in [23] and [24] marked a significant advancement in this area, offering a simpler and more scalable approach for realizing reconfigurable functionalities.

These evolutions led to the emergence of *reconfigurable intelligent surfaces* (RISs), which generalize the concept of metasurfaces by combining EM wave manipulation with embedded electronic control and software-defined functionality. RISs are envisioned as intelligent, programmable entities that can adapt to their environment and cooperate with wireless transceivers to improve signal coverage, directivity, and spectral efficiency [25].

2.2.4 Functionalities of RIS: Beyond Passive Reflection

RIS architectures can be broadly categorized into two types [26]:

- **Guided-wave structures:** These incorporate an integrated feed or source that excites the meta-atoms within the surface. By designing each element to achieve a desired surface impedance or phase shift, the RIS can radiate energy into space with specific beam patterns. Examples include leaky-wave antennas and holographic antennas.
- **Reflective/refractive structures:** In this configuration, the RIS is illuminated by an external wave, either a plane wave or a spherical wave, depending on the distance between the source and the surface. Each element on the RIS imposes a programmable reflection or transmission phase shift, enabling dynamic beam steering, beam shaping, or focusing without any embedded RF chains.

Reflective/refractive RIS structures can be used for different functions. Figure 2.3 outlines some functionalities of these structures in wireless communication systems [14]:

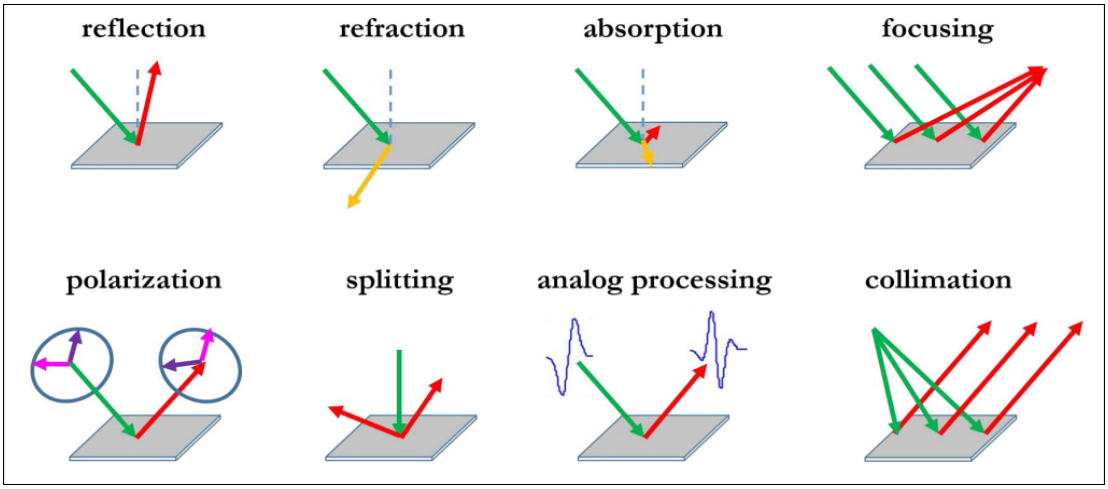


Figure 2.3: Different functionalities of reflective/refractive structures [14].

- **Reflection:** RIS can redirect incident waves toward arbitrary directions by imposing a desired phase-shift profile, enabling both specular and anomalous reflection behaviors.

- **Refraction:** Similar to reflection, RIS can tailor transmitted wave directions by engineering a spatial phase gradient, effectively generalizing Snell's law for transmission. Transmitarrays are practical implementations of this functionality, offering transmission control along with beam steering.

- **Absorption:** Through impedance matching and surface-loss engineering, RIS can absorb incoming EM waves, minimizing reflected or transmitted energy, which is useful for stealth and energy-harvesting applications.

- **Focusing:** By applying a phase distribution across the surface, RIS can converge plane waves to a focal point. Reflectarray antennas serve as classical examples of this application in reflective configurations.

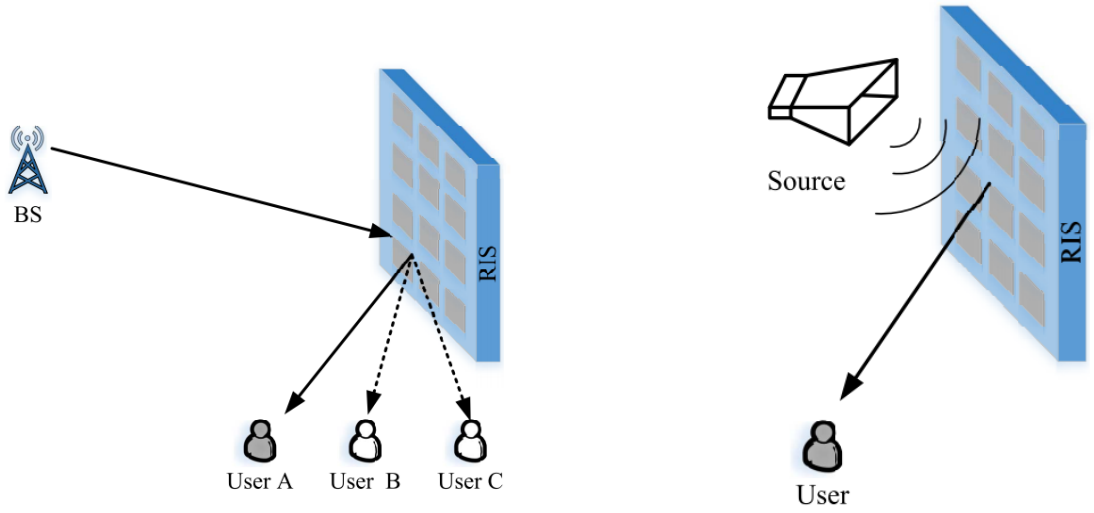
- **Polarization Control:** RIS structures composed of anisotropic meta-atoms can transform the polarization of EM waves, enabling dynamic polarization conversion and control.

- **Splitting:** RIS can split an incident wave into multiple beams with distinct directions, frequencies, or polarizations, enabling multi-user or multi-function operations.

- **Analog Processing:** RIS can perform analog computation directly in the EM domain, such as convolution or correlation, by engineering the spatial structure to emulate mathematical operations.

- **Collimation:** By appropriately adjusting the surface phase profile, RISs can transform diverging spherical waves into parallel plane waves, enhancing beam focusing. Reflectarrays also exemplify this functionality, especially when used to convert spherical wavefront into directive beams.

Among the above-mentioned applications, anomalous reflection (refraction) and beamforming (focusing and collimation) are of most interest in the new generation of wireless systems, as demonstrated in Figure 2.4. When the RIS is designed for anomalous reflection, an incident plane wave is redirected to the user in the far field, according to the generalized law of reflection. In the beamforming application, the incident wave is focused to a point, usually referred to as the focal point, following the theory of reflectarrays [27], [11]. In what follows, some of the reported work addressing these applications will be discussed.



(a) (b)

Figure 2.4: Two key functions of RIS. (a) Anomalous reflection (b) Beamforming [11].

2.3 Recent Advancements in RIS Design

2.3.1 Beamforming applications

Reconfigurable antenna arrays offer a promising solution for achieving versatility and adaptability in current and next-generation communication systems [28]. Beamforming is one of the key functionalities of reconfigurable intelligent surfaces (RISs) and mainly includes focusing and collimation. In focusing applications, an RIS transforms an incoming plane wave into a converging wavefront that concentrates energy at a specific point, similar to how a parabolic reflector focuses incoming plane waves onto its focal point. In collimation applications, an RIS converts a diverging spherical wave, typically radiated by a feed source, into a nearly planar wavefront, thereby producing a highly directive beam

and improving coverage in a desired direction.

With advancements in PCB technology, reflectarrays have emerged as a practical alternative, offering benefits such as low cost and ease of fabrication [29]. However, traditional reflectarrays are typically designed for fixed-beam applications. Recently, reconfigurable reflectarrays and transmitarrays have been developed, enabling dynamic and programmable radiation patterns and thereby enhancing the flexibility of wireless systems.

The fundamental component of any reflect/transmit array design is the unit cell. In conventional designs, each unit cell is assigned a specific reflection phase, enabling the array's radiation beam to be directed at a certain angle. To achieve reconfigurability, the reflection phase of each unit cell must be adjustable, which can be accomplished by integrating it with tunable materials or elements. Various methods have been considered, such as using liquid crystal [30], [31], varactor diodes [32], PIN diodes [33], [34], and MEMS switches and actuators [35], [36]. The choice of method largely depends on the target application, as each has its own advantages and drawbacks [37].

In [38], varactor diodes were integrated with patch-type unit cells to achieve reconfigurability by changing the resonance frequency (Figure 2.5). The fabricated reflectarray shows a maximum gain of 12.5 dBi with a 3-dB gain bandwidth of about 200 MHz at 5.5 GHz (3.6%) for all scanned angles. Designing the bias network is often the most challenging aspect of implementing reconfigurable structures, especially in large arrays. To mitigate this complexity, many systems employ discrete reflection phase states, achieved using RF switches such as PIN diodes and MEMS switches, instead of continuously tunable phase control. While this approach may lead to some degradation in radiation performance, including reduced array efficiency and increased sidelobe levels (SLL), it significantly simplifies the biasing network design [39], [40].

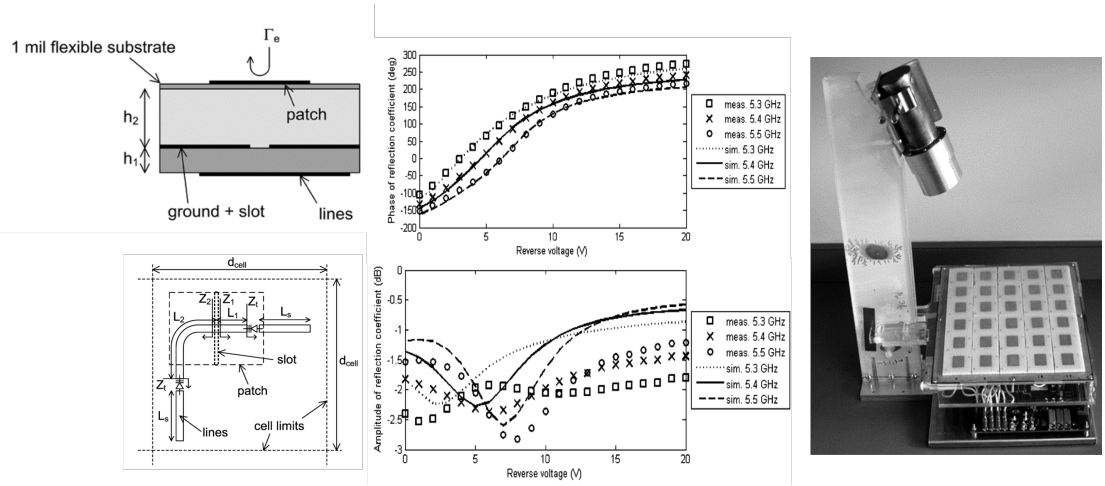
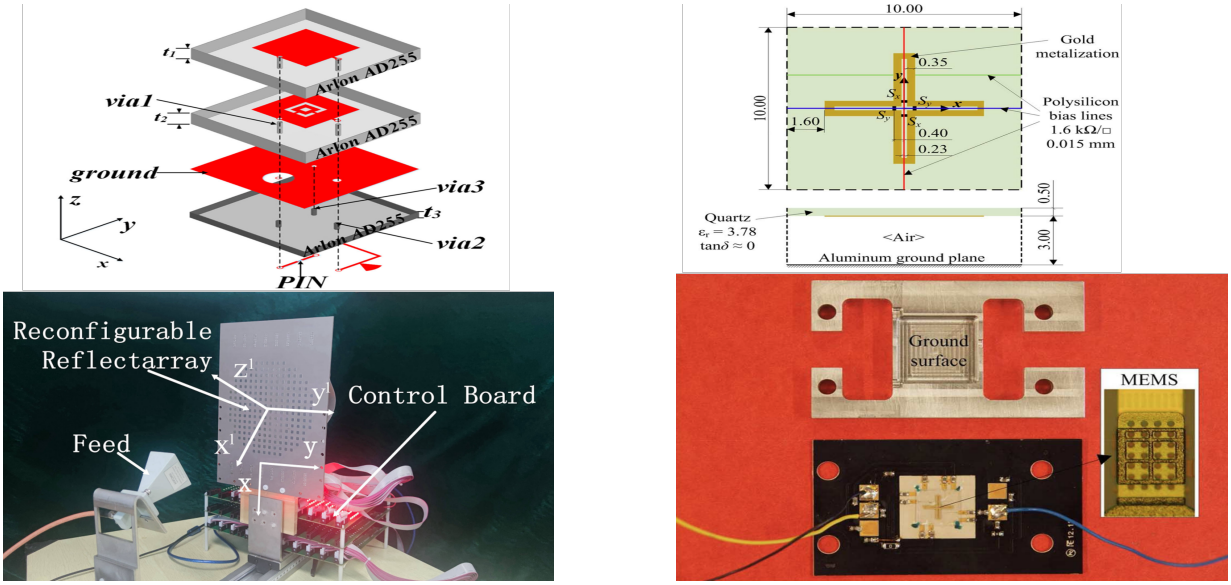


Figure 2.5: The proposed unit cell using a varactor diode in [38].

Several research studies have investigated reconfigurable reflectarrays (RRAs) employing discrete reflection phase states at the unit-cell level. In [41], a 12×12 RRA was fabricated using 1-bit unit cells (two phase states), each consisting of a slotted patch integrated with a PIN diode. The fabricated array demonstrated a maximum gain of 19.2 dBi at 5 GHz, with a 1-dB gain bandwidth of 8% and a radiation efficiency of 15.5%. It is also capable of beam scanning up to 60°. The authors in [42] proposed a wideband RRA by employing a multilayer stacked structure forming a double-resonance behavior. The 16×16 fabricated RRA shows a gain of 21.6 dBi, with a 22.5% 1-dB gain bandwidth and 25% aperture efficiency (Figure 2.6-(a)). MEMS switches have been used in some proposed structures [43], [44]. In [44], a four-leg unit-cell structure was loaded with ohmic MEMS switches, enabling reflection phase variation by switching them ON or OFF. The proposed design supports both x- and y-polarizations, which is a valuable feature for certain applications. However, the concept was not experimentally validated in a fabricated array (Figure 2.6-(b)).



(a) (b)

Figure 2.6: (a) Proposed structure in [42]. (b) Proposed unit cell using MEMS switches in [44].

To obtain better radiation efficiency, unit-cell designs with four phase states (2-bit) have been considered in various research works. In [45], the proposed unit cell consists of a defected split-ring slot patch loaded with two PIN diodes and a cross-shaped hollow ring loaded with four PIN diodes. By combining the states of these PIN diodes, different current paths are obtained to achieve 2-bit phase quantization. A passive prototype with a high aperture efficiency of 35.1% was fabricated. The authors in [46] proposed a dual-polarized unit cell for the sub-6 GHz frequency band, which includes an aperture-coupled patch, two perpendicular slots, and two microstrip delay lines. Each delay line has only two PIN diodes, and all four states of the two PIN diodes are fully utilized to achieve 2-bit phase resolution. The 16×16 fabricated RRA shows a maximum measured gain of 23.11, with 40.5% radiation efficiency (Figure 2.7).

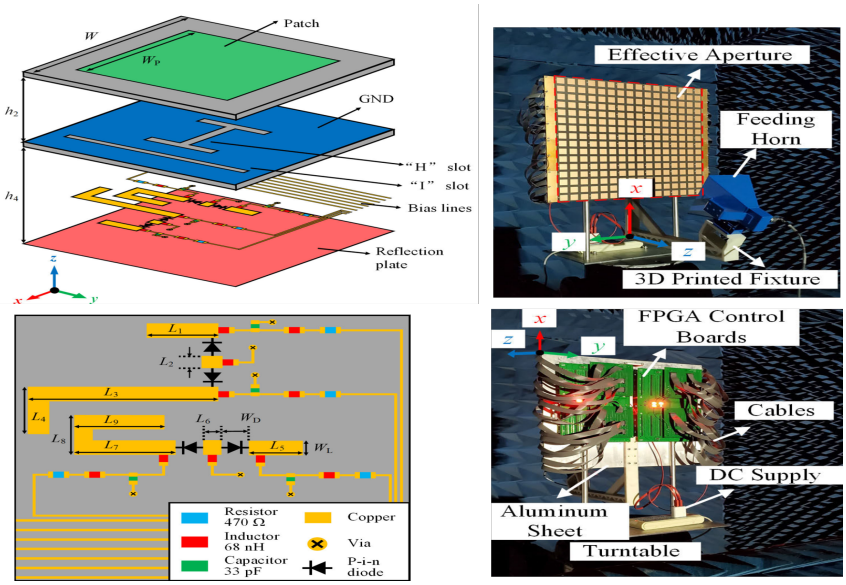


Figure 2.7: The proposed 2-bit unit cell in [46].

2.3.2 Anomalous reflection

As discussed previously, anomalous reflection refers to changing the reflection angle of an incident wave using the concept of the generalized Snell's law of reflection and refraction. In contrast to beam focusing, the incident wave is a plane wave from a source that is located in the far field of the array. In [47], a reflectarray was utilized to improve a non-line-of-sight (NLOS) radio channel by redirecting the received signal from the base station to a certain angle and mitigating building blockage. The work in [48] presents an RIS prototype for adaptive beamforming, evaluated through both indoor and outdoor field trials. The proposed unit cell consists of a metallic patch integrated with varactor diodes as the tuning elements, enabling continuous phase control by adjusting the bias voltage. This configuration allows beam steering toward desired directions, and experimental results show significant improvements in received signal strength across various environments (Figure

2.8-(a)). Similarly, [49] reports the design and implementation of a sub-6 GHz RIS for real-world demonstrations. Its unit cell employs a square patch loaded with varactor diodes and a dedicated biasing network to achieve continuous phase shifts. Measurements and simulations confirm effective beam-steering capability, with notable enhancements in coverage and signal quality in practical scenarios.

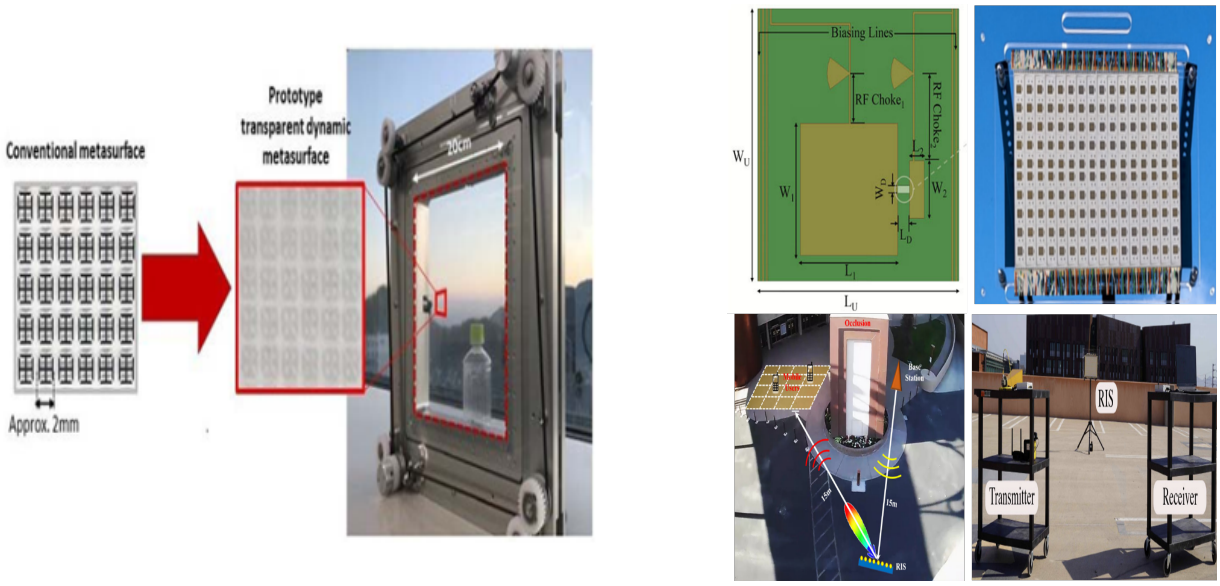
In [50], NTT DOCOMO and AGC developed a transparent dynamic metasurface at 28 GHz that can switch between full penetration, partial reflection, and full reflection of radio waves by shifting a movable glass layer. It maintains optical transparency, scales to large sizes, and is suitable for windows, vehicles, billboards, and secure indoor areas. Trials showed successful mode switching without attenuation, with future versions targeting high-speed actuator control and frequencies beyond 5G.



(a) (b)

Figure 2.8: (a) Proposed RIS in [48]. (b) Proposed RIS in [49].

Similar to what was presented in beamforming applications, discrete reflection phase has been employed in structures with anomalous reflection, especially through the introduction of digital metamaterials and coded metasurfaces in [23] and [24], respectively. Despite their discrete nature, coded metasurfaces have demonstrated strong capabilities in electromagnetic field manipulation. Coding can be applied not only to the reflection phase, but also to parameters such as amplitude, polarization, and orbital angular momentum (OAM), enabling a wide range of field-control functionalities [51].



(a) (b)

Figure 2.9: (a) Proposed RIS by NTT DOCOMO in [50]. (b) Proposed RIS in [52].

The authors in [52] designed and implemented an RIS using a patch-based unit cell with an integrated PIN diode in a 160-element array. Their field measurements demonstrate improved communication performance, with significant signal-to-noise ratio (SNR) gains when the RIS is deployed compared with the case without RIS. In [53], different func-

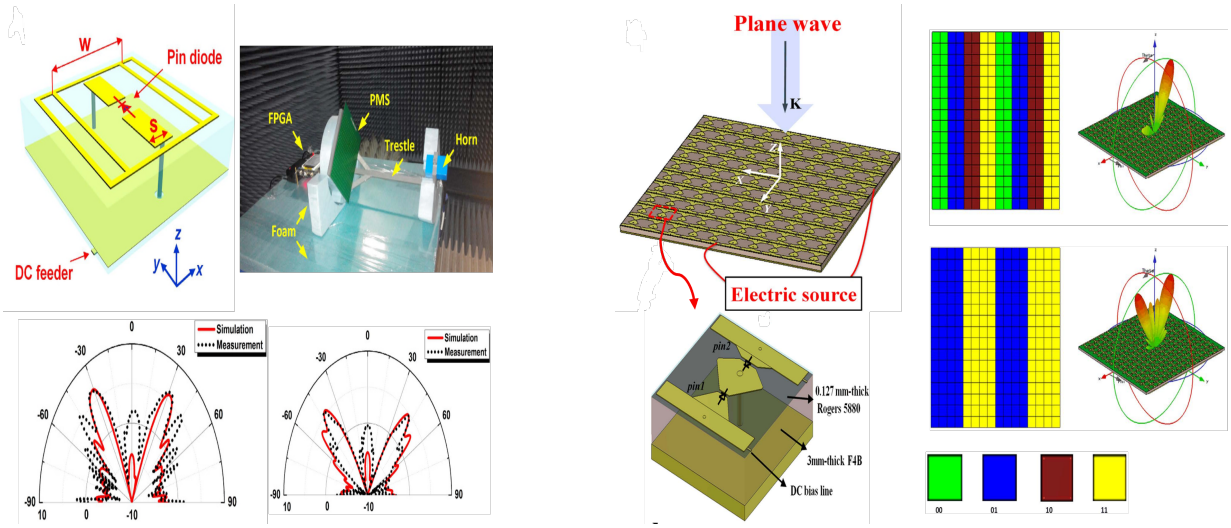
tionalities of a coded metasurface were demonstrated by integrating a PIN diode into a patch unit cell. A programmable metasurface containing 1600 individually controlled unit cells was fabricated to demonstrate the dynamic manipulation of electromagnetic waves. By applying a binary coding matrix, genetic algorithm, and inverse fast Fourier transform (IFFT) technique, various scattering and focusing functionalities were obtained.

The authors in [54] proposed a 1-bit unit cell operating at 9.2 GHz. By applying different phase distributions over the array surface, the reflected beam direction is changed. It was also shown that the direction of the reflected wave in 1-bit coded metasurfaces changes when different lattice sizes are used. A 2-bit structure was proposed in [55] using two pairs of metallic trapezoidal and rectangular patches integrated with two PIN diodes. Each PIN diode is independently controlled by a DC bias line, which results in four phase states for the two diodes. The fabricated array was illuminated by a plane wave source, and beam steering was verified for different phase patterns.

2.4 Summary

Reconfigurable intelligent surfaces (RISs) have emerged as a promising technology for controlling electromagnetic wave propagation in next-generation wireless networks. By integrating tunable elements such as varactor diodes or RF switches into periodic unit cells, RISs can dynamically adjust reflection phase, amplitude, and polarization to shape the wavefront as desired. Two primary applications are evident in the literature: beamforming and anomalous reflection.

In beamforming applications, RISs enable wavefront transformation from an incident plane wave to a focused or steered beam, enhancing coverage and signal quality. Examples include 1-bit PIN-diode-based reflectarrays and varactor-tuned prototypes that achieve



(a) (b)

Figure 2.10: (a) 1-bit array implemented in [54]. (b) 2-bit array proposed in [55].

wide scanning angles, dual-polarization operation, and demonstrated adaptability in real-world field trials. In anomalous reflection, RISs are designed to redirect incident waves toward non-specular directions, enabling precise control of reflection angles for coverage optimization and interference management. Coding metasurfaces, including 1-bit and 2-bit designs, have been widely employed to achieve such effects, with capabilities extended to manipulate amplitude, polarization, and orbital angular momentum.

These developments show that RIS technology, when applied to beamforming and anomalous reflection, enables new possibilities in adaptive wireless environments, improving indoor coverage and enhancing outdoor links through transparent integration on building surfaces and vehicles.

Chapter 3

Design Methodology of Reconfigurable Intelligent Surfaces (RISs)

3.1 Introduction

Engineered electromagnetic surfaces — encompassing metasurfaces, frequency-selective surfaces (FSS) and diffraction grating surfaces- are artificially structured interfaces designed to manipulate electromagnetic (EM) waves in ways not achievable with natural materials. By controlling the amplitude, phase, polarization, or direction of incident waves, they enable applications ranging from wireless communications and radar stealth to imaging and sensing. At the heart of these surfaces lies the unit cell, the sub-wavelength building block whose geometry and material composition dictate the local EM response. Furthermore, the periodicity between adjacent units determines the proper design method [17].

When arranged periodically or quasi-periodically, these unit cells form a surface with tailored dispersion and wave manipulation properties.

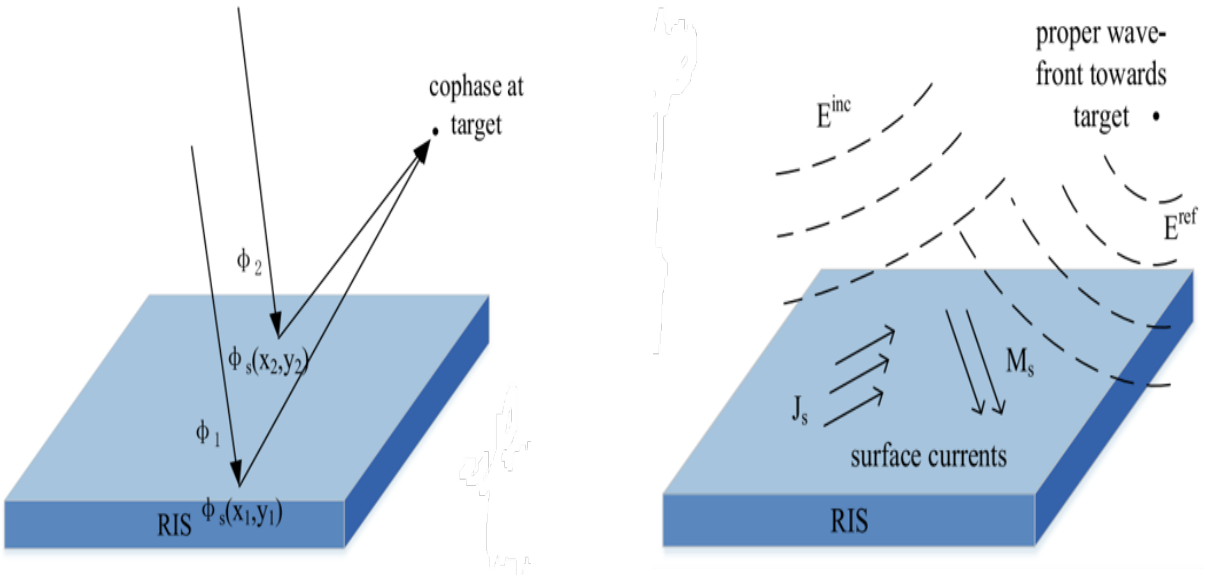
Generally, two main perspectives have been utilized for design of reflective surfaces, ray optics and wave optics, as shown in Figure 3.1. In the ray optics method, waves are assumed as rays in which their phases increase by path length. Therefore, a phase will be defined for each element on the array. The phase of reflected wave is related to the incident wave phase and unit cell reflection phase. In wave-optics, the interaction between incident wave and material is modeled by equivalent theorems like love's equivalence and surface equivalence theorems. Desired scattered wave is obtained by proper wave transformation by the surface [11]. Ray optics is a simplified model in RIS design compared to wave optics, but it has some disadvantages. In this method, interaction between elements is not considered which may lead to difference in fabrication results compared to simulation results. This is an important point which must be considered in RIS design. In what follows, the basic design procedure of RIS for beamforming and anomalous reflection applications will be discussed.

3.2 RIS Design for Beamforming Applications

3.2.1 Ray optic approach

In beamforming applications, one of the receiver or transmitter is positioned in the near field of the array. This will enforce the design process to bring the spatial phase delay into calculation. This design procedure is well-explained in reflectarray design.

Like typical array structure, to direct the radiation beam to a certain direction, a progressive phase is needed for array elements. The main procedure is the same for reflect-



(a) (b)

Figure 3.1: Two main perspective in reflective surface design. (a) Ray optics. (b) Wave optic. [11].

arrays, however spatial phase change due to distance from elements to the source should be considered [29]. Figure 3.2 shows a geometrical view of a reflectarray with the source position. The array elements are in the far-field of the source, and they are illuminated by a spherical wave with a certain angle. The emanated field from the source originates from the phase center and has a spatial phase delay. This phase delay should be compensated by array elements. Spatial phase delay is given by

$$\phi_{\text{spd}} = -k_0 R_i \tag{3.1}$$

where R_i is the distance between the i^{th} element and the phase center, and k_0 is the wave number at the center frequency. The required progressive phase distribution on the

reflectarray to produce a beam in (θ_0, ϕ_0) is represented as

$$\phi(x_i, y_i) = -k_0 \sin\theta_0 \left(x_i \cos\phi_0 + y_i \sin\phi_0\right) \tag{3.2}$$

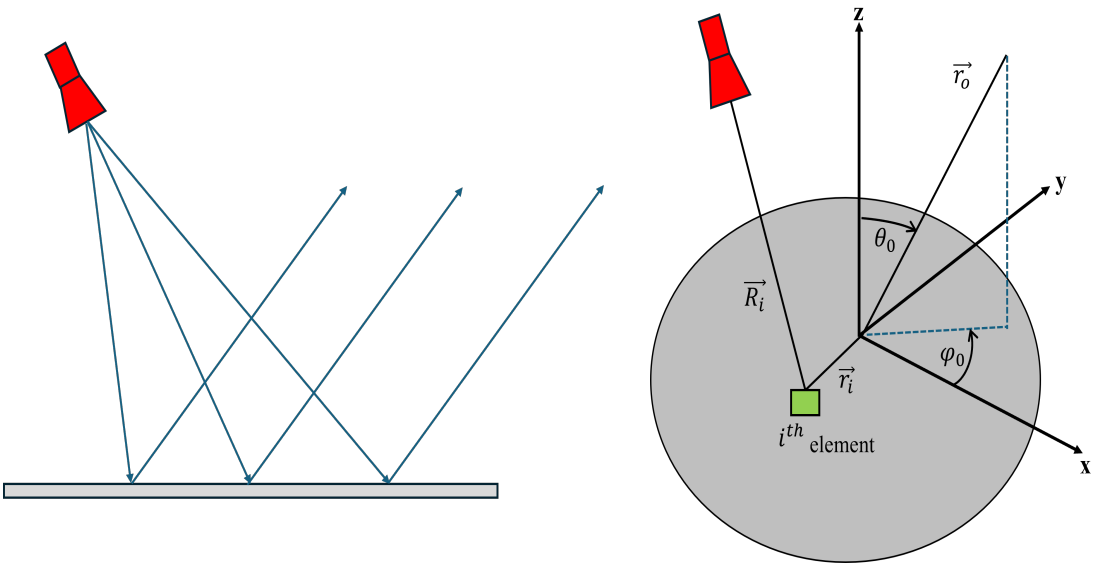


Figure 3.2: Geometry of reflectarray with source position .

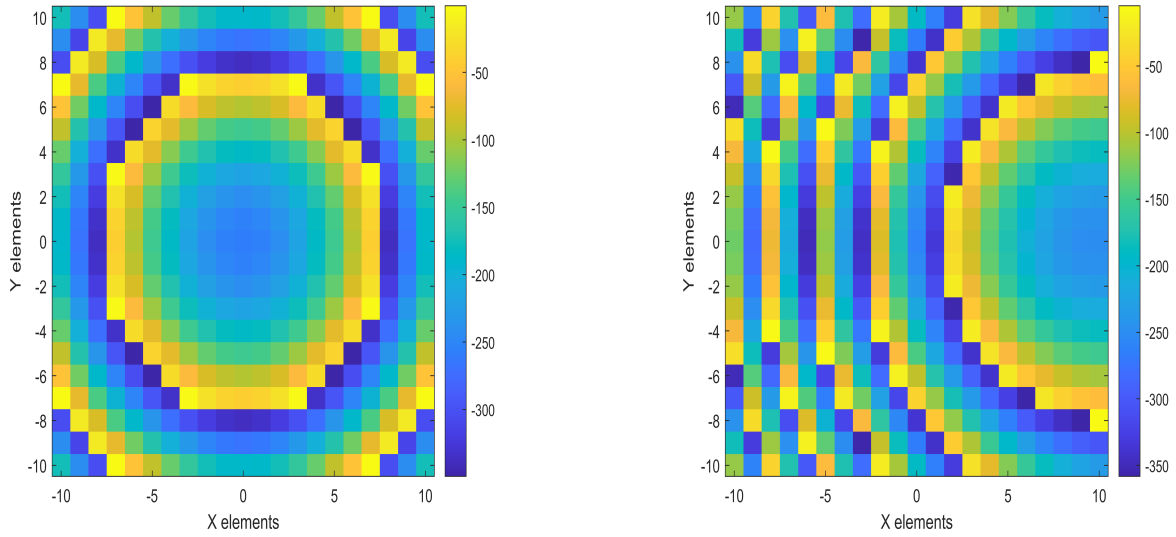
where (x_i, y_i) is the coordinate of the i^{th} element. On the other hand, the phase of the reflected wave on each element is the summation of spatial phase and the phase introduced by the element, which can be expressed as

$$\phi(x_i, y_i) = -k_0 R_i + \phi_R(x_i, y_i) \tag{3.3}$$

where $\phi_R(x_i, y_i)$ is the reflection phase introduced by the unit cell. From Equations (3.2) and (3.3), the required reflection phase of each element is calculated as

$$\phi_R(x_i, y_i) = k_0 \left[R_i - \sin\theta_0 \left(x_i \cos\phi_0 + y_i \sin\phi_0\right)\right] + \Delta\phi \tag{3.4}$$

where $\Delta\phi$ is a phase offset which is added to all the array elements. Figure 3.3 shows the required reflection phase of a 21×21 array at 13 GHz to collimate the beam to $(\theta_0 = 0°, \phi_0 = 0°)$ and $(\theta_0 = 30°, \phi_0 = 0°)$ directions respectively.



(a) (b)

Figure 3.3: Required phase distributions for two directions. (a) $(\theta_0, \phi_0) = (0°, 0°)$. (b) $(\theta_0, \phi_0) = (30°, 0°)$.

This analysis is only on a phase basis, and it does not discuss radiation characteristics of a reflect array. To address this issue, a full wave analysis should be done based on far-field analysis of electric field on the array aperture which is related to reflected wave from array elements. It will be discussed in the later section.

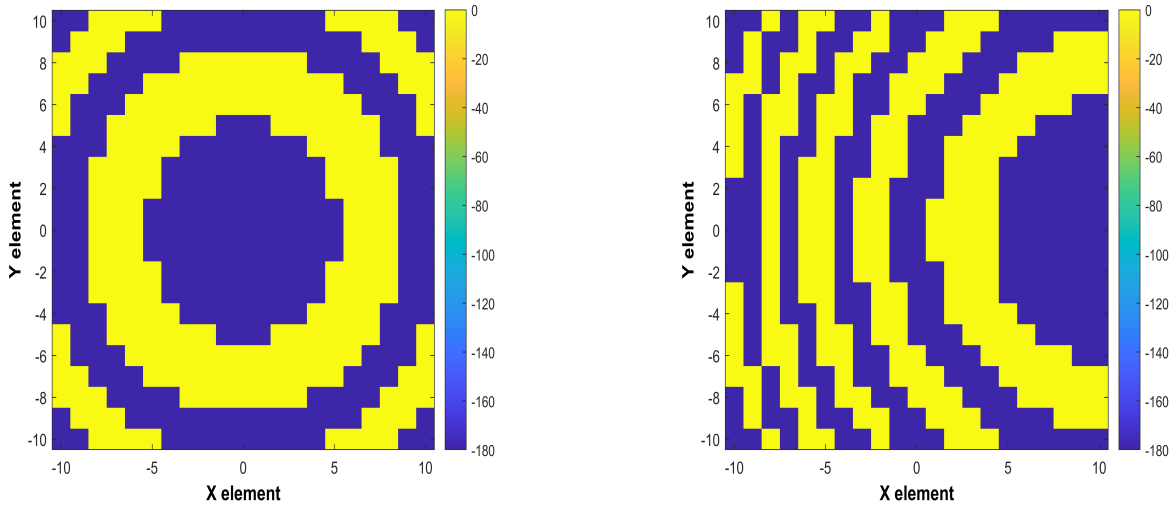
3.2.2 1-bit array design

As mentioned in the literature review, recent designs utilizes discrete reflection phase in reflectarray due to less complexity in bias and control system. In a 1-bit RRA design, the continuous reflection phase in Equation 3.4 should be quantized into two states, which can be implemented in various schemes. The 1-bit quantized phase can be expressed as

$$\varphi_{\text{1–bit}} = \begin{cases} 0^\circ, & \phi_{m,n} \in [0^\circ, -180^\circ] \\ -180^\circ, & \phi_{m,n} \in [-180^\circ, -360^\circ] \end{cases} \tag{3.5}$$

in which the two states are chosen as 0° (state 1) and -180° (state 2). The corresponding quantized reflection phases of the array shown in Figure 3.3 are demonstrated in Figure 3.4. As explored in [56], the use of different quantization schemes will result in different radiation performance, which can be used as a useful parameter in the RRA design.

According to Equation 3.4, $\Delta\phi$ does not change the required phase difference between elements and does not affect the radiation angle of the array. However, it changes the absolute required reflection phase of each element, which may impact the overall performance of the array, especially in arrays employing resonant-type unit cells. In array design using discrete phase states, altering this parameter will impact the ON/OFF states of the PIN diodes and consequently the required phase distribution. In general, the constant phase offset is advantageous for improving radiation efficiency [57]. Using these design keys is useful in mitigating the radiation performance degradation due to phase quantization.



(a) (b)

Figure 3.4: Required quantized phase distributions for two directions. (a) $(\theta_0, \phi_0) = (0°, 0°)$. (b) $(\theta_0, \phi_0) = (30°, 0°)$.

3.2.3 Wave optic approach

The wave optic approach is a useful method to evaluate radiation characteristics of the array including directivity, gain and the side lobe level (SSL).The incident field on the array is determined using the feed antenna pattern. By calculating the electric field on the array surface and applying a two-dimensional Fourier transformation over the array surface, the radiation parameters can be obtained. Figure 3.5 illustrates the geometry of a reflectarray illuminated by a horn antenna as the source.

The horn antenna is assumed to have a symmetric pattern in both the E-plane and H-plane. Therefore, its pattern can be modeled as a $\cos^q(\theta)$ function. For an ideal feed, the radiated electric field can be expressed as [29]:

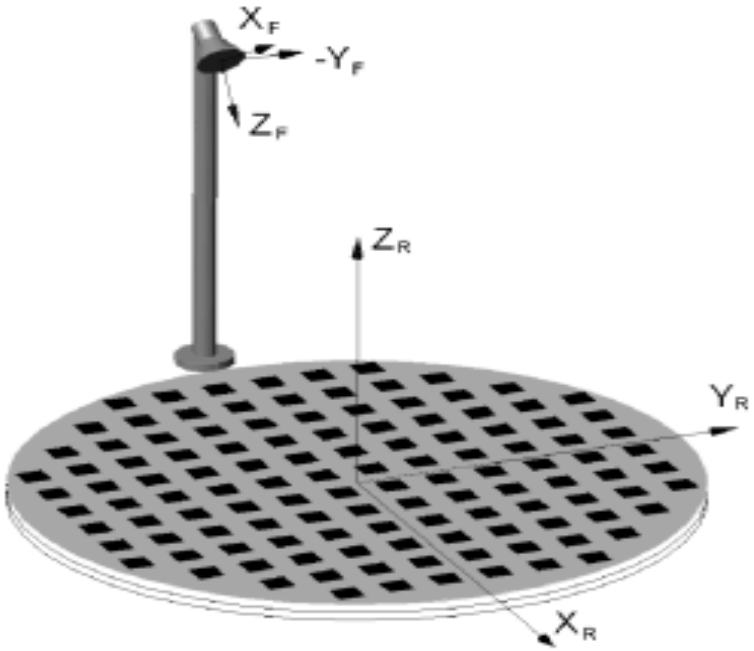


Figure 3.5: Geometry of reflectarray with a horn antenna source [29].

$$\text{x-polarized feed: } E^{F_x}(\theta,\phi) = \frac{jke^{-jkr}}{2\pi r}\left[\hat{\theta}C_E(\theta)\cos\phi - \hat{\phi}C_H(\theta)\sin\phi\right] \tag{3.6}$$

$$\text{y-polarized feed: } E^{F_y}(\theta,\phi) = \frac{jke^{-jkr}}{2\pi r}\left[\hat{\theta}C_E(\theta)\sin\phi + \hat{\phi}C_H(\theta)\cos\phi\right] \tag{3.7}$$

where F denotes fields in the feed coordinate system, and C_E and C_H correspond to the feed pattern in the E-plane and H-plane, respectively, and are defined as:

$$C_E(\theta) = \cos^{q_E}(\theta), \qquad C_H(\theta) = \cos^{q_H}(\theta) \tag{3.8}$$

For a symmetric feed pattern, $q_E = q_H = q$. In the next step, the radiated field at each reflectarray unit cell should be expressed in the reflectarray coordinate system

(X_R, Y_R, Z_R), as shown in Figure 3.5. Using Equation 3.7 and Equation 3.8, the electric field at the center of each element is calculated. It is converted to Cartesian components by:

$$\begin{bmatrix} E_x^R \\ E_y^R \\ E_z^R \end{bmatrix} = \begin{bmatrix} \sin\theta\cos\phi & \cos\theta\cos\phi & -\sin\phi \\ \sin\theta\sin\phi & \cos\theta\sin\phi & \cos\phi \\ \cos\theta & -\sin\theta & 0 \end{bmatrix} \begin{bmatrix} 0 \\ E_\theta^F \\ E_\phi^F \end{bmatrix} \tag{3.9}$$

After this transformation, the Cartesian field components are transformed from the feed coordinate system (F) into the reflectarray coordinate system (R). Let A be the transformation matrix performing this conversion. The electric field on each unit cell is then:

$$E^{R_C} = A\, E^{F_C} \tag{3.10}$$

Once the incident field on each unit cell is determined, the reflected wave can be expressed as:

$$\begin{bmatrix} E_x^{\text{ref}} \\ E_y^{\text{ref}} \end{bmatrix} = \begin{bmatrix} \Gamma_{xx} & \Gamma_{xy} \\ \Gamma_{yx} & \Gamma_{yy} \end{bmatrix} \begin{bmatrix} E_x^{\text{inc}} \\ E_y^{\text{inc}} \end{bmatrix} \tag{3.11}$$

Since the reflected wave from each unit cell is known, the radiation characteristics of the reflectarray can be determined using either the angular spectrum method or the current distribution approach on the surface, both of which are thoroughly discussed in the literature [29]. Although this formulation may appear complex, it provides accurate predictions of radiation characteristics and is especially useful for identifying sources of discrepancies between theoretical analysis and experimental measurements.

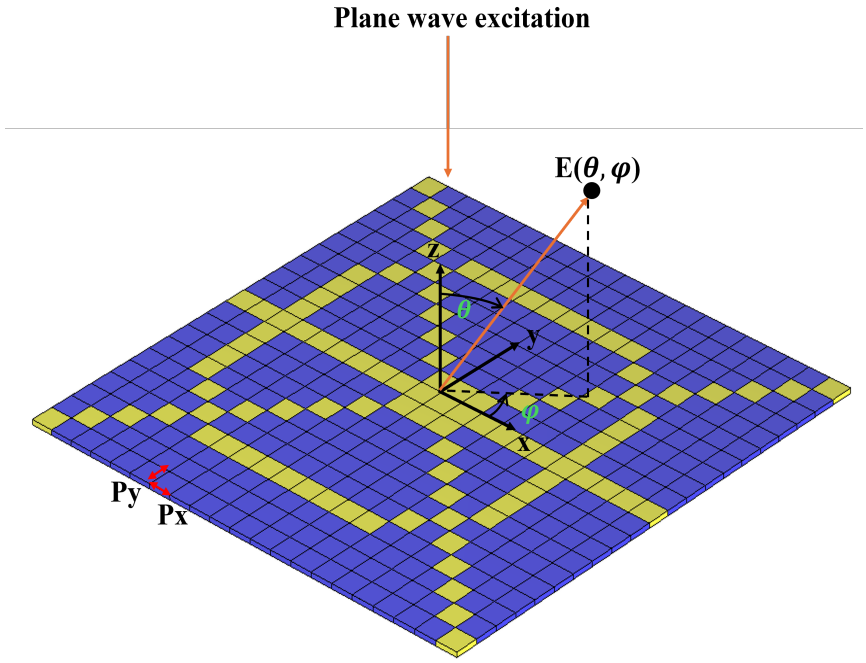


Figure 3.6: The 1-bit array structure illuminated with a plane wave source.

3.3 RIS Design for Anomalous Reflection Applications

In anomalous reflection, the array is excited with a plane wave source which is positioned far away from the array surface. In this case, the spatial phase delay is the same for all array elements while it was different in beamforming applications. Figure 3.6 represents a 1-bit array which is illuminated by a plane wave source.

The reflection amplitude is assumed to be unity due to the perfect reflection of the coding particle, and thus the electric field on the metasurface can be expressed in the cartesian coordinate system as [58]:

$$E_{m,n}(x', y') = e^{i\phi(m,n)} \tag{3.12}$$

where $\phi(m, n)$ represents the reflection phase of the coding particle (m, n), which is either 0 or π for a 1-bit unit cell with two phase states. The local coordinates x', y' are limited to the size of a coding particle:

$$-\frac{P_x}{2} < x' < \frac{P_x}{2}, \quad -\frac{P_y}{2} < y' < \frac{P_y}{2}. \tag{3.13}$$

Using the spectral analysis technique and asymptotic phase approximation, the far-field scattered electric fields for a 1-bit array can be calculated using following formulation: [59]

$$\mathbf{E}(r, \theta, \phi) = \frac{jke^{-jkr}}{2\pi r}\left[\hat{\theta}\left(F_x \cos\phi + F_y \sin\phi\right) + \hat{\phi}\,\cos\theta\left(-F_x \sin\phi + F_y \cos\phi\right)\right] \tag{3.14}$$

where F_x and F_y are the two dimensional Fourier transform of the electric field over the array surface for x-polarized and y-polarized incident waves respectively.

$$F_x = \int_{-\frac{MP_x}{2}}^{\frac{MP_x}{2}} \int_{-\frac{NP_y}{2}}^{\frac{NP_y}{2}} E_x(x, y)\, e^{jk(x\sin\theta\cos\phi + y\sin\theta\sin\phi)}\, dx\, dy \tag{3.15}$$

$$F_y = \int_{-\frac{MP_x}{2}}^{\frac{MP_x}{2}} \int_{-\frac{NP_y}{2}}^{\frac{NP_y}{2}} E_y(x, y)\, e^{jk(x\sin\theta\cos\phi + y\sin\theta\sin\phi)}\, dx\, dy \tag{3.16}$$

For a y-polarized incident wave, the far-field scattered electric field is expressed as

$$\mathbf{E}(r, \theta, \phi) = \frac{jke^{-jkr}}{2\pi r}\left[(\hat{\theta}\ \sin\phi + \hat{\phi}\,\cos\theta\,\cos\phi)Fy\right] \tag{3.17}$$

To evaluate the F_y, the integral in Equation 3.16 is transformed to to the unit cell intervals.

$$F_y = \int_{-\frac{P_x}{2}}^{\frac{P_x}{2}} \int_{-\frac{P_y}{2}}^{\frac{P_y}{2}} E_{m,n}(x', y')\, e^{jk(x \sin\theta \cos\phi + y \sin\theta \sin\phi)}\, dx'\, dy' \tag{3.18}$$

$$x' = x - \left(m - \frac{M-1}{2}\right) P_x \tag{3.19}$$

$$y' = y - \left(n - \frac{N-1}{2}\right) P_y \tag{3.20}$$

where x' and y' and local coordinates within the unit cell. By doing integration over Equation 3.16, they results will be

$$u = \sin\theta\, \cos\phi, \qquad v = \sin\theta\, \sin\phi, \qquad k_0 = \frac{2\pi}{\lambda}. \tag{3.21}$$

$$F_y(u, v) = K\, P_x P_y\, \operatorname{sinc}\left(\frac{k_0 u P_x}{2}\right)\, \operatorname{sinc}\left(\frac{k_0 v P_y}{2}\right)\, \sum_{m=0}^{M-1} \sum_{n=0}^{N-1} \exp\big(j\, \phi(m, n)\big)\, \exp\Big(j k_0\, [\, u\, m P_x + v\, n P_y\,]\Big). \tag{3.22}$$

$$K = \exp\left(-j\, \frac{k_0 u (M-1) P_x}{2}\right)\, \exp\left(-j\, \frac{k_0 v (N-1) P_y}{2}\right). \tag{3.23}$$

By evaluating Equation 3.22, the far-field scattered electric field is obtained using Equation 3.17. Different radiation patterns are produced by changing the phase distribution over the array surface. Figure 3.7 shows various applied phase distributions with their corresponding radiation patterns. It is observed that the direction of the main beam changes

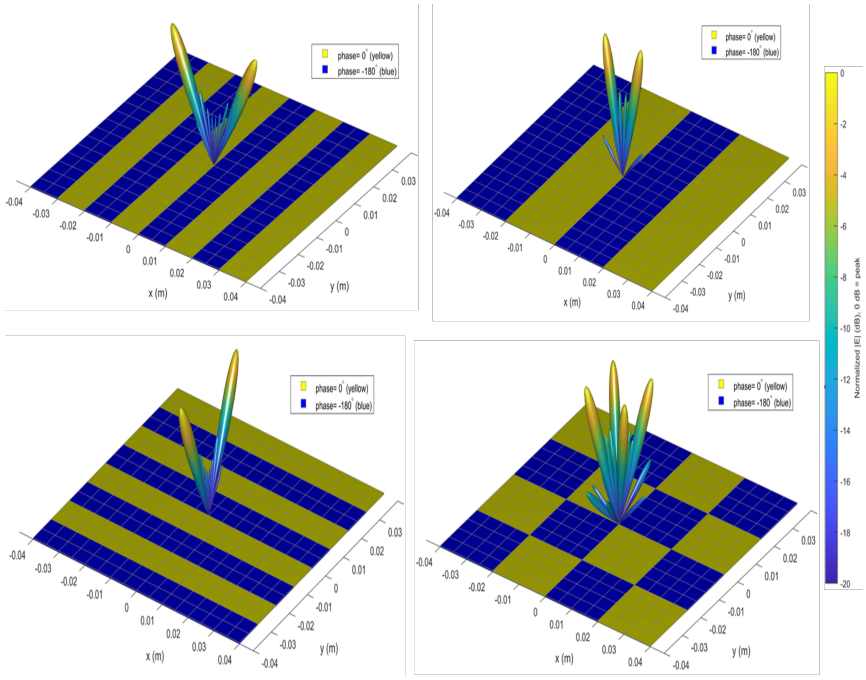


Figure 3.7: Different phase distributions over the array surface with corresponding radiation pattern.

when different sequences of rows with the same phase state are applied, as illustrated in Figure 3.7 (a)–(d). It is worth mentioning that a 1-bit reflective surface radiates two main beams when it is excited by a plane-wave source, as discussed in detail in [60]. It was shown by the authors that single-beam patterns can be achieved by introducing a fixed prephase distribution with two values over the 1-bit array. Another solution is to employ unit cells with higher phase resolution (2-bit, 3-bit, etc.) to address this issue. The above analysis was repeated for a 2-bit unit cell with four reflection phase states $(0°, 90°, 180°, 270°)$. The results show single-beam radiation and beam steering for two different applied patterns, as demonstrated in Figure 3.8.

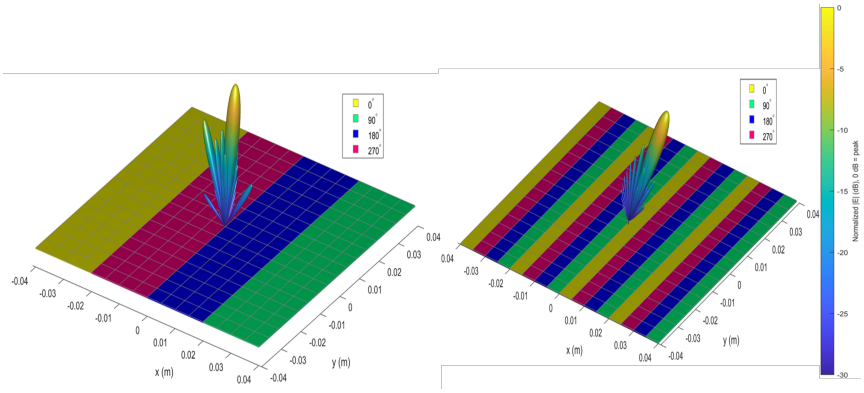


Figure 3.8: Single-beam radiation and beam steering obtained by applying different patterns on a 2-bit array.

Chapter 4

Reconfigurable Arrays Using Semiconductor Switches

4.1 Introduction

The growing demand for multifunctional, adaptable, and spectrum-efficient wireless systems has driven antenna technology beyond conventional fixed designs. In modern applications ranging from cognitive radio and 5G/6G communications to satellite payloads and advanced radar, antenna systems must support higher data rates, broader bandwidths, and enhanced polarization diversity to improve link reliability and spectral efficiency. Dual-polarized reconfigurable reflectarray antennas are particularly attractive for their ability to transmit and receive orthogonal polarizations simultaneously, effectively doubling channel capacity and improving system throughput.

Reconfigurable reflect/transmit array antennas have emerged as a powerful solution, capable of dynamically altering key radiation characteristics such as beam direction in

real time. The integration of semiconductor technologies, including PIN diodes, varactor diodes, RF MEMS switches, and CMOS-based circuits, lies at the heart of this adaptability. These active components serve as control nodes, enabling fast and precise tuning of the unit cell or array, which in turn supports phase control, beam steering, and polarization switching.

This chapter presents the design, analysis, and realization of a wideband dual-polarized reconfigurable reflectarray (RRA) and transmitarray (RTA) by employing semiconductor switches. The chapter begins with the design of a wideband dual-polarized RRA at the Ku frequency band. All steps of the unit cell design will be discussed. Simulation and experimental results are provided to validate the proposed design, demonstrating its ability to combine wideband performance with dual-polarization reconfigurability. Moving forward, the design of a wideband dual-polarized RTA will be discussed.

4.2 Wideband Dual-Polarized RRA Design

With the growing demand for higher data rates and broader bandwidth in modern communication systems such as satellite communications, radar, and wireless networks, wideband antennas have become indispensable. At the same time, polarization diversity enhances signal quality, improves link reliability, and can double channel capacity. In particular, dual-polarized reconfigurable reflectarray antennas are particularly attractive for their ability to transmit and receive orthogonal polarizations simultaneously, effectively doubling channel capacity and improving system throughput. While each of these capabilities, namely wideband operation and dual polarization, has been extensively studied, their combined implementation in a reconfigurable reflectarray remains challenging.

Enhancing the bandwidth of reflectarray antennas has been a primary focus in many

studies, given the increasing demand for high data-rate applications. In most of reconfigurable architectures, phase tuning is accomplished by shifting the unit cell's resonance frequency, which inherently results in a narrow operational bandwidth due to the fact that the unit cell structure is the main limiting factor of the array bandwidth [61]. To overcome this limitation, various techniques have been proposed. For example, [42] employs a multi-resonance configuration to achieve a 1-dB gain bandwidth of 22%, while [62] utilizes a magneto-electric dipole in the unit cell design, resulting in 22.5% 1-dB gain bandwidth. A different approach was proposed in [63] by using polarization rotation technique. The reflected wave is rotated by $-90°/+90°$ relative to the y-polarized incident wave, providing a 180° phase difference between states and achieving a 1-dB gain bandwidth of about 12%.

In parallel, other studies have focused on enabling dual-polarization capability, which enhances link reliability and spectral efficiency through the use of orthogonal polarizations. In [44] and [64], dual-polarized unit cells were proposed using MEMS switches and PIN diodes, respectively. However, these designs were not validated at the array level and lack practical implementation in array fabrication. A more complete approach was presented in [65], where a dual-polarized reflectarray was fabricated and experimentally verified. Nevertheless, these designs often involve trade-offs among bandwidth, the number of tuning elements, fabrication complexity, and control network design. These limitations underscore the need for further research to improve both the radiation performance and practical feasibility of reconfigurable dual-polarized reflectarrays.

Although wide bandwidth and dual polarization have been extensively studied individually, achieving both simultaneously in a reconfigurable reflectarray remains a significant challenge. Only a few studies have addressed these features together. In [66], a "receiving-phase shift-transmitting" unit cell was introduced, offering 1-bit phase resolution through polarization rotation and achieving a 15.4% 1-dB gain bandwidth. However, the use of

PIN diodes mounted on the ground plane and a non-integrated DC bias circuit with stamp vias complicated the fabrication process. In [67], polarization twisting was realized using two pairs of PIN diodes, achieving a 180° phase shift between two states and a 12% 1-dB gain bandwidth for both polarizations. Despite this, the design required four PIN diodes per unit cell, increasing the power consumption of the array. These prior works, while promising, involve significant trade-offs between performance, complexity, and fabrication practicality, highlighting the need for more efficient wideband, dual-polarized reflectarray solutions.

To address these limitations, the proposed structure offers a wideband dual-polarized reconfigurable reflectarray based on a novel unit cell design. Wideband operation is achieved by using a polarization rotation technique instead of altering the resonance frequency of the unit cell, which inherently results in a narrow bandwidth. The unit cell achieves a stable phase difference of $180° \pm 2°$ between two states across a wide bandwidth (10 GHz - 15 GHz) using only two PIN diodes per unit cell, of which only one PIN diode is active in each state for both polarizations. This configuration allows dual-polarization control through a single control line, significantly simplifying the biasing network. In addition, the unit cell supports circularly polarized incident waves, enhancing its applicability. By combining wideband operation with handling dual-polarization, the proposed structure offers a practical and efficient solution for modern reconfigurable reflectarray applications, with reduced fabrication effort and fewer tuning elements. In what follows, the detailed design process will be discussed.

4.2.1 Primary proposed structure

Unit cell design

The primary design objective of the proposed unit cell is to support both polarizations. To achieve dual-polarization operation, a square patch antenna capable of supporting both polarizations is employed. A second design objective is wideband performance, which requires the unit cell to maintain a stable 180° phase difference between its two states over the intended frequency range. This is accomplished using a polarization rotation technique that converts an incoming y-polarized wave to an x-polarized wave, and vice versa, while realizing two distinct phase states. The procedure described in what following explains how these goals are achieved.

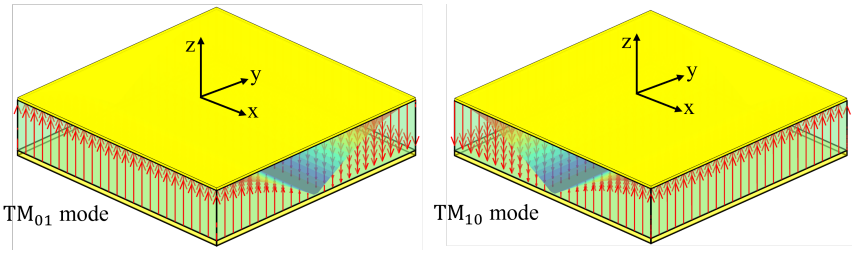


Figure 4.1: The electric field distribution of the patch dominant modes.

In a square patch antenna, the TM_{01} and TM_{10} modes are orthogonal and can exhibit identical resonance frequencies. This characteristic is a key feature of square patch antennas and is commonly utilized in dual-polarization designs. The electric field distributions of these modes are characterized by nulls along the patch centerline and out-of-phase behavior across either side, as illustrated in Figure 4.1. The proposed unit cell leverages these properties to realize two distinct phase states by exciting and converting these orthogonal modes together.

To achieve this, the square patch unit cell is configured within a multilayer structure comprising three dielectric substrates and is designed to operate at 12 GHz. Two RTDroid 5880 substrates (thicknesses of 0.208 mm and 0.82 mm) with low dielectric permittivity ($\varepsilon_r = 2.23$), which is desirable for achieving higher bandwidth, are used. A RO4003 substrate with $\varepsilon_r = 3.55$ and a thickness of 0.508 mm is employed in the bottom layer to achieve a more compact feeding network

Both the TM_{01} and TM_{10} modes are excited independently by y-polarized and x-polarized incident waves respectively, using unit cell boundary condition in the CST microwave studio software. To enable the mode conversion, and achieving distinct phase states accordingly, two independent excitation mechanisms are required to ensure selective excitation and enable simultaneous mode conversion. For this purpose, two metallic vias placed along the y-axis and penetrating through the ground layer are employed for TM_{01} excitation, while a L-probe oriented perpendicular to the x-axis is used for TM_{10} excitation. as shown in Figure 4.2 (a). The L-probe feeding is chosen for its ability to provide good bandwidth in multilayer structures [68], which will be required later when implementing the polarization conversion mechanism.

Due to their orthogonal nature, the excitation mechanism for one mode does not significantly disturb the other. Specifically, the addition of the L-probe when TM_{01} mode is excited, or the addition of vias when the TM_{10} mode is excited preserves the original electric field distribution of each mode, as shown in Figure 4.2 (b). This can be observed in the reflection magnitude and phase of the unit cell under x-polarized and y-polarized incident waves, as shown in Figure 4.2 (c) and Figure 4.2 (d). These responses remain nearly unchanged after introducing the excitation method for the other mode, confirming the independence of the two excitations.

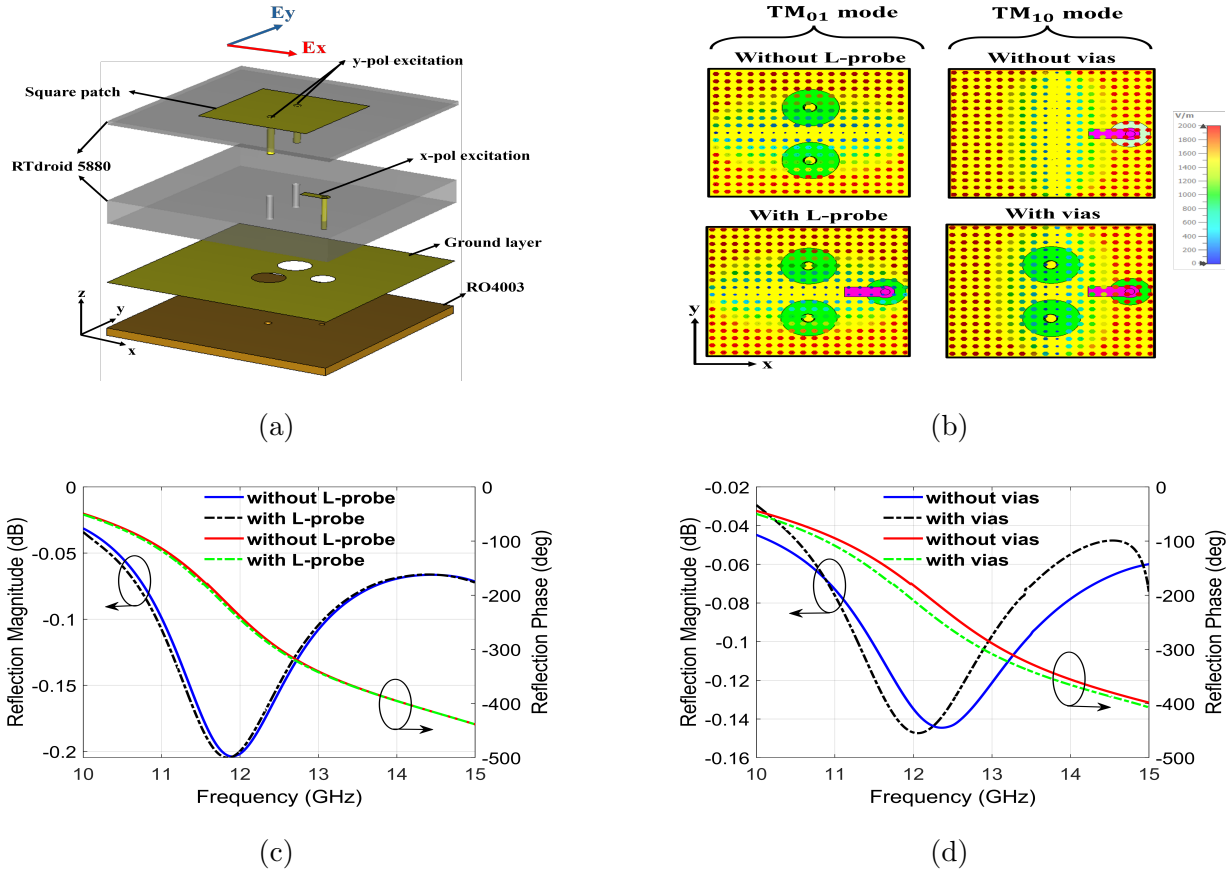
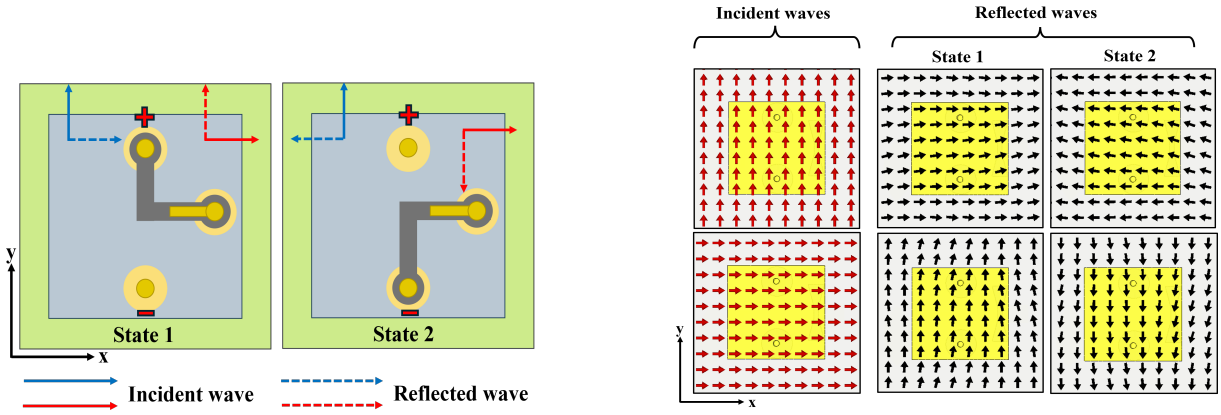


Figure 4.2: (a). The square patch unit cell with two excitation mechanism. (b) Field distribution of each mode with and without the other mode excitation mechanism. (c) Reflection magnitude/phase under y-polarized incident wave (related to TM_{01}). (d) Reflection magnitude/phase under x-polarized incident wave (related to TM_{10}).

To enable the joint conversion of these modes and achieve two discrete phase states, a microstrip line is used on the bottom layer of the RO4003 substrate to connect the vias and the L-probe. Figure 4.3 (a) illustrates this switching configuration for both states, along with the incident and reflected wave behavior for both polarization.



(a) (b)

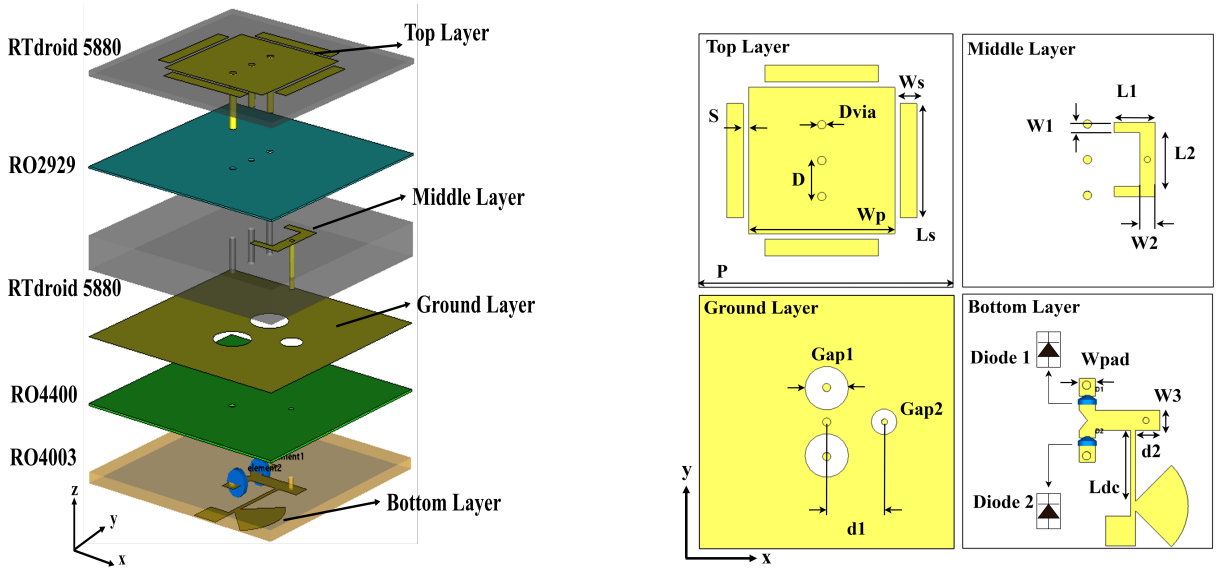
Figure 4.3: (a) The process of achieving two states. (b) Incident and reflected waves in two states for both polarizations.

For state 1, when the patch is excited with a y-polarized incident wave, the TM_{01} mode of the patch is excited and vias along the y-axis will be excited by 180° phase difference, as indicated by the relevant positive and negative signs in Figure 4.3 (a). This is due to the out-of-phase characteristic of electric filed in TM_{01} mode. By connecting the positive via along the y-axis to the L-probe by a microstrip line, the TM_{10} mode will be excited, causing radiation back in x-polarization. Therefore, the y-polarized incident wave will be radiated back in x-polarization. Concurrently, an x-polarized incident wave will excites TM_{10} mode, and it converts to the TM_{01} mode, causing radiation back in y-polarization.

In state 2, the negative via along the y-axis is connected to the L-probe. Consequently, the y-polarized incident wave will be radiated back in x-polarization with 180° phase difference compared to state 1. For the x-polarized incident wave, the connection to the lower via along the y-axis results in excitation of the patch in the opposite direction, leading to a 180° phase difference compared to state 1. In summary, the operational mechanism in-

volves the conversion of the y-polarized incident wave to an x-polarized reflected wave with two distinct phase states, and vice versa. To evaluate the process, the reflected electric field of each state are depicted in Figure 4.3 (b) at one instant in the constant z-plane above the unit cell (z= 5mm). The unit cell is illuminated with both x and y-polarized incident waves. The reflected electric fields clearly show that for each incident wave, the reflected electric field for both states have 180° phase difference, as expected from the principles of operations.

Regarding the operating principles explained above, the structure shown in Figure 4.4 is proposed. It comprises three substrates, namely RTDroid 5880 (10 mil and 61 mil) and RO4003 (20 mil), and four metallic layers. A square patch is used as the receiving/transmitting element, with its dimensions chosen to operate at 12.5 GHz. It is also loaded with four parasitic patches that are used to increase the bandwidth. Two vias in the y direction are used for y-polarization excitation, and L-probe feeding with a twin geometry is used for x-polarization excitation. The middle via, which connects the square patch to the ground layer, provides a DC current path for the diodes to the ground. Since the electric field is zero at the center for both modes, this via does not affect the unit cell's electromagnetic characteristics. Two diodes, D1 and D2, are used to switch between two states. For each state, only one diode is active for both polarizations. In addition, only one control signal is used to turn the diodes on and off, which considerably simplifies the design of the control system. To prevent the DC pad from interfering with RF performance, a radial capacitor with a quarter-wavelength line designed at center frequency (13 GHz) is used. The dimensions of microstrip line and twin L-probe feed (width and length) are optimized through full-wave simulation to achieve the desired response. Table 4.1 shows the optimized design parameters of the proposed structure.



(a) (b)

Figure 4.4: The proposed unit cell structure. (a) 3-D view. (b) Layer description

Table 4.1 Dimensions of the proposed unit cell.

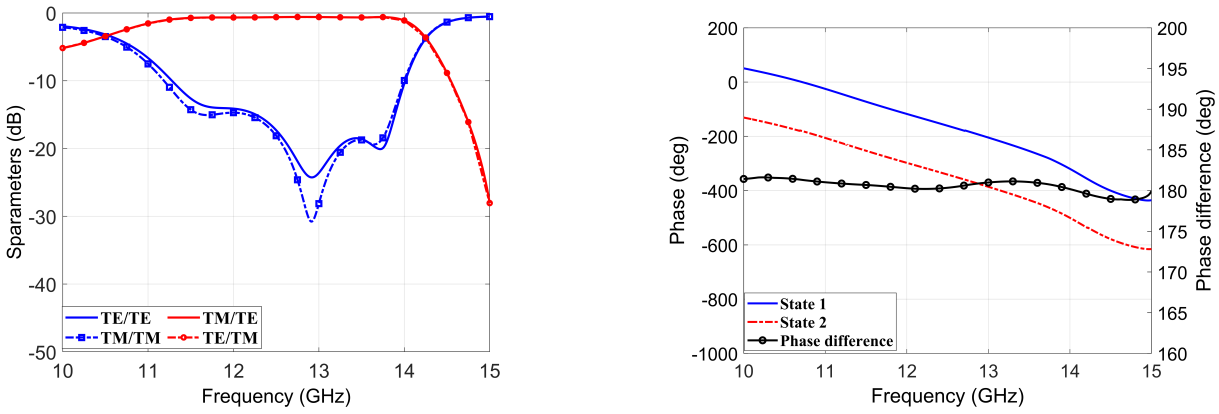
Parameter	P	Wp	D	Dvia	S	Ls	Ws	L1	W1	L2	W2
Value (mm)	13	6.9	1.7	0.4	0.25	5.4	0.8	1.97	0.5	2.6	0.75
Parameter	d1	Gap1	Gap2	W3	Wpad	Ldc	d2				
Value (mm)	2.9	2.2	1.3	1	0.8	3.5	1.2				

To simulate the proposed structure, CST Microwave Studio software is used with unit-cell boundary conditions. The proposed structure is illuminated with TE (y-polarized) and TM (x-polarized) plane waves at normal incidence. To incorporate the diode into the

simulation, its equivalent circuit model is employed. The MACOM MADP-00097-1402 PIN diode, known for its good performance within the desired frequency band, is used. According to the manufacturer's datasheet, an RL equivalent circuit ($R = 5\ \Omega$, $L = 30$ pH) is used for the ON state, while an LC equivalent circuit ($C = 25$ fF, $L = 30$ pH) represents the OFF state.

As discussed earlier, the upper and lower y-axis vias experience a 180° phase difference in excitation. When D1 is active (state 1), the upper y-axis via is connected to the L-probe through an x-axis via. Therefore, a y-polarized incident wave will be radiated back in x-polarization, and vice versa. When D2 is active (state 2), the lower y-axis via, which has a 180° phase difference, connects to the L-probe. This results in a y-polarized wave radiating back with a 180° phase difference. For an x-polarized incident wave, the lower y-axis via, excited in the opposite sense compared to state 1, causes the radiated y-polarized wave to differ by 180° in phase compared to state 1.

Figure 4.5 (a) shows the simulation results of polarization conversion for the proposed structure. TE/TE (TM/TM) represents the reflected wave from a y-polarized (x-polarized) incident wave. Accordingly, TM/TE (TE/TM) represents polarization conversion. The reflection coefficient for TE/TE (TM/TM) is less than -10 dB within the 11.2 GHz to 14.2 GHz frequency range, with TE/TM (TM/TE) conversion loss less than 1 dB. This indicates good polarization conversion within the specified frequency range. The introduced loss is mainly related to the ohmic loss of the connection path and the PIN diode loss. The two phase states and their difference are shown in Figure 4.5 (b). It is observed that the phase difference between the two states is $180° \pm 2°$ over the entire 11.2 GHz to 14.2 GHz band. Simulation results show a relative bandwidth of around 25% for both polarizations, which is a considerable achievement.



(a) (b)

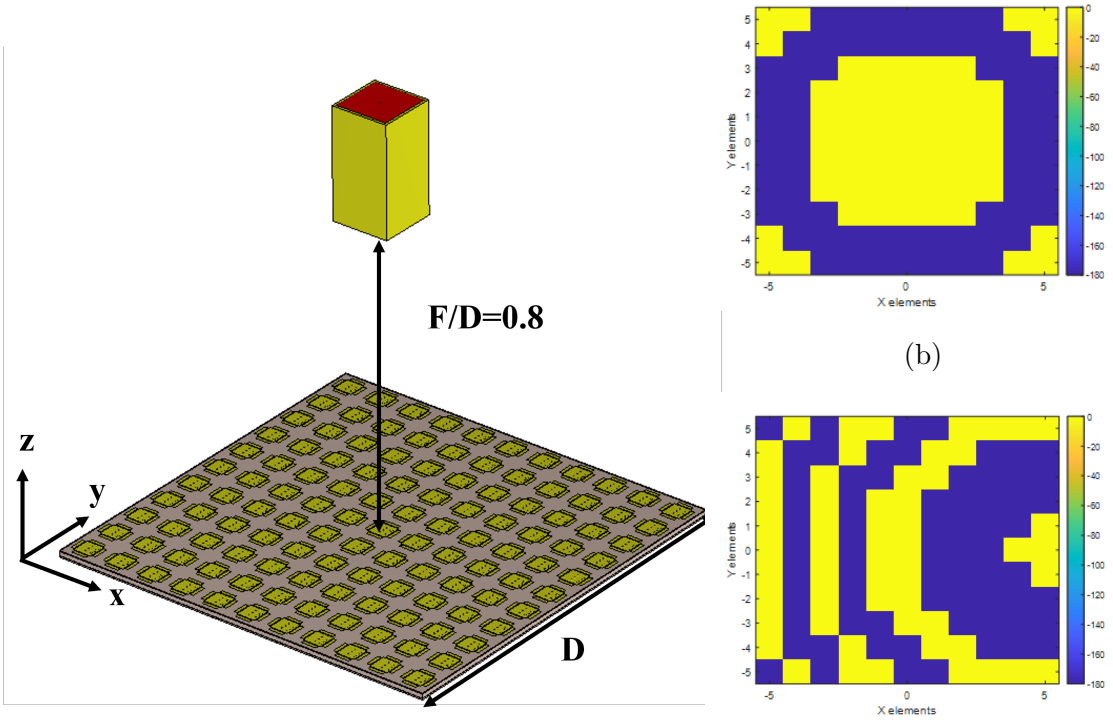
Figure 4.5: (a) S-parameters of the proposed unit cell. (b) Phase difference between two states.

Array simulation

To evaluate the proposed unit cell performance, it was utilized in an 11 × 11 elements array structure. Figure 4.6 (a) shows array structure in CST using proposed unit cell. The required phase distributions shown in Figure 4.6 (b)-(c) were calculated at 12 GHz to collimate the beam to (θ_0,φ_0)=(0°,0°) and (θ_0,φ_0)=(30°,0°) directions respectively, using the Equation 4.1.

$$\varphi_{1-bit} = \begin{cases} 0° & -180° < \phi_R \leq 0° \\ -180° & -360° < \phi_R \leq -180° \end{cases} \tag{4.1}$$

where ϕ_R is the continuous reflection phase expressed in Equation 3.4. The array is illuminated with a square waveguide which supports two excitation modes. The F/D which affects the array efficiency is set to 0.8.



(a) (b) (c)

Figure 4.6: (a) Array structure. (b) Required phase distribution for $(\theta_0, \phi_0) = (0°, 0°)$. (c) Required phase distribution for $(\theta_0, \phi_0) = (30°, 0°)$).

The radiation patterns in XoZ plane ($\phi_0 = 0°$) is demonstrated in Figure 4.7 at $\theta_0 = 0^0$ and $\theta_0 = 30^0$ angles for both polarizations. Simulation results show good 1-dB gain bandwidth over 11 GHz - 13.5 GHz frequency range with 20% relative bandwidth for both polarizations. Simulated gain at 11 GHz is 17 dBi for both polarizations. There is a deviation around 5° from the designed beam direction in y-polarization at 11.5 GHz. This may relate to the phase distribution regarding the fact that for each frequency, phase distribution should be calculated individually. In this simulation only one phase distribution was used for the entire frequency band because only overall unit cell evaluation

was intended. As presented in simulation results, the proposed structure shows acceptable radiation performance in the desired frequency range.

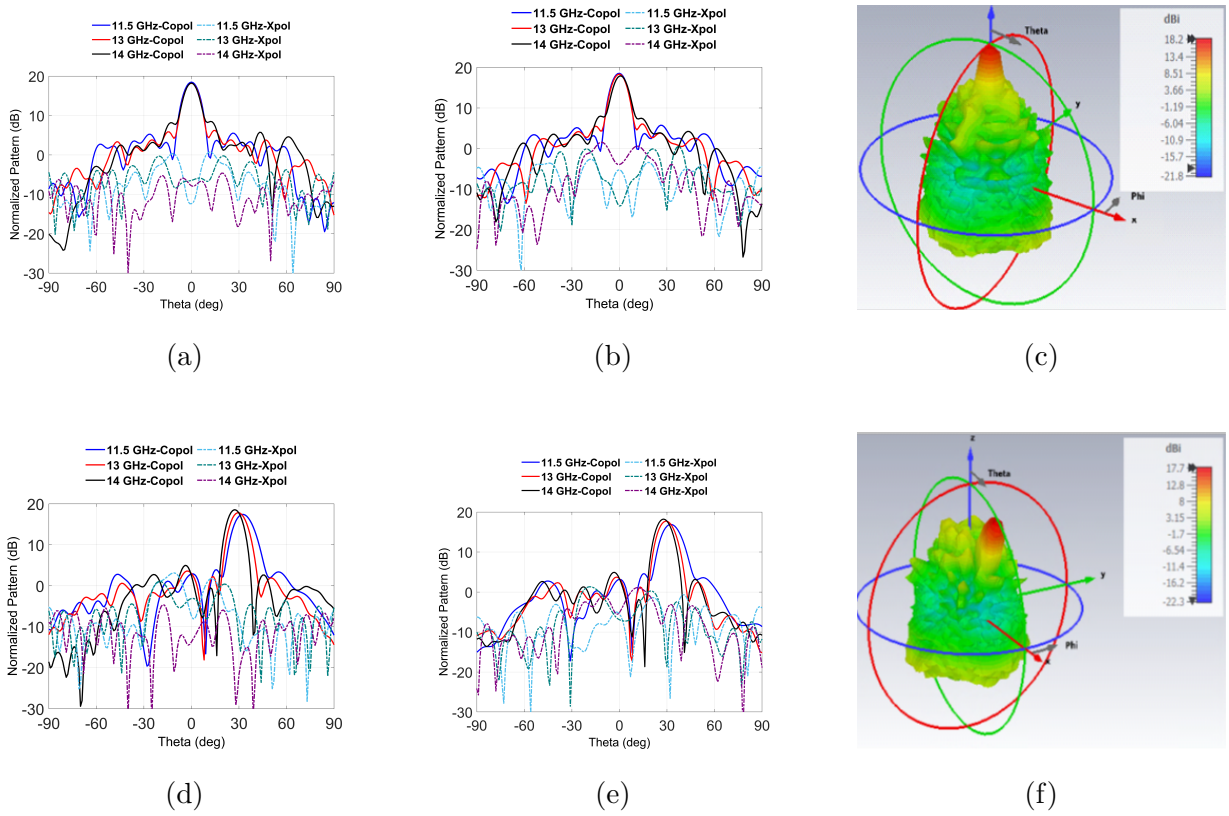


Figure 4.7: (a) Radiation pattern at $\theta_0 = 0^0$, x-polarization. (b) Radiation pattern at $\theta_0 = 0^0$, y-polarization. (c) 3-D radiation pattern at $\theta_0 = 0^0$. (d) Radiation pattern at $\theta_0 = 30^0$, x-polarization. (e) Radiation pattern at $\theta_0 = 30^0$, y-polarization. (f) 3-D radiation pattern at $\theta_0 = 30^0$.

4.2.2 Modified proposed structure

Unit cell design

The primary design which is a multi-layer structure consisting of three substrates and four metallic layers achieved 20% 1-dB gain bandwidth for both polarizations. However, despite the substantial gain bandwidth, the structure required a complex and costly fabrication process due to the use of blind vias. Furthermore, the array performance was not verified by fabrication and measurement. The current design simplifies the structure, aiming to reduce fabrication complexity and cost. Additionally, the array simulation results have been validated through measurements. Figure 4.8 illustrates the proposed unit cell structure. This structure features two substrates and three metallic layers. The utilized substrates are RTDroid 5880 (0.82 mm) and RO4003 (0.508 mm) which are laminated together with a RO4400 (0.1 mm) prepreg layer.

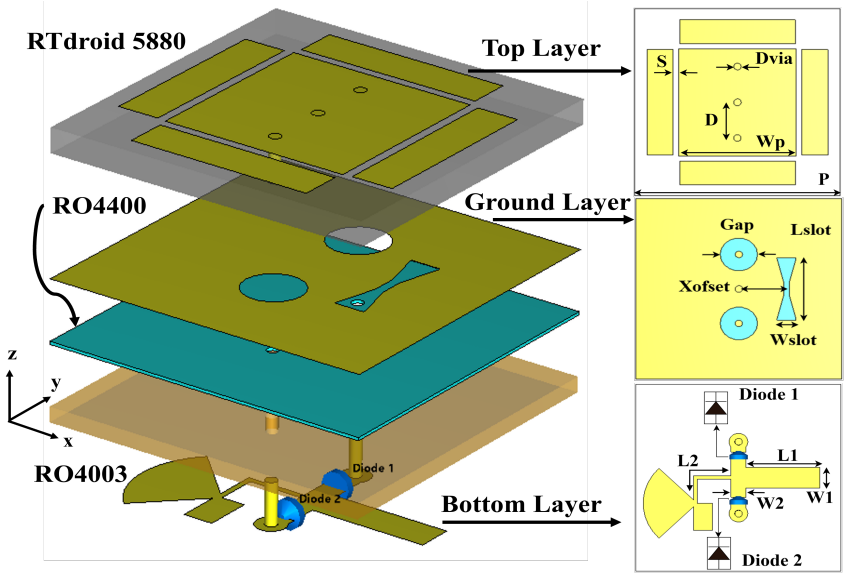


Figure 4.8: The proposed modified structure.

Table 4.2 Dimensions of the modified proposed unit cell.

Parameter	P	Wp	D	Dvia	S	Lslot	Wslot
Value (mm)	11	6.3	2.1	0.4	0.3	3.8	1.1
Parameter	X_offset	Gap	L1	W1	L2	W2	Larc
Value (mm)	2.6	1	4	1.2	3.5	0.8	1.8

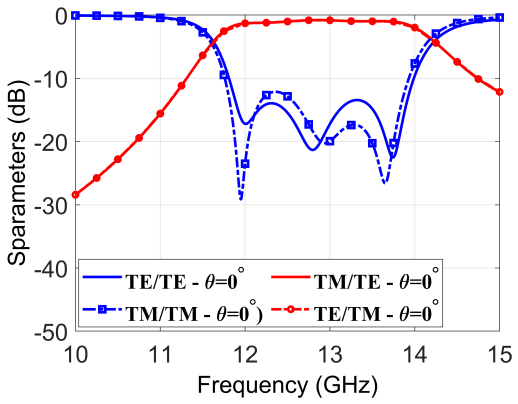
n the top layer, the square patch loaded with parasitic strips serves as the transmit/receive element, as in the primary proposed structure. Instead of L-probe feeding, a bowtie-shaped slot, oriented perpendicular to the x-axis and optimized to maximize polarization conversion bandwidth, is employed for x-polarization excitation. For y-polarization excitation, two vias along the y-axis are used, which extend through the ground plane and connect to the bottom layer, similar to the primary structure. As in the primary design, two PIN diodes are used as switches in the bottom layer, with a single DC bias line. By applying a positive or negative DC voltage, only one diode is activated in each state for both polarizations. The middle via, which connects the square patch to the ground layer, provides a DC current path to the ground. As previously mentioned, this via does not affect the unit cell's electromagnetic characteristics, as the electric field is zero at the center for both modes. The dimensions of the microstrip line that provides the connection between the two excitations are optimized to achieve acceptable matching for polarization conversion. Table 4.2 presents the optimized dimensions in the modified proposed structure.

In State 1, Diode 1 is activated with a positive voltage bias, connecting the microstrip

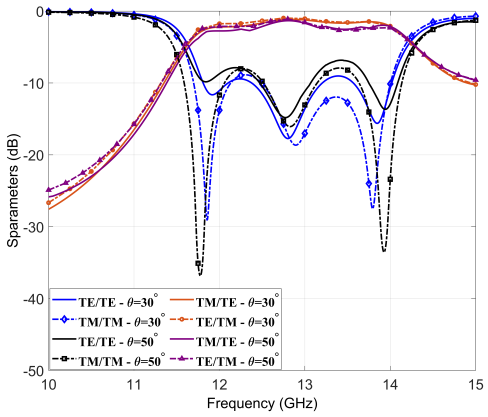
line to the upper via along the y-axis. This configuration reflects a y-polarized incident wave back as an x-polarized wave through the slot, and vice versa. In State 2, a negative voltage activates Diode 2, causing the y-polarized wave to reflect back as an x-polarized wave with a 180° phase shift relative to State 1. Similarly, an x-polarized incident wave reflects back as a y-polarized wave with a 180° phase shift, achieved by exciting the lower via along the y-axis in the opposite sense compared to State 1. The proposed unit cell was simulated in CST using the same boundary conditions and excitation. The circuit model parameters of the MACOM MADP-00097-1402 PIN diode were used for the ON and OFF states.

The reflection performance of the unit cell is demonstrated in Figure 4.9 (a)-(b), showing polarization conversion under both normal and oblique incidence. As explained earlier,TE/TE (TM/TM) shows reflection from the y-polarized (x-polarized) incident wave. Accordingly, TM/TE (TE/TM) represents transformation of the y-polarized (x-polarized) incident wave to the x-polarized (y-polarized) reflected wave. Under normal incidence, the reflection coefficient remains below –10 dB within the 11.8 GHz to 14 GHz frequency range, with an insertion loss of less than 1.6 dB across the entire band, corresponding to a relative bandwidth exceeding 15%. Under oblique incidence, while the performance degrades, the unit cell still maintains acceptable characteristics, with the reflection coefficient remaining below –7 dB across the entire frequency range and the maximum insertion loss increasing to 2.8 dB at an incident angle of 50°. Figure 4.9 (c)-(d) demonstrates the phase of two states and the difference between them, which is $180° \pm 2°$ for normal incidence and reaches $180° \pm 6°$ for oblique incidence within 10 GHz-15 GHz frequency range. It shows stable and accurate phase difference between two states over a wide frequency range, which is achieved by using the out-of-phase characteristic of the electric field in the patch dominant mode. The limiting factor is the polarization conversion bandwidth, which can

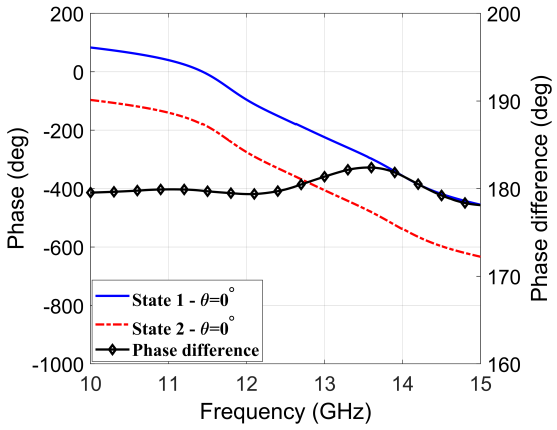
be increased by improving the matching network or using structures with more layers, as discussed in primary design.



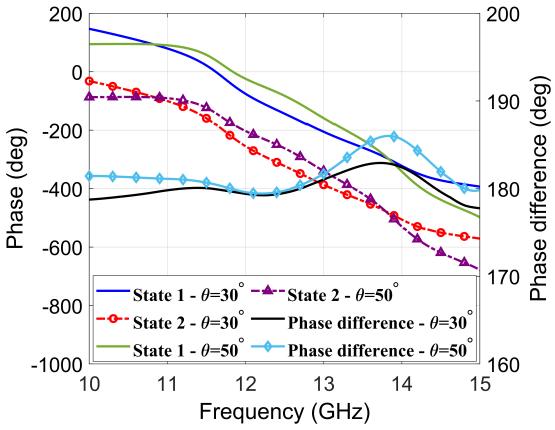
(a)



(b)



(c)



(d)

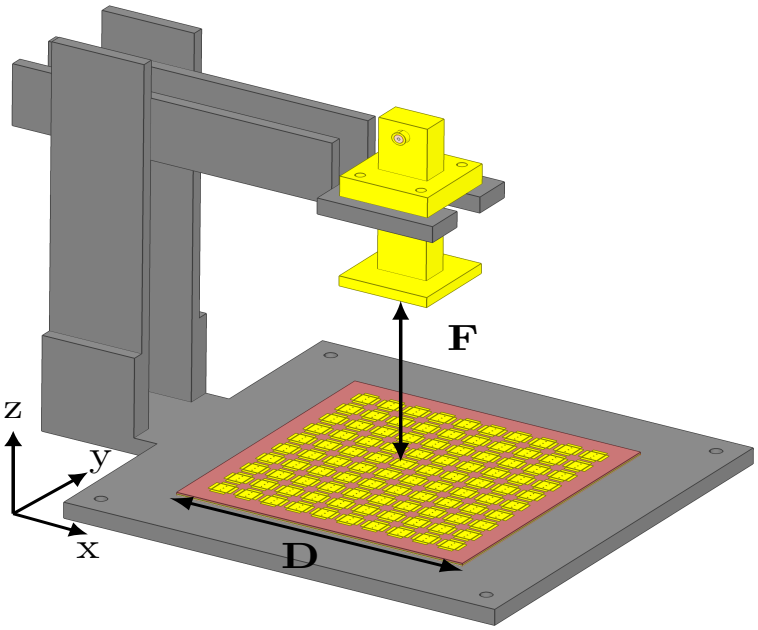
Figure 4.9: S-parameters of the proposed unit cell at (a) normal incidence and (b) oblique incidence. Phase difference between two states at (c) normal incidence and (d) oblique incidence.

Array design and fabrication

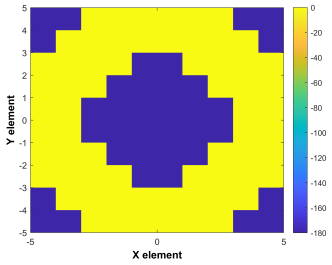
By employing the proposed unit cell, a 10×10 elements RRA with an aperture size of $11cm \times 11cm$ $(4.7\lambda_0 \times 4.7\lambda_0)$ is designed and simulated to evaluate its beam steering performance. Figure 4.10 (a) shows the array structure in CST software which is illuminated by a WR75 waveguide source. The location of the feed plays a crucial role in the efficiency of a reflectarray. As discussed in [69], the aperture efficiency (η_a) is related to spillover efficiency (η_s), and illumination efficiency (η_i). A trade-off exists between these parameters, which should be optimized by adjusting the focal-to-diameter (F/D) ratio, where F represents the focal point, and D is the side length of the array. In this design, the F/D ratio set to 0.9, and the waveguide source is placed in a normal position to the array on dielectric fixture. The required phase distributions shown in Figure 4.10 (b)-(d) are calculated using Equation 4.1 at 13 GHz for three desired directions which are $\theta_0 = 0^0$, $\theta_0 = 30^0$ and $\theta_0 = 50^0$ respectively in the XoZ plane ($\phi_0 = 0°$).

To validate the design of the reconfigurable reflectarray (RRA), a 10×10 element array was fabricated, along with the associated DC bias circuit, using printed circuit board (PCB) technology. The fabricated array consists of RTDroid 5880 (thickness = 0.82 mm) and RO4003 (thickness = 0.508 mm) substrates, which are bonded together by an RO4400 prepreg layer. Two PIN diodes are soldered onto the bottom layer of each unit cell, as demonstrated in Figure 4.11 (a). To excite the array, a WR-75 waveguide source is positioned normal to the structure. For measurements of both polarization states, the waveguide source is rotated by 90° . Figure 4.11 (b) shows the fabricated prototype mounted on a 3D-printed fixture.

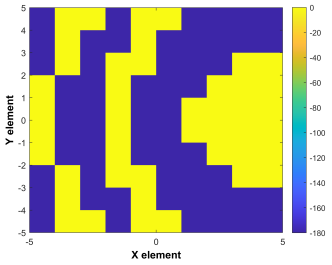
The DC bias circuit contains 100 identical DC units to control each unit cell in the array individually, as shown in Figure 4.11 (c). Each DC unit is fed by two positive and



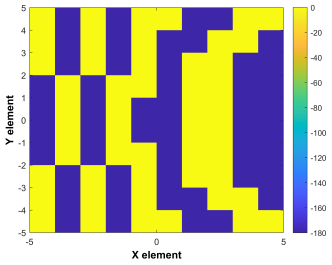
(a) Top figure



(b)



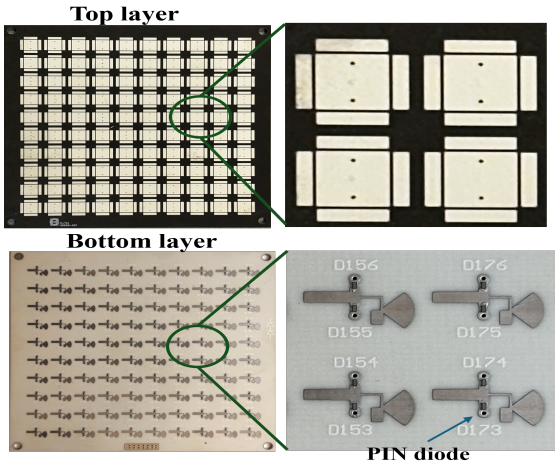
(c)



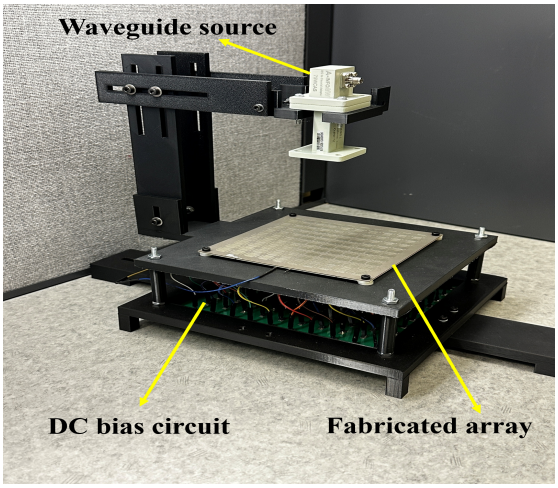
(d)

Figure 4.10: (a) 3-D view of the modified array. Required phase for (b) $\theta_0 = 0^0$. (c) $\theta_0 = 30^0$. (d) $\theta_0 = 50^0$

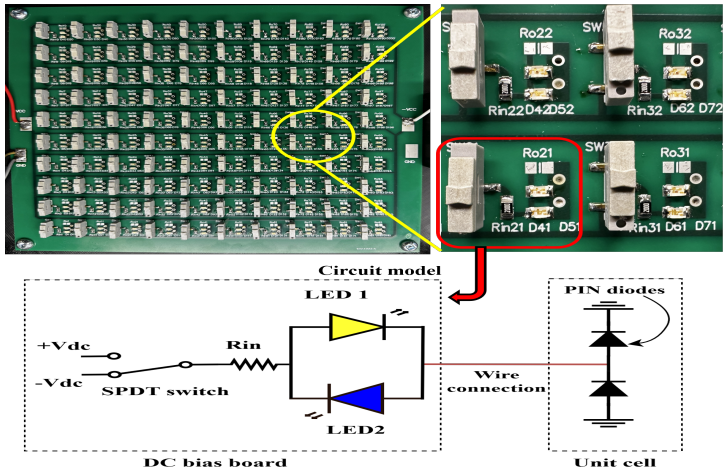
negative bias lines, connected to a SPDT switch. These bias lines are common for all DC units. The DC unit output is connected to the specified unit cell in the array section by



(a)



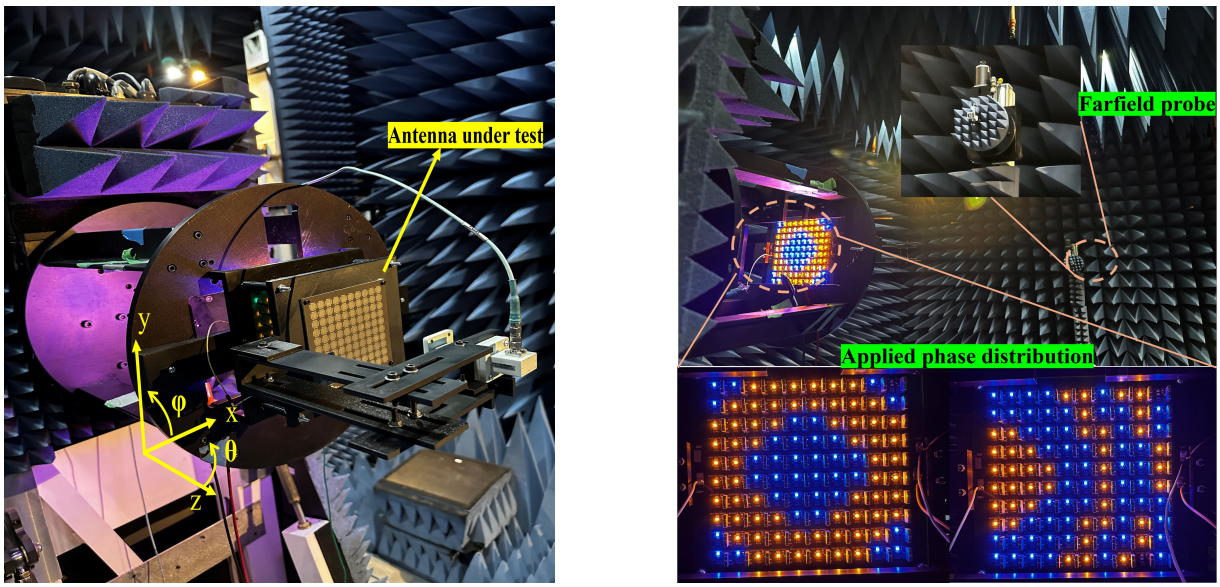
(b)



(c)

Figure 4.11: (a) Top and bottom layers of the fabricated array. (b) Fabricated prototype. (c) The DC circuit board of the array.

a wire connection. By changing the switch configuration, two different phase states are obtained. To identify the active state for each unit cell, two light emission diodes (LED) are used as indicator in each DC unit.



(a) (b)

Figure 4.12: Antenna under test (AUT) in the anechoic chamber. (a) Front view. (b) Back view.

Figure 4.12 (a) shows the fabricated RRA placed in the anechoic chamber for far-field measurement. Different phase distribution applied to the array to tilt the beam toward the specified direction, as demonstrated in Figure 4.12 (b). The yellow LEDs indicate state 1 (0°), while the blue ones indicate state 2 (−180°). The radiation pattern was measured for three different radiation angles. For each angle, the measurement was done for several frequency points ranging from 12 GHz to 14 GHz.

The simulated and measured radiation patterns for both polarizations at three radiation

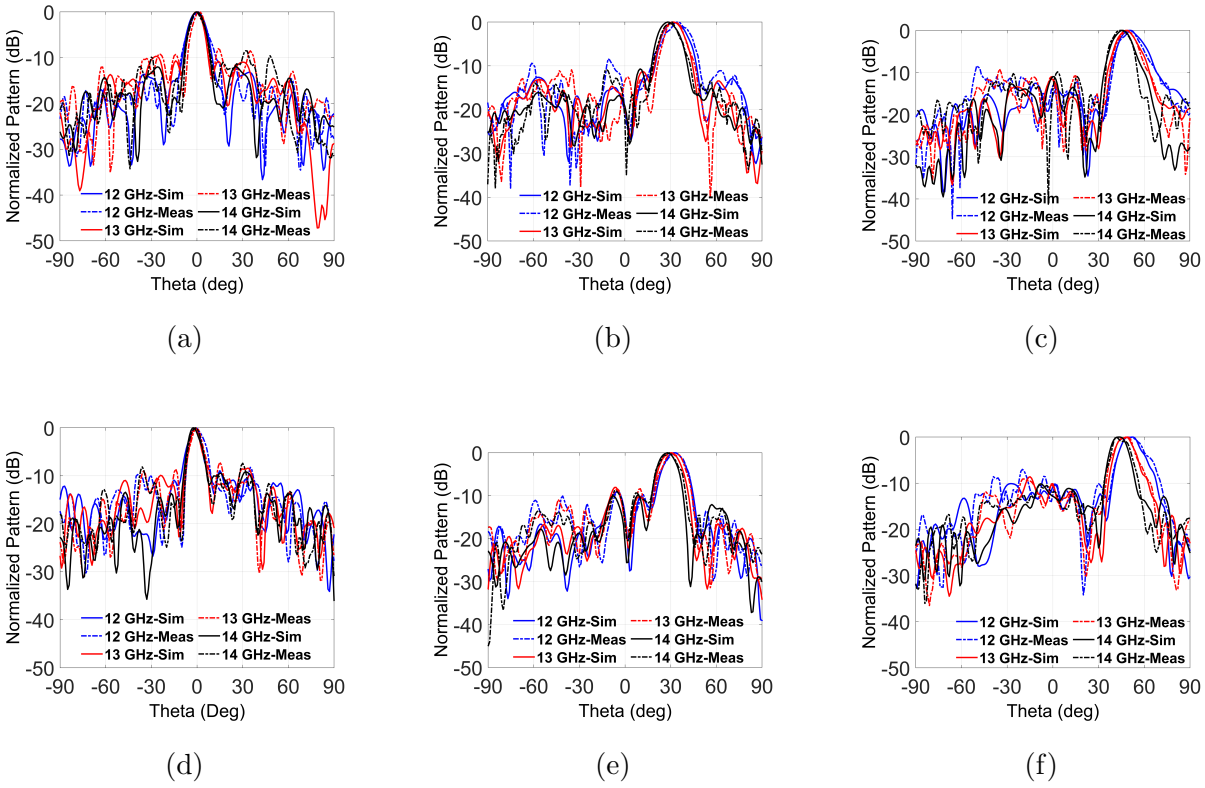


Figure 4.13: Simulated and measured radiation pattern for three arrays. (a) $\theta_0 = 0°$, x-polarization. (b) $\theta_0 = 0°$, Y-polarization. (c) $\theta_0 = 30°$, x-polarization. (d) $\theta_0 = 30°$, y-polarization. (e) $\theta_0 = 50°$, x-polarization. (f) $\theta_0 = 50°$, y-polarization.

angles in the XoZ plane are shown in Figure 4.13 (a)–(f). These results demonstrate that the proposed RRA achieves effective beam steering, with radiation pattern directed towards the desired angles. The simulated and measured patterns align well across the entire operating frequency range of 12 GHz to 14 GHz. There is a deviation in the radiation angle of about 2° for $\theta_0 = 30°$, and 6° for $\theta_0 = 50°$, observed at the lower and upper bounds of the frequency range, respectively. This discrepancy is primarily attributed to the phase distribution being calculated at the center frequency. Considering (3.4), the reflection phase

is frequency dependent. In narrow-band RRA design, the required phase distribution is calculated at the center frequency of operation. However, for wideband arrays, the phase distribution can vary significantly across different frequencies within the band. To achieve optimal performance, it is better to assign distinct phase patterns for different frequencies. In this design. Despite using a single phase pattern across the frequency band, the RRA demonstrates stable performance over a wide bandwidth. More accurate radiation angles could be achieved by optimizing the phase distribution for different frequencies.

The highest measured side lobe level (SLL) is -8 dB. It is observed that employing a discrete phase distribution can degrade the array's radiation characteristics, including the SLL. Additionally, feed blockage effects should be taken into account. Although the measured SLL is relatively high, improvements may be achieved by increasing the aperture size or enhancing the number of phase states [39]. Furthermore, implementing offset feeding or improving the directivity of the illuminating source can effectively reduce the SLL.

The measured gain of three radiation angles for both polarizations at 13 GHz are shown in Figure 4.14 (a)-(b). The measured maximum x-polarized gain is about 12.6 dBi, 13.8 dBi and 12.2 dBi for $\theta_0 = 0°, \theta_0 = 30°, \theta_0 = 50°$ respectively, while the corresponding simulated values are 13.2 dBi, 14.5 dBi and 12.8 dBi. The observed gain reduction is likely attributed to feed blockage and measurement setup effects, which were not accounted for in the simulation. Furthermore, the measured cross-polarization levels remain below -13 dB across all radiation angles for both polarizations, confirming effective polarization conversion. Furthermore, under broadside radiation ($\theta_0 = 0°$), the simulated cross-polarization level in the $\phi_0 = 45°$ plane is approximately –13 dB across the operating band. This diagonal plane is important for assessing polarization purity, as it represents a mixed-polarization direction. The –13 dB level demonstrates that the design provides reasonable polarization isolation even in off-axis planes, supporting effective dual-polarized operation.

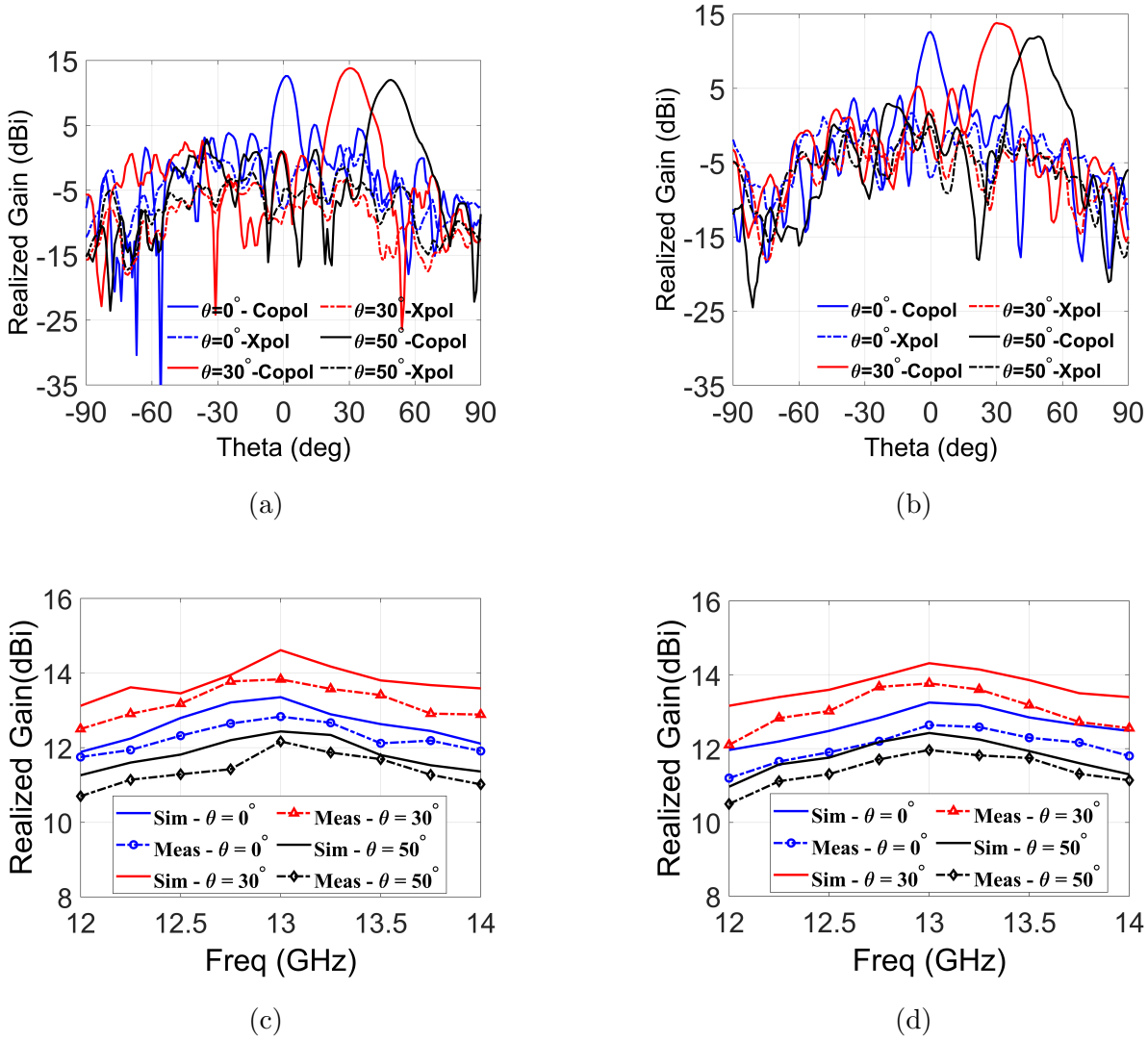


Figure 4.14: (a) Measured gains for x-polarization. (b) Measured gains for y-polarization. (c) Gain vs.frequency for x-polarization. (d) Gain vs.frequency for y-polarization

To analyze the bandwidth characteristics of the proposed RRA, the gain response over the 12 GHz to 14 GHz frequency range was evaluated, as shown in Figure 4.14 (c)-(d) at three beam directions for both polarizations. The measured 1-dB gain bandwidth of

the array is 13.7% (12.2 GHz–14 GHz), demonstrating good agreement with the simulated results. Since the proposed array can simultaneously control both polarizations with a single bias line, it is well-suited for applications involving circularly polarized (CP) incident waves. For instance, a right-hand circularly polarized (RHCP) incident wave will be reflected as a left-hand circularly polarized (LHCP) wave, and vice versa. Figure 4.15 presents the simulated radiation pattern of the array under an RHCP incident wave for both $\theta_0 = 0°$ and $\theta_0 = 30°$ angles. The results were obtained by combining both modes during post-processing in CST software. The patterns confirm that the RHCP incident wave is effectively radiated back as LHCP, with reconfigurable beam control achieved as accurately as for linear polarization.

The observed discrepancies between the measured and simulated results can be attributed to several factors, including fabrication tolerances and the influence of measurement setup components such as cables and fixtures, which were not accounted for in the simulation. To simplify the fabrication and measurement process, a waveguide source was employed in this setup. However, due to the relatively small aperture of the array, the waveguide source introduces significant blockage, as evident when comparing the measured gain with other works featuring similar aperture sizes. Additionally, the waveguide source exhibits asymmetric radiation patterns in the E-plane and H-plane, resulting in uneven amplitude excitation across the array surface in the x- and y-directions. This asymmetry likely contributes to further degradation in the array's radiation performance.

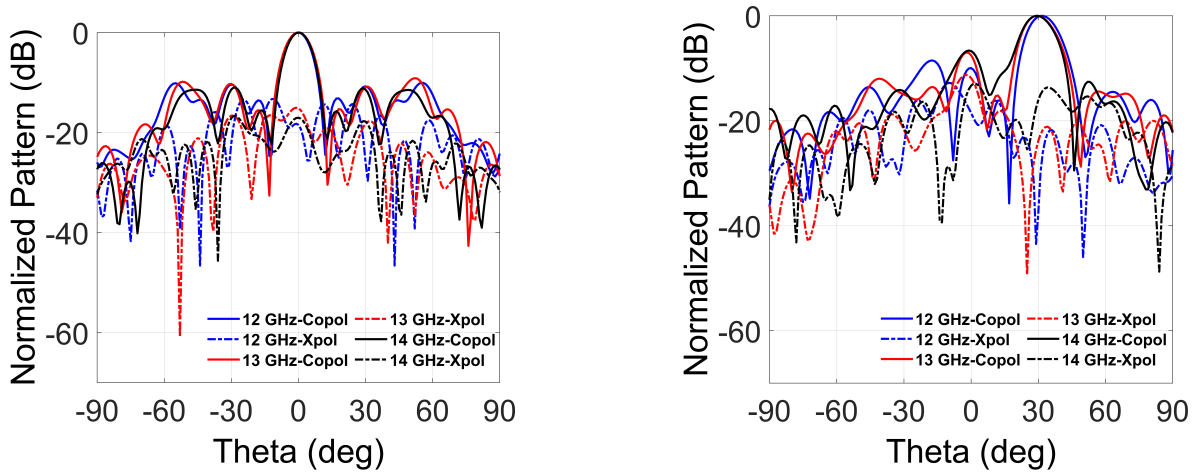


Figure 4.15: Simulated radiation pattern under RHCP incident wave. (a) $\theta_0 = 0°$. (b) $\theta_0 = 30°$

The comparison between the proposed RRA and several prior 1-bit RRA designs is summarized in Table 4.3. Compared to [66], the proposed design significantly reduces fabrication complexity by incorporating an integrated DC bias circuit, in contrast to the non-integrated approach used in that work, while achieving a comparable 1-dB gain bandwidth (13.7% vs. 15.4%). Furthermore, the proposed unit cell shows a more accurate and stable phase difference between two states. Relative to [67], it delivers improved bandwidth performance using only half the number of PIN diodes per unit cell and features a simpler structural design. On the other hand, the proposed structure exhibits slightly lower aperture efficiency, primarily due to gain reduction caused by feed blockage. This limitation can be addressed by employing a higher-gain feed source or using an offset feeding scheme to minimize blockage. Compared to the other referenced works, which focus on addressing either wide bandwidth or dual polarization individually, the proposed design effectively

integrates both features, offering a practical and efficient solution for reconfigurable reflectarray applications.

Table 4.3 Comparison between the proposed RRA and related works

Ref.	[42]	[65]	[67]	[66]	**This work**
Frequency (GHz)	12.5	7.45	13.5	12.5	**13**
Number of array elements	16×16	20×20	10×10	16×16	$\mathbf{10 \times 10}$
Number of PIN diodes	1	4	4	2	**2**
Polarization	LP	DP/CP	DP/CP	DP/CP	**DP/CP**
Peak gain (dBi)	20.1	22	17.3	18	**13.8**
Aperture efficiency (%)	24	16.35	12.5	15	**8.9**
1-dB gain bandwidth (%)	22.3	<6	12	15.4	**13.7**
Fabrication aspects	• Three substrates • Integrated DC bias circuits	• Two substrates • Integrated DC bias circuits	• Three substrates • Non-integrated DC bias circuit	• Three substrates • Non-integrated DC bias circuit	• **Two substrates** • **Integrated DC bias circuit**

Array simulation under plane wave excitation

The designed and fabricated array was considered in reflectarray mode, which is for beamforming applications. As discussed in the literature review, in beamforming applications the source is in the near field of the array, and the spatial phase delay from the source to

the array should be taken into account for beam collimation, as discussed in the analysis. In anomalous reflection applications, the array is excited with a plane wave, which is located far away from the array. In this case, the spatial phase delay is not considered, since all array elements will approximately receive the same wavefront.

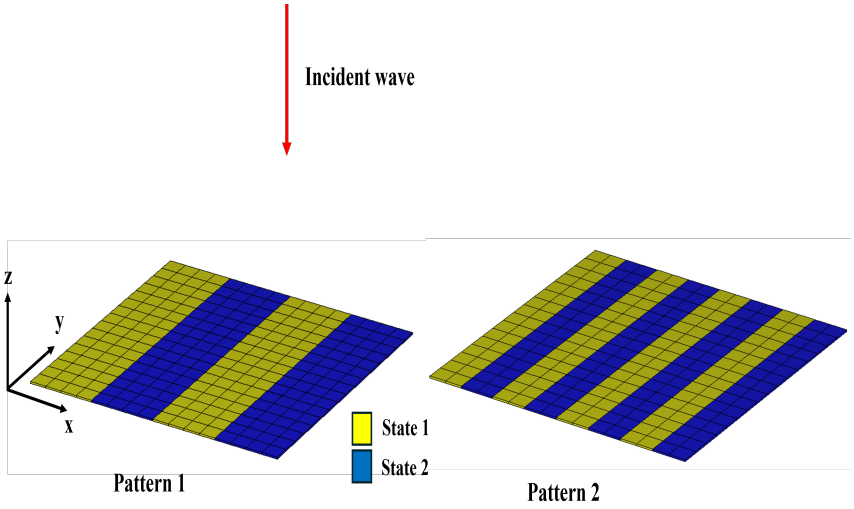


Figure 4.16: The proposed unit cell in an array under plane wave excitation.

Herein, the proposed unit cell was employed in a 16×16 array, and two different phase distributions were applied over the array surface. The array was excited with a plane wave source normal to the array, as demonstrated in Figure 4.16. Two distinct phase distributions are applied to achieve different radiation patterns. As shown in Figure 4.17, the direction of the beam changes by applying distinct phase distributions. The radiation pattern is symmetric, which means the reflected wave has two main beams. This is a natural characteristic of 1-bit reflective arrays when they are excited with plane waves, as discussed in [60].

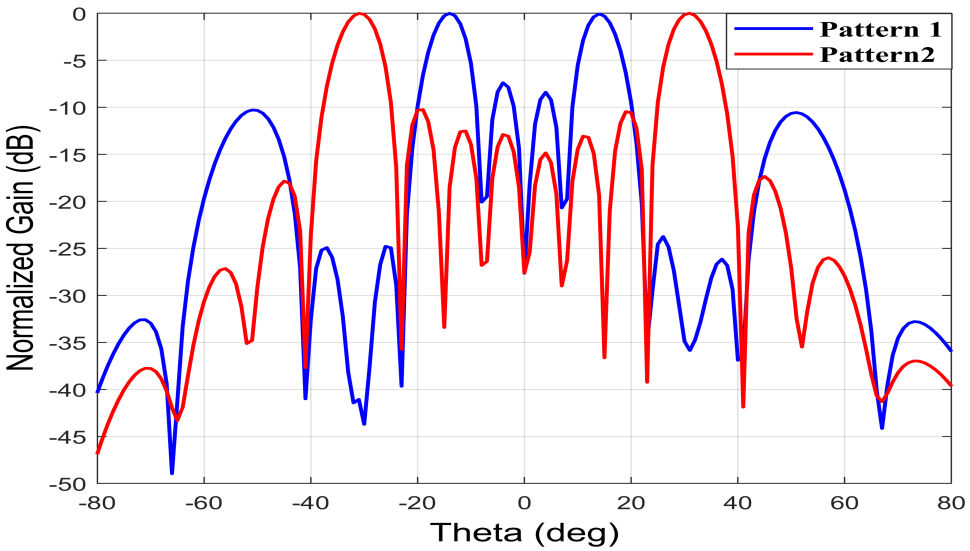


Figure 4.17: The far-field pattern of the array with two different phase distributions.

4.3 Wideband Dual-Polarized RTA Design

Reconfigurable transmitarrays (RTAs) have emerged as a promising approach for achieving high gain along with pattern reconfigurability. These structures offer beam-scanning capabilities similar to RRAs while eliminating feed-blockage effects, particularly in millimeter-wave frequency bands [70]. As discussed in the literature review, refraction is one of the main desired functionalities of RIS, which can be realized using transmitarrays. There are two main approaches to transmitarray design. The first approach utilizes multi-layer frequency-selective surfaces (FSS) to achieve the required phase for beam steering by adjusting the length or shape of each layer. The second approach employs a receiver–transmitter (Rx–Tx) structure with a transmission mechanism between them. In this method, the phase shift can be introduced in each component, typically by using tunable elements. The second approach generally offers superior performance for wideband

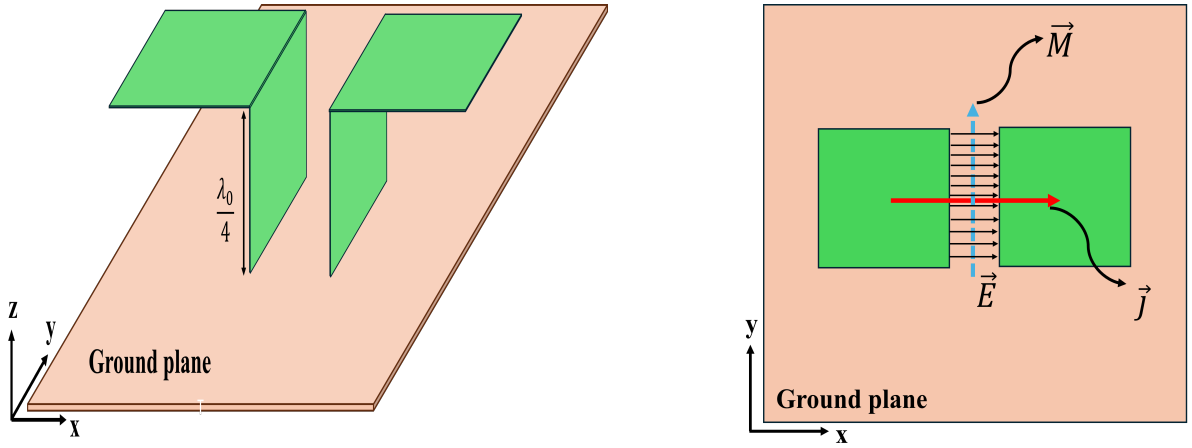
array design [71].

Several studies on reconfigurable transmitarray design have been reported in the literature [72], [73]. In [74], an RTA was proposed using a combination of two magneto-electric (ME) dipole antennas as the receiving and transmitting components. This design exhibited a wide gain bandwidth due to the use of ME dipoles. Considering polarization diversity, few works have addressed dual-polarized RTA designs because of various challenges. The unit cell introduced in [75] utilized two square ring patches for receiving and transmitting. These patches are excited by two orthogonal U-shaped transmission lines loaded with PIN diodes, enabling independent dual linear polarization and 1-bit phase tuning. The design presented in [76] offers a 1-bit dual-polarized element; however, the two polarization modes cannot operate simultaneously. In [77], a novel 1-bit dual-polarized RTA was proposed, employing asymmetric dipoles for both polarizations, and the design was verified through fabrication and measurements.

The aim of this section is to propose a unit cell structure that provides dual-polarization control with wideband operation. The design incorporates a magneto-electric (ME) dipole antenna as the transmitting element, fed by a square patch acting as the receiving element. Two distinct phase states are achieved using PIN diode switches. To validate the design concept, a transmitarray employing the proposed structure was simulated, and its beam-steering capability was evaluated.

4.3.1 Unit cell design

To address the design requirements of wide bandwidth and dual-polarization operation, magneto-electric (ME) dipoles are utilized in the proposed structure. A magneto-electric dipole antenna provides wide bandwidth by incorporating both electric and magnetic



(a) (b)

Figure 4.18: (a) 3D view of the ME-dipole structure. (b) Electric and magnetic currents resulting from the excited electric field on the aperture.

dipoles with simultaneous excitation in a single configuration. Figure 4.18 (a) shows an implementation of an ME-dipole structure proposed in [78], which consists of two strips short-circuited to the ground by a vertical metal strip with a quarter-wavelength height. By exciting the electric field in the aperture, both electric and magnetic currents are generated as shown in Figure 4.18 (b), resulting in wideband operation. To handle both polarizations, the structure is modified as demonstrated in Figure 4.19. By exciting the appropriate electric field in the corresponding apertures, the structure can radiate both polarizations. This configuration is used in the proposed structure to achieve the design goals.

The proposed structure, illustrated in Figure 4.20, consists of receiving and transmitting components. The transmitting part is a dual-polarized ME dipole, which comprises four square metallic patches connected to the ground layer through four sets of vias. It also

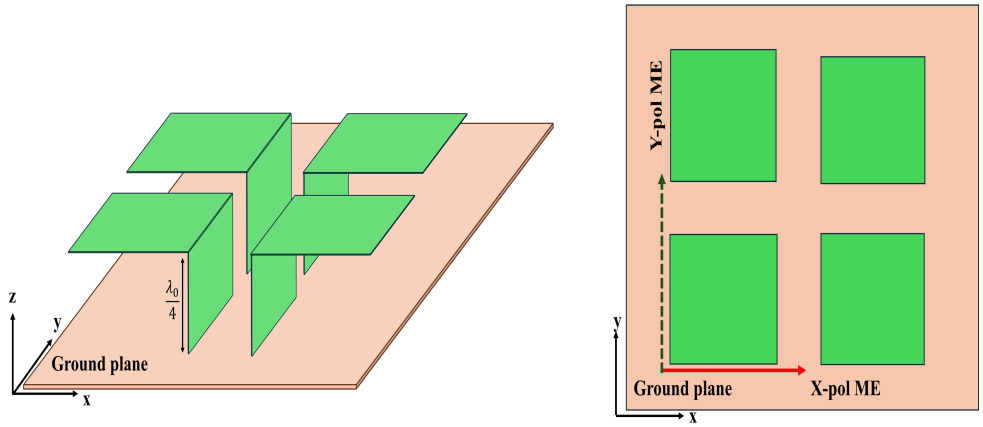
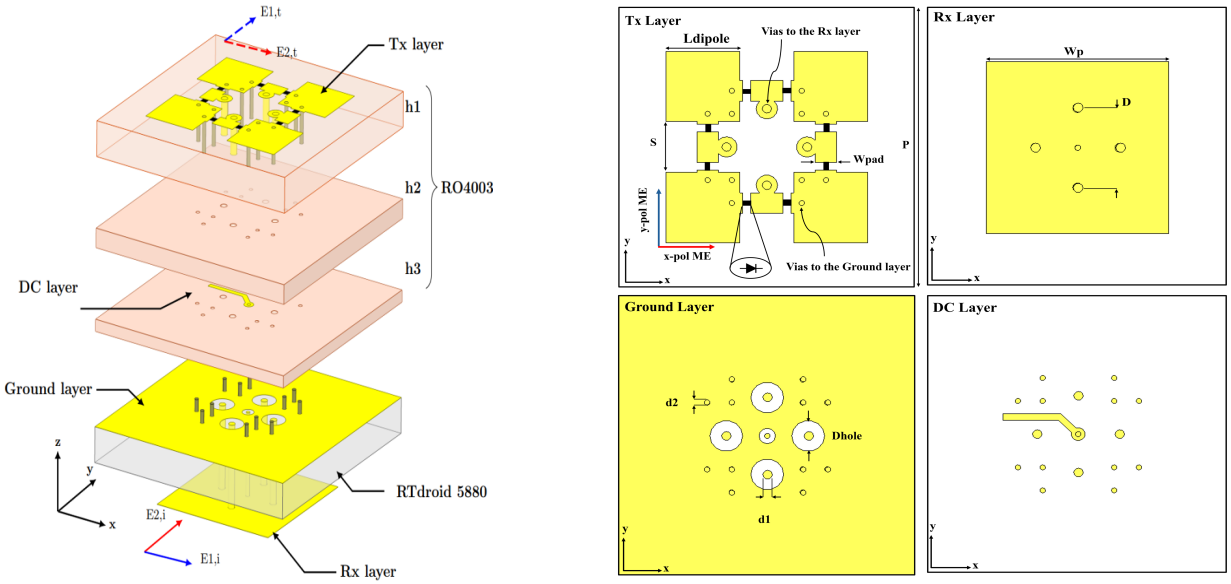


Figure 4.19: Dual polarized ME-dipole antenna.

includes three substrate layers: Rogers RO4003 with thicknesses $h_1 = 1.57$ mm, $h_2 = 0.82$ mm, and $h_3 = 0.508$ mm, respectively. These heights are chosen to approximate a total height of one-quarter wavelength($\lambda_g/4$), enabling the implementation of a vertically placed quarter-wave shorted patch at center frequency (13.5 GHz) [79]. The receiving component is a square patch antenna, capable of receiving both polarizations, and placed on a RTDroid 5880 substrate with a thickness of 1.57 mm, designed to operate at 13.5 GHz. The unit cell periodicity P is set to be less than $\lambda_0/2$ at the center frequency. Two pairs of through vias along the x- and y-axes pass through the ground layer, connecting the square patch to the ME-dipole antenna. These vias establish a conductive path between the receiving and transmitting components for both polarizations, with the ON/OFF states of the PIN diodes controlling the connection. The optimized design parameters are shown in Table 4.4.

To control the PIN diodes, a DC bias line is connected to the center of the square patch through a blind via. Since the electric field at the center of the patch is zero for both polarizations, connecting the DC bias line does not affect the patch's electromagnetic



(a) (b)

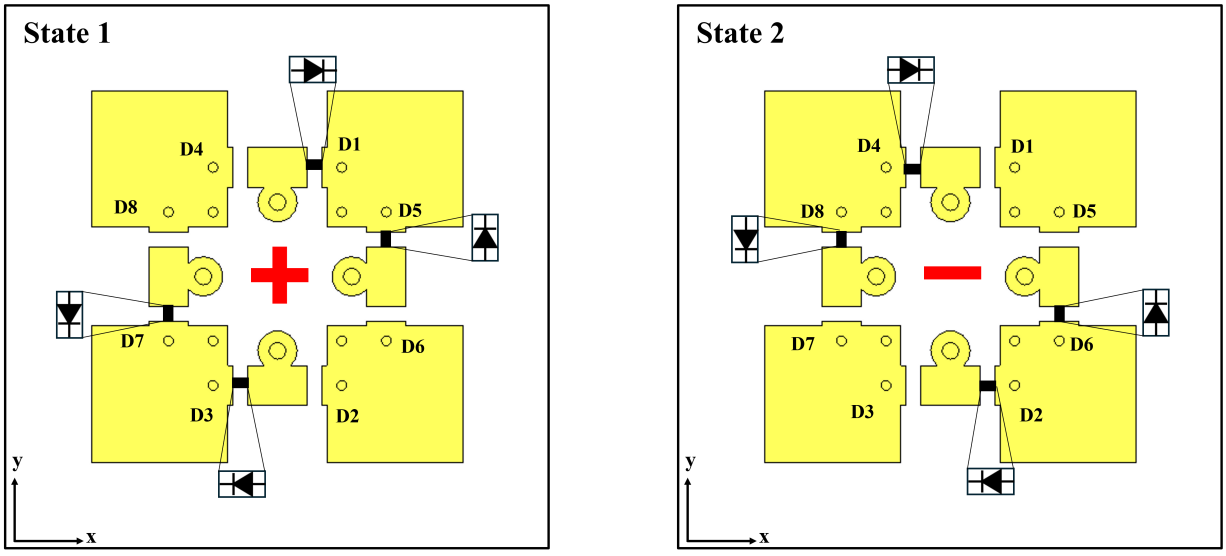
Figure 4.20: The proposed TR unit cell. (a) 3-D view. (b) Layer description.

TABLE 4.4 DIMENSIONS OF THE PROPOSED UNIT CELL.

Parameter	P	Ldipole	S	Wpad	Wp	D	Dhole	d1	d2
Value (mm)	11	5.5	2	0.8	6.5	3	1.2	0.4	0.2

performance. The DC voltage is applied to the PIN diodes through the vias, as they are connected to the square patch. The other terminals of the PIN diodes are located on the metallic patches of the ME dipoles. Consequently, the DC return path to the ground is provided by the grounded vias. This configuration significantly simplifies the biasing circuit, addressing one of the major challenges in transmitarray structures. Moreover, all PIN diodes are controlled using a single DC bias line, which greatly reduces the complexity

of the control system.

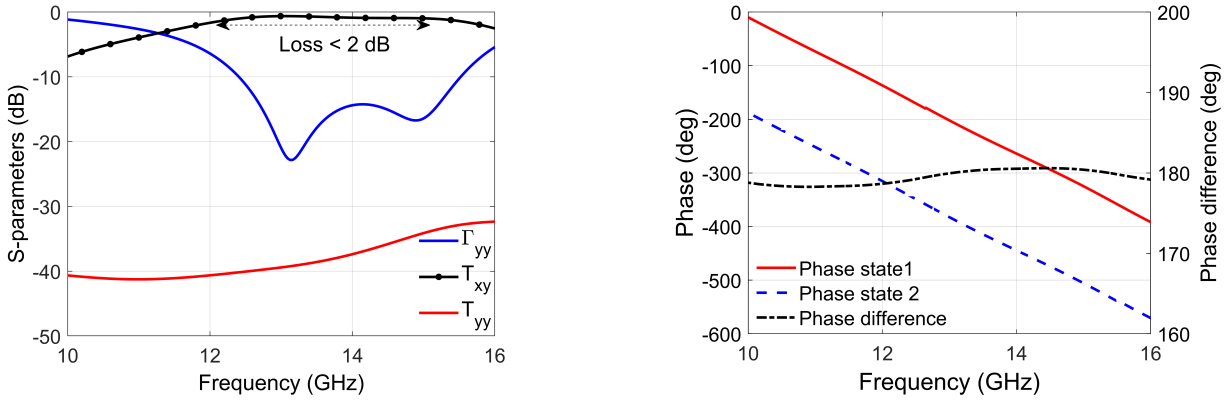


(a) (b)

Figure 4.21: Active PIN diodes for both polarizations in (a) State 1 with positive DC bias, and (b) State 2 with negative DC bias.

When the patch is excited by a y-polarized incident wave, the pair of through vias along the y-axis is activated. Because the electric field in the dominant mode of the patch is zero at the center and out of phase on either side, each pair of vias is excited with a 180° phase difference. As a result, they function as a balun feed to excite the ME dipole antenna. For each polarization, four PIN diodes are used. In State 1, D1 and D3 are activated by applying a positive DC bias, connecting the through vias along the y-axis to the x-polarized ME dipole, as illustrated in Figure 4.21. Consequently, the y-polarized incident wave is transmitted as x-polarization. When a negative DC bias is applied, D2 and D4 are activated, and the transmitted wave experiences a 180° phase shift relative to State 1 due to current reversal. The same mechanism applies for an x-polarized incident

wave, with D5 and D7 activated in State 1, and D6 and D8 activated in State 2. The proposed unit cell was simulated using CST software under periodic boundary conditions (PBC) and excited by both y- and x-polarized incident waves. The equivalent circuit model of the MACOM MADP-00097-1402 PIN diode was incorporated into the simulation.



(a) (b)

Figure 4.22: Simulation results of the proposed unit cell under y-polarized incident wave. (a) Transmission magnitude. (b) Transmission phase.

The simulation results of the unit cell performance are presented in Figure 4.22 for a y-polarized incident wave. In Figure 4.22 (a), T_{xy} and T_{yy} represent the transformation of the y-polarized incident wave into x-polarized and y-polarized transmitted waves, respectively. Accordingly, Γ_{yy} shows the reflection due to the y-polarized incident wave. The results indicate that the y-polarized incident wave is converted into an x-polarized transmitted wave with a loss of less than 2 dB over the entire 11.8 GHz to 15.8 GHz frequency range, demonstrating a bandwidth of more than 25%. The achieved wide bandwidth is a key feature of the ME dipoles used in the structure. The phase difference between the two states, shown in Figure 4.22 (b), demonstrates $180° \pm 2°$ across the entire frequency range,

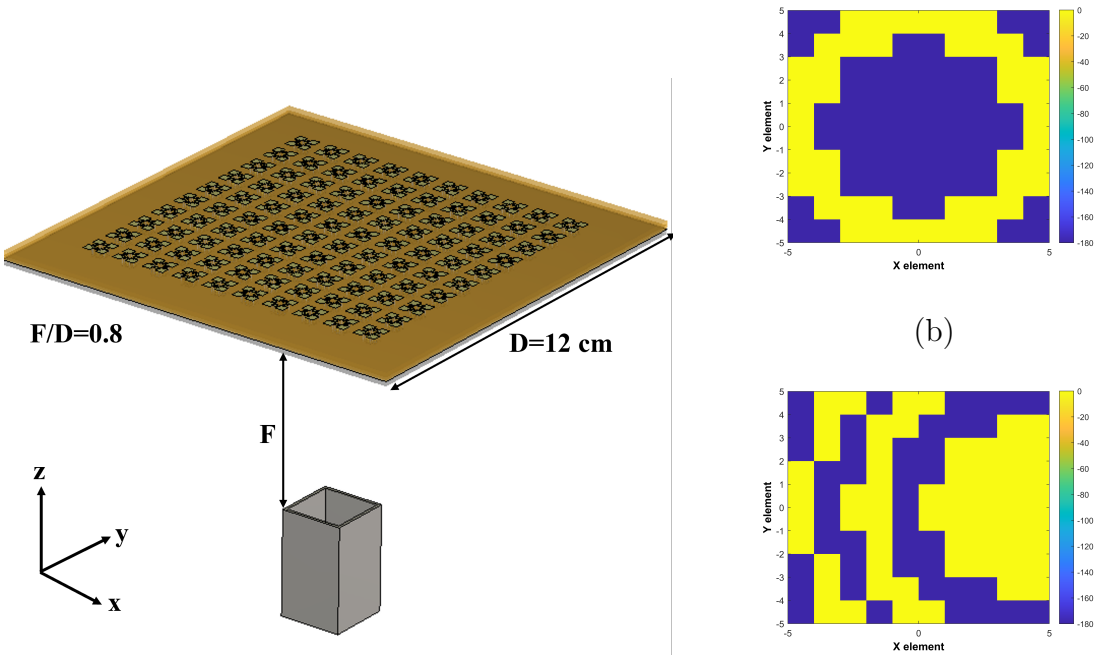
indicating a stable and accurate phase difference over a wide frequency range. For an x-polarized incident wave, same results are expected.

4.3.2 Array simulation

To evaluate the performance of the proposed unit cell, a 10×10 transmitarray was simulated using CST software. Figure 4.23 illustrates the array structure incorporating the unit cell, along with the required phase distributions to steer the beam to $\theta = 0°$ and $\theta = 30°$ in the XoZ plane. The phase distributions were calculated at 14 GHz following the design procedure described in [71].

The simulated radiation patterns for both x- and y-polarizations are presented in Figure 4.24 (a)–(d). The results indicate peak gains of 17.2 dBi at $\theta = 0°$ and 16 dBi at $\theta = 30°$, with a 1-dB gain bandwidth covering 12.5 GHz to 15.5 GHz (20% relative bandwidth). The cross-polarization level is below −20 dB for both scan angles and both polarizations, confirming good polarization purity and satisfactory overall performance.

As discussed earlier, the proposed structure offers a significantly simplified biasing mechanism compared to previously reported designs. A single bias via controls all PIN diodes on the top layer, enabling dual-polarization operation through only one control line. In addition, the structure provides a wide 1-dB gain bandwidth. Although the simulation results demonstrate good performance, a complete comparison with recently published works should be conducted after fabrication and measurement under real-world conditions.



(a) (b) (c)

Figure 4.23: (a) The array structure in CST. (b) Required phase for $\theta_0 = 0°$. (c) Required phase for $\theta_0 = 30°$.

4.4 Conclusion

In this chapter, two wideband, dual-polarized reconfigurable antenna array designs were developed and validated: a reconfigurable reflectarray (RRA) and a reconfigurable transmitarray (RTA). The proposed RRA unit cell exploits the out-of-phase characteristic of the patch's dominant mode to realize two distinct phase states, maintaining a stable $180° \pm 2°$ phase difference over the 10 GHz to 15 GHz band using only two PIN diodes, with one active per state for both polarizations. This configuration enables simultaneous dual-polarization control through a single bias line, significantly simplifying the biasing network. A fab-

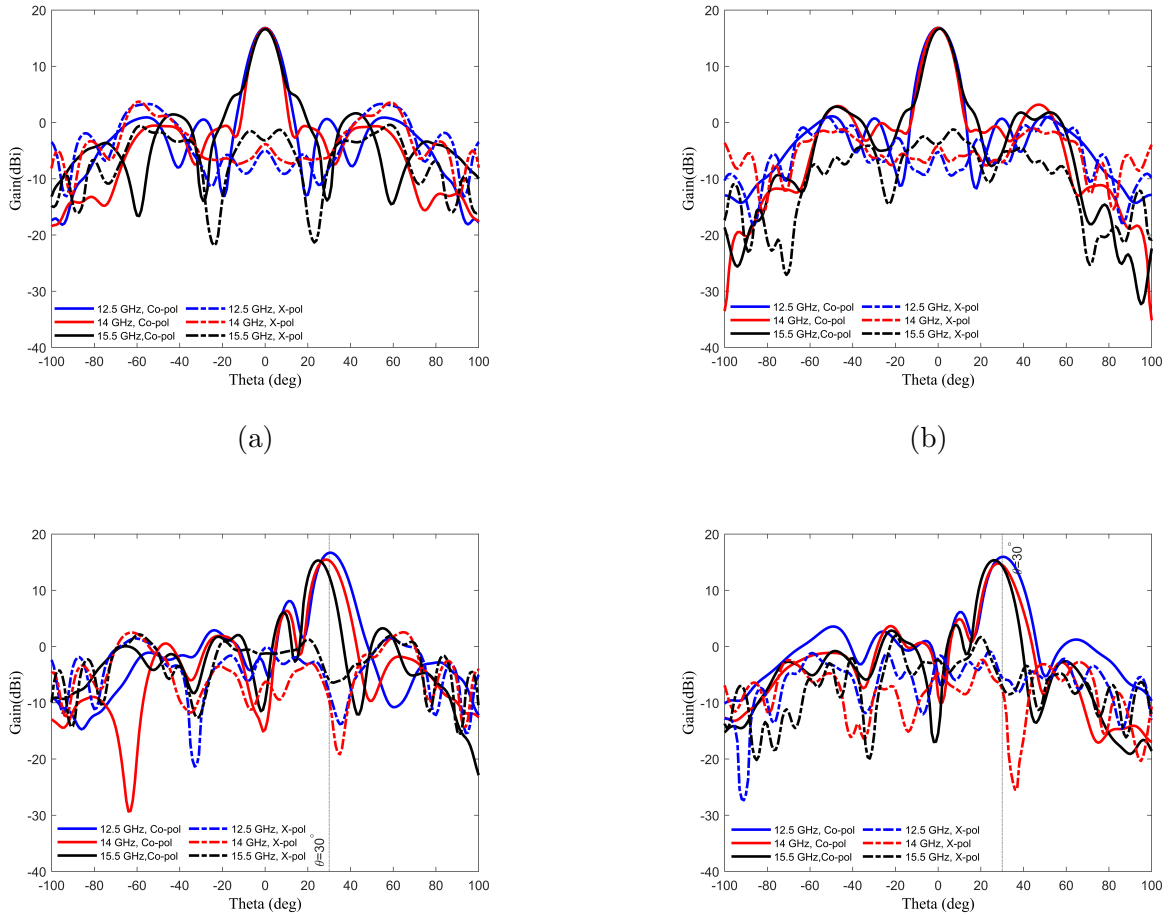


Figure 4.24: Simulated gain of the array. (a) $\theta = 0°$, x-polarization. (b) $\theta = 0°$, y-polarization. (c) $\theta = 30°$, x-polarization. (d) $\theta = 30°$, y-polarization.

ricated 10×10 prototype demonstrated beam steering with measured radiation patterns closely aligned with simulations, achieving a 13.7% 1-dB gain bandwidth while supporting both linear and circular polarization.

The proposed RTA unit cell integrates a magneto-electric dipole and a square patch

to form the receiving and transmitting elements, achieving a transmission loss below 2 dB from 11.8 GHz to 15.8 GHz. When employed in a transmitarray, the design provided a 1-dB gain bandwidth from 12.5 GHz to 15.5 GHz (20% relative bandwidth). Similar to the RRA, both polarizations are controlled through a single bias signal, simplifying practical implementation. Together, these designs deliver efficient, wideband, reconfigurable, and polarization-diverse array solutions with reduced complexity, making them strong candidates for modern high-performance beam-steering applications.

Chapter 5

Reconfigurable Arrays Using MEMS Actuator

5.1 Introduction

Micro-Electro-Mechanical Systems (MEMS) actuators have emerged as a promising technology for realizing reconfigurable unit cells in reflective surfaces and reflectarrays. Unlike traditional approaches relying on PIN diodes, varactors, or liquid crystals, MEMS-based tuning mechanisms offer several unique advantages, including low insertion loss, excellent linearity, high power handling capability, and minimal parasitic effects at microwave and millimeter-wave frequencies. MEMS actuators enable precise mechanical adjustments—such as modifying the physical position, orientation, or gap spacing of metallic elements within a unit cell—which in turn dynamically alters the phase response or polarization characteristics of the reflected wavefront. This capability facilitates the development of agile beam-steering and polarization-reconfigurable surfaces with enhanced performance

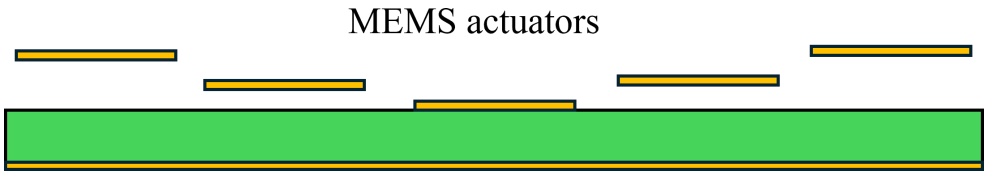
and reliability. Furthermore, MEMS technology supports monolithic integration with planar fabrication processes, allowing the realization of compact, low-profile reconfigurable reflectarrays suitable for emerging applications in satellite communications, radar systems, and 5G/6G networks. As a result, MEMS actuators are increasingly being investigated as a versatile and scalable solution for the next generation of intelligent electromagnetic surfaces.

5.2 Unit Cell Design Using MEMS Actuators

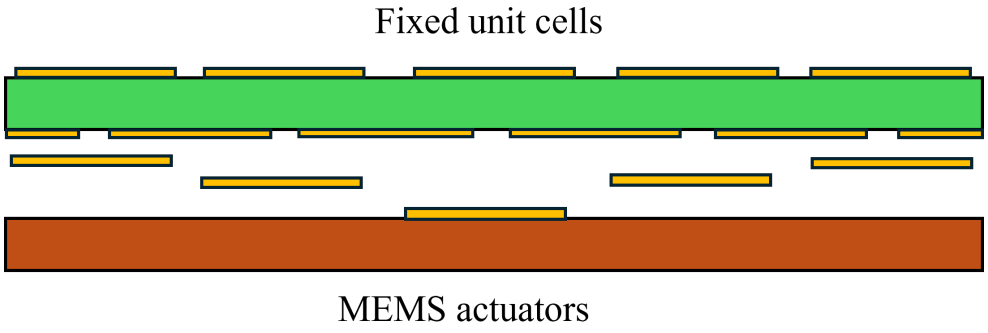
MEMS switches have been employed in reconfigurable array design due to their potential applications in higher frequency bands. Despite issues related to reliability and switching speed, they have special characteristics like low power consumption, high linearity, and monolithic integration, making them an attractive option [80]. Similar to PIN diodes, MEMS switches are used in applications where discrete reflection phases are needed. A 1-bit dual-polarized unit cell using ohmic MEMS switches was proposed in [44], demonstrating low loss at X-frequency band. The authors in [81] employed MEMS switches to design a beam switching array at Ka-frequency band. Most of the works presented in the literature focus on using MEMS switches.

While designing unit cells for discrete reflection phases simplifies the bias and control systems, there are still intriguing applications for dynamic reflection phase control [48]. It renders the use of MEMS actuators an interesting option to achieve dynamic reflection phases, alongside other solutions such as varactor diodes and liquid crystal. In addition, MEMS actuators can be employed to obtain discrete phase states by using them in different actuation states. In the literature, different movable structures were used utilizing piezoelectric actuators [82], magnetic tuning [83], and micro motors [84]. Compared to these

methods, using MEMS actuators becomes even more interesting for high frequency applications, where future generation of communication systems are intended to operate [85], [86].



(a)



(b)

Figure 5.1: Typical topologies using MEMS actuators. (a) MEMS actuators utilized as unit cells. (b) Fixed unit cells integrated with MEMS actuators.

Generally, MEMS actuators are proposed in two main topologies, demonstrated in Figure 5.1. In the first topology, the movable actuator itself constitutes the unit cell, altering the reflection phase by moving up and down. In the second topology, the unit cells are fixed in one layer, and a MEMS actuator layer is integrated with the unit cell layer to provide reconfigurable reflection phase. Considering the first topology, the authors in [87] proposed a patch unit cell with variable height to achieve reconfigurability. However, neither experimental results nor details about the MEMS actuator were provided. From

fabrication point of view, the first topology may face different challenges since all the fabrication process should be done on the same layer. A high impedance surface (HIS) was proposed at W-band, using a movable membrane in [88], which encountered various fabrication and measurement challenges. The second topology, which is considered for the proposed unit cell here, seems to be less challenging due to the fact that actuator layer has separate fabrication from the unit cell layer.

5.3 The Proposed Unit Cell Structure

5.3.1 Design and simulation

The proposed structure consists of two main parts: electric-LC resonator (ELC) and MEMS actuator. As depicted in the Figure 5.2 (a), ELC resonator is a capacitor-like structure which is connected to two inductive loops. The ELC resonator is known as electric counterpart of split ring-resonator, which couples to an incident electric field [89]. A notable advantage of the ELC resonator, which makes it a suitable choice in reflectarray design, is its ability to maintain invariant reflection phase characteristics over a wide range of incident angles [90]. Consequently, they have been utilized in different reflect array designs [91], [92]. Considering the lumped element model in Figure 5.2 (b), the resonance frequency can be expressed as:

$$f_0 = \frac{1}{2\pi}\sqrt{\frac{2}{LC}} \tag{5.1}$$

where f_0 is the resonant frequency, L is the equivalent inductance, and C is the equivalent capacitance.

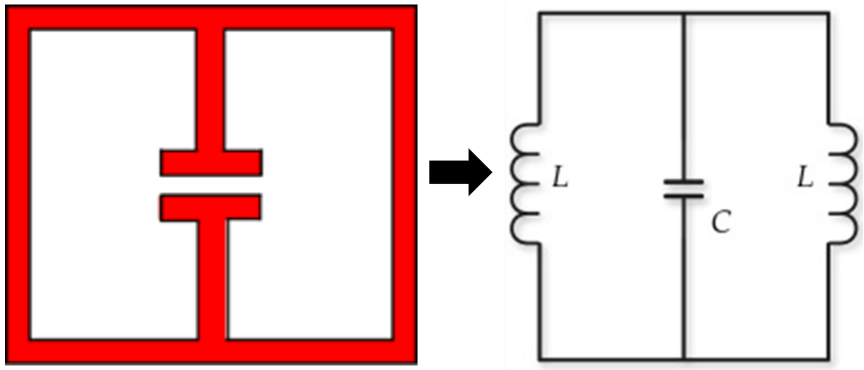


Figure 5.2: Schematic of an ELC resonator with lumped element model.

To change the resonance frequency and, consequently, the reflection phase, either the inductance or the capacitance can be adjusted. To achieve capacitance variation, a MEMS actuator is employed. Figure 5.3 illustrates the proposed structure. A commercial substrate, RO4003, with a permittivity of 3.55 and a thickness of 20 mil (0.508 mm), is used. To model the actuator's movement, an ideal metal plane mounted on a silicon substrate, capable of vertical motion, is used. Two vias connect the middle strip on the top layer to two pads on the bottom layer, which are isolated from the ground plane by a slot. These pads form a variable capacitance with the actuator plane. An alumina substrate containing the DC bias lines is included to account for their effects in the simulation. These DC bias lines are connected to the actuator's DC pads via wire bonds. Both substrates are integrated with the resonator by a support section, which can be made of either metallic or non-metallic material, as it does not affect the results. In this design, a plastic material is used for the support section. When the actuator plate moves toward the via pads, the capacitance between them changes, causing a corresponding change in the reflection phase. Table 5.1 presents the design parameters of the proposed structure.

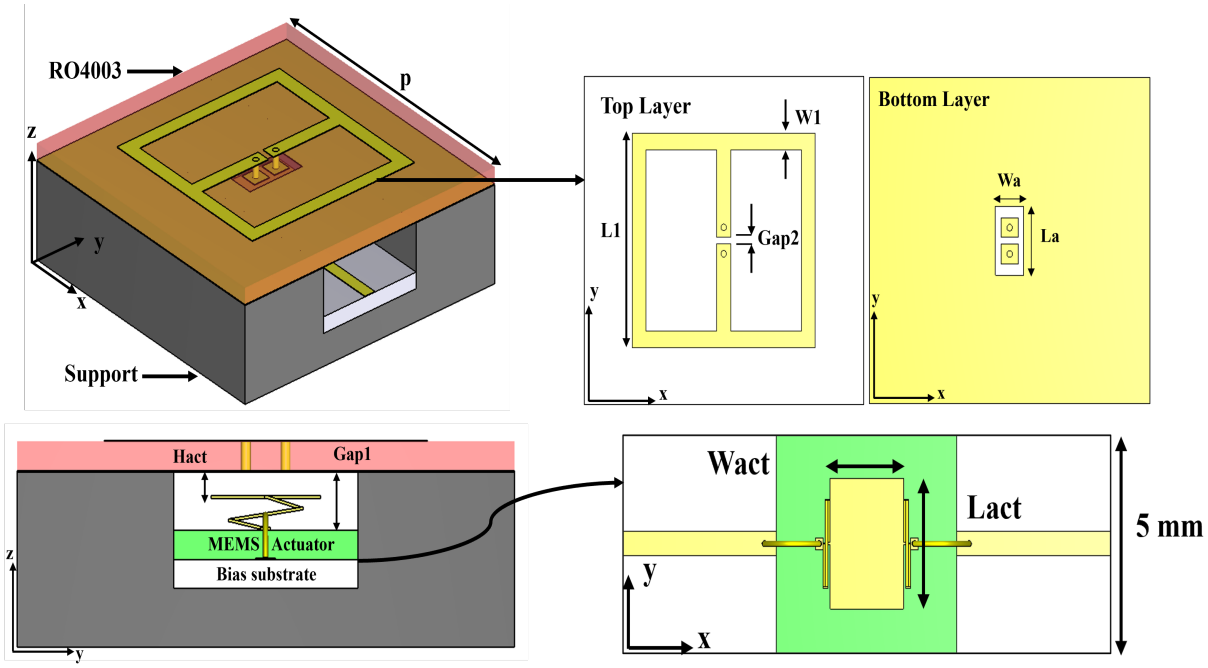


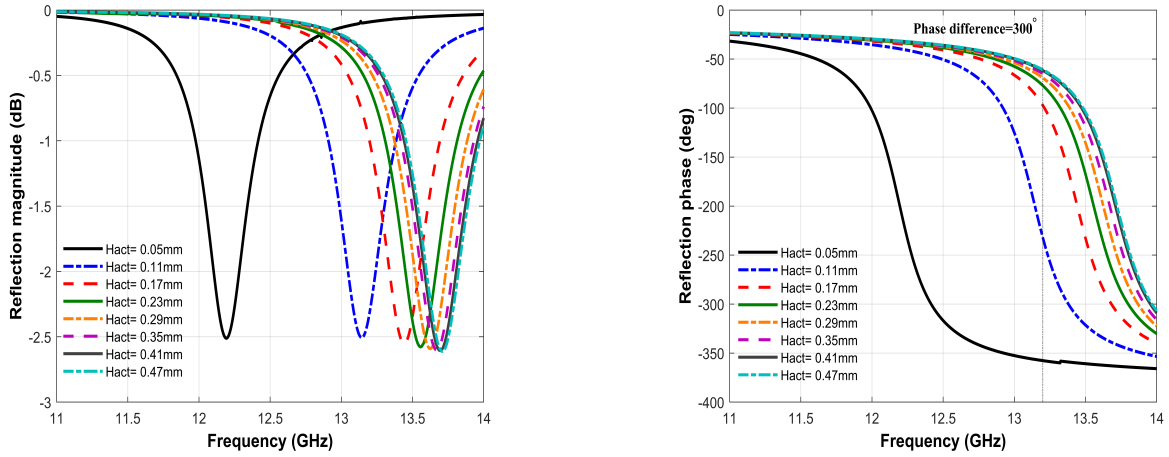
Figure 5.3: The proposed unit cell structure using MEMS actuator.

Table 5.1 Dimensions of the proposed unit cell.

Parameter	P	L1	W1	Gap1	Gap2	Lact	Wact	Hact
Value (mm)	10	5.5	0.5	1	0.2	2.2	1.8	0.05 - 0.5

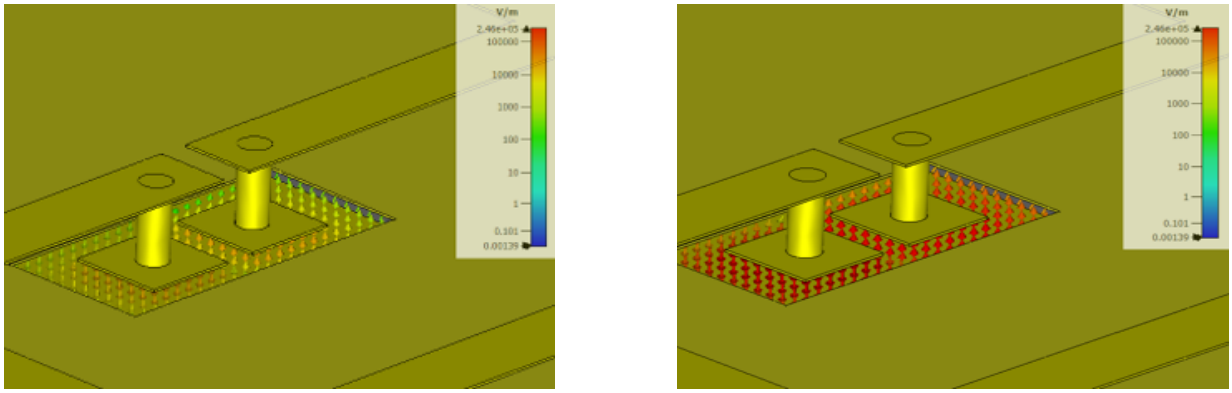
The proposed unit cell was simulated using CST software and excited by a y-polarized incident plane wave under periodic boundary condition (PBC). The actuator is capable of moving upward to the maximum height defined by Gap1, which is set to 1 mm. It is anticipated that the maximum change in resonance will occur when the actuator is in close proximity to the bottom layer. Therefore, the actuator's movement is restricted within the range of 0.45 mm to 0.95 mm. Figure 5.4 illustrates the reflection phase and magnitude

for various actuator movements. It demonstrates that as the actuator moves towards the bottom layer, the resonance frequency will change, leading to a change in reflection phase. At 13.2 GHz, the reflection phase changes about 300^0 and reflection magnitude shows maximum loss around 2.5 dB for entire frequency band. As anticipated, the most significant resonance change occurs when the actuator is in close vicinity of the bottom layer. To observe the effect of actuator, electric fields at two frequencies are demonstrated in Figure 5.5, with actuator height set to 0.1 mm. It shows a strong electric field between via pads and the actuator at 13 GHz, which is the resonance frequency at this height.



(a) (b)

Figure 5.4: Simulated reflection magnitude and phase of the proposed structure. (a) Reflection magnitude. (b) Reflection phase.



(a) (b)

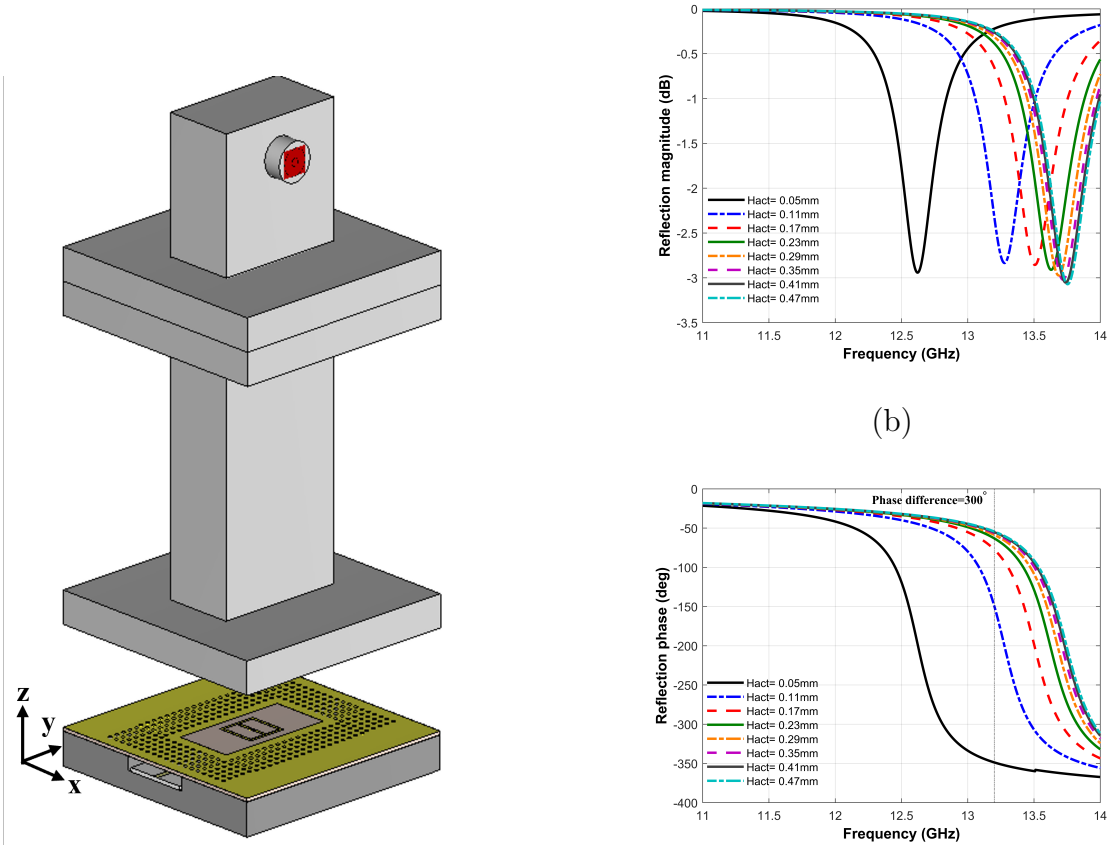
Figure 5.5: . Electric field strength at Hact=0.1mm. (a) 12.6 GHz. (b) 13 GHz.

The periodic boundary condition (PBC) used to obtain the reflection phase of the unit cell assumes an infinite array of unit cells with a plane wave excitation. In practical applications, using waveguide measurement set up is one of the methods to measure the reflection phase of the unit cell. This approach is an efficient and simple way to evaluate the performance of the unit cell. One or a few unit cells are fitted and excited by the dominant TE_{10} mode of the waveguide, which can be decomposed to two plane waves with incidence angles derived as [29], [93]:

$$\theta_{\text{inc}} = \cos^{-1}\left(\sqrt{1-\left(\frac{f_c}{f}\right)^2}\right) \tag{5.2}$$

Where f_c is the cutoff frequency of the waveguide dominant mode, and f is the operating frequency. Based on Equation 5.2, the incident angle of this plane wave varies with changes in the operating frequency. Consequently, the results of this method may differ slightly from those of the PBC method, as the unit cell's reflection phase is influenced by the change in incident angle. In this case, the incident angle will be $\theta_{\text{inc}} \leq 36°$ for the frequency range

of 11 GHz to 14 GHz. As noted in [94], reflection phase variations are generally minimal for incident angles up to $\theta_{\text{inc}} = 40°$, indicating that waveguide measurement setup is a reliable approach for evaluating unit cell functionality. Additionally, the proposed unit cell demonstrates stability across incident angles in this range, which further improves the accuracy of the evaluation.



(a) (b) (c)

Figure 5.6: (a) Waveguide simulation set up. (b) Reflection magnitude. (c) Reflection phase.

A WR-75 waveguide is used for excitation in this simulation, covering the desired frequency band. Figure 5.6 (a) depicts the proposed unit cell in the waveguide simulation set up. To establish a connection between the ground plane and the waveguide flange, the top layer is covered by a series of vias that are connected to the ground plane. As demonstrated in Figure 5.6 (b)-(c) , although a slight shift in the resonance is introduced, the waveguide simulation shows the same range for the reflection phase at 13.2 GHz.

5.3.2 Fabrication and Measurement

To evaluate the performance of the proposed unit cell, a prototype was fabricated and measured. The ELC resonator part, shown in Figure 5.7 (a)-(b), was fabricated on a RO4003 Rogers substrate. As mentioned above, the top and bottom layers are connected with a series of vias, which enable the connection between ground plane and waveguide flange for measurement. It will not affect the results because it is covered by waveguide flange.

The MEMS actuator was fabricated using PolyMUMPs process, a three-layer micro-machining process [95]. The basic unit of the actuator is a bimorph made of gold and poly silicon, which exhibits deflection after thermal plastic deformation assembly treatment. To achieve required out-of-plane displacement, several bimorph units are connected in a zig-zag manner, as discussed with details in [96]. Figure 5.7 (c)-(d) shows the fabricated actuator with its scanning electron microscopy (SEM) picture. These structures usually consume more power compared to other structures like electrostatic actuators, but they offer larger displacement.

To provide DC bias for the actuator, it was assembled on an alumina substrate containing DC bias lines, as demonstrated in Figure 5.8 (a). The actuator DC pads are connected

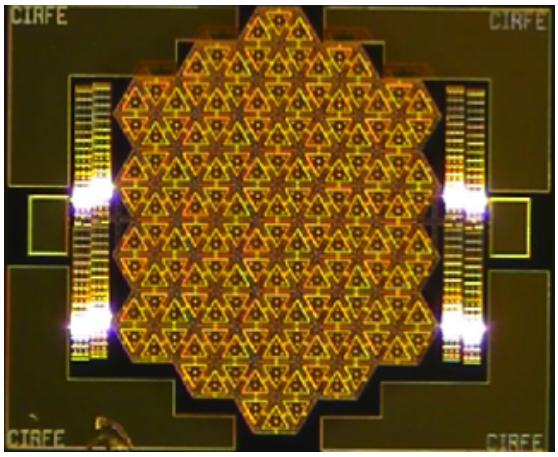
to the bias lines via wire bonds. The assembled actuator and the ELC resonator are attached to the waveguide set up shown in Figure 5.8 (b) with a support section, made with plastic material using 3D-printing.



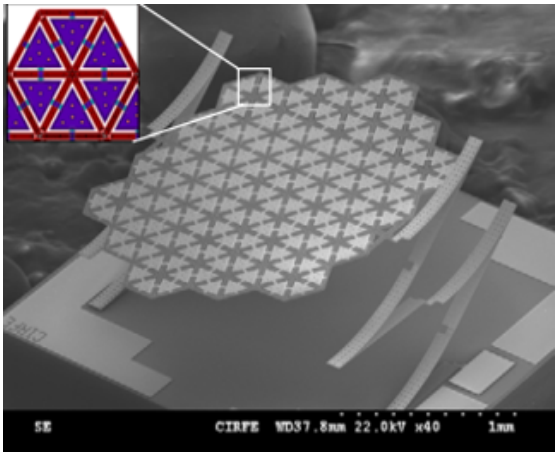
(a)



(b)

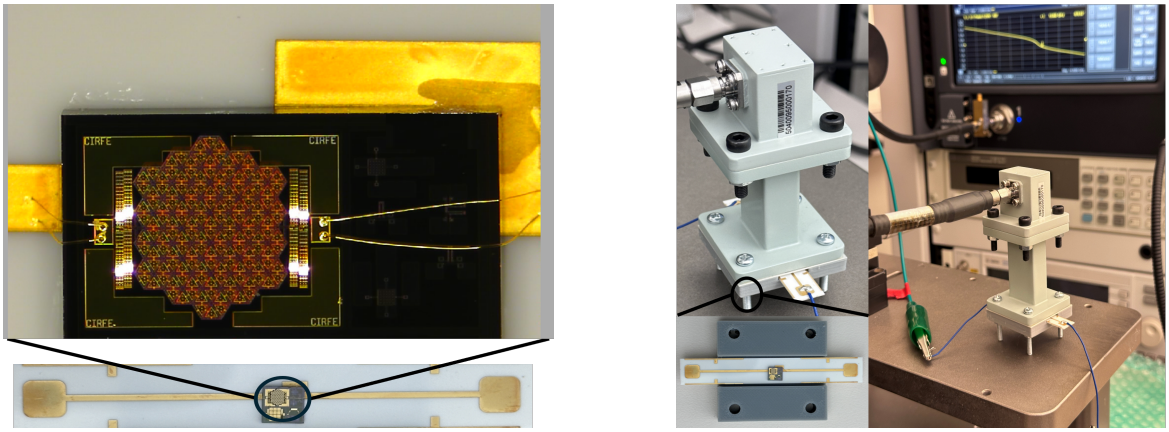


(c)



(d)

Figure 5.7: (a) Top layer of the ELC resonator. (b) Bottom layer of the ELC resonator. (c) Fabricated MEMS actuator. (d) SEM picture of the MEMS actuator.

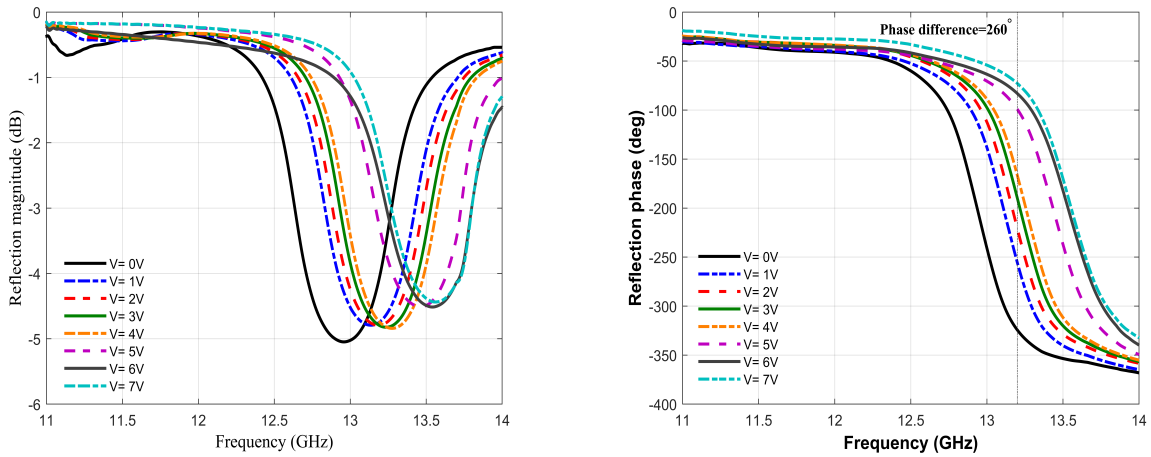


(a) (b)

Figure 5.8: (a) Fabricated MEMS actuator on the alumina substrate. (b) Waveguide measurement set up.

The measured reflection magnitude and phase are shown in Figure 5.9, indicating approximately 260° change in reflection phase at 13.2 GHz as the applied voltage changes from 0 V to 7 V. The maximum incurred loss is about 5 dB at this frequency. The major source of loss is related to the unit-cell structure. The aperture etched in the ground plane to achieve variable capacitance increases the reflection loss, as a portion of the wave leaks through the aperture. In addition, part of the loss may be attributed to the connection between the waveguide flange and the resonator top layer. Using a metal support can help to tighten this connection and subsequently reduce the loss. As observed in the measurement results, the reflection phase exhibits a significant change when the actuator is in close proximity to the bottom layer of the resonator. This is a positive aspect, as it can reduce the actuator design complexity by decreasing the required displacement. A comparison between several reported works and the proposed structure is provided in Table 5.2, showing an acceptable phase range for the proposed design. Compared to [87], which presents

a similar application, the proposed structure demonstrates improved performance verified by measurement.



(a) (b)

Figure 5.9: Measured (a) reflection magnitude and (b) reflection phase of the proposed structure.

5.4 Array Simulation

To explore the functionality of the proposed unit cell, an 11×11 reflectarray was simulated using CST software. Figure 5.10 shows a general view of the array, which consists of the unit cells, the MEMS actuator layer, and the support section. Each actuator is connected to the DC bias lines via wire bonds. These bias lines can be fed by DC feed-through passing through holes in the support. A WR-75 waveguide with a y-polarized incident wave is used for excitation.

Table 5.2 Performance comparison with related works

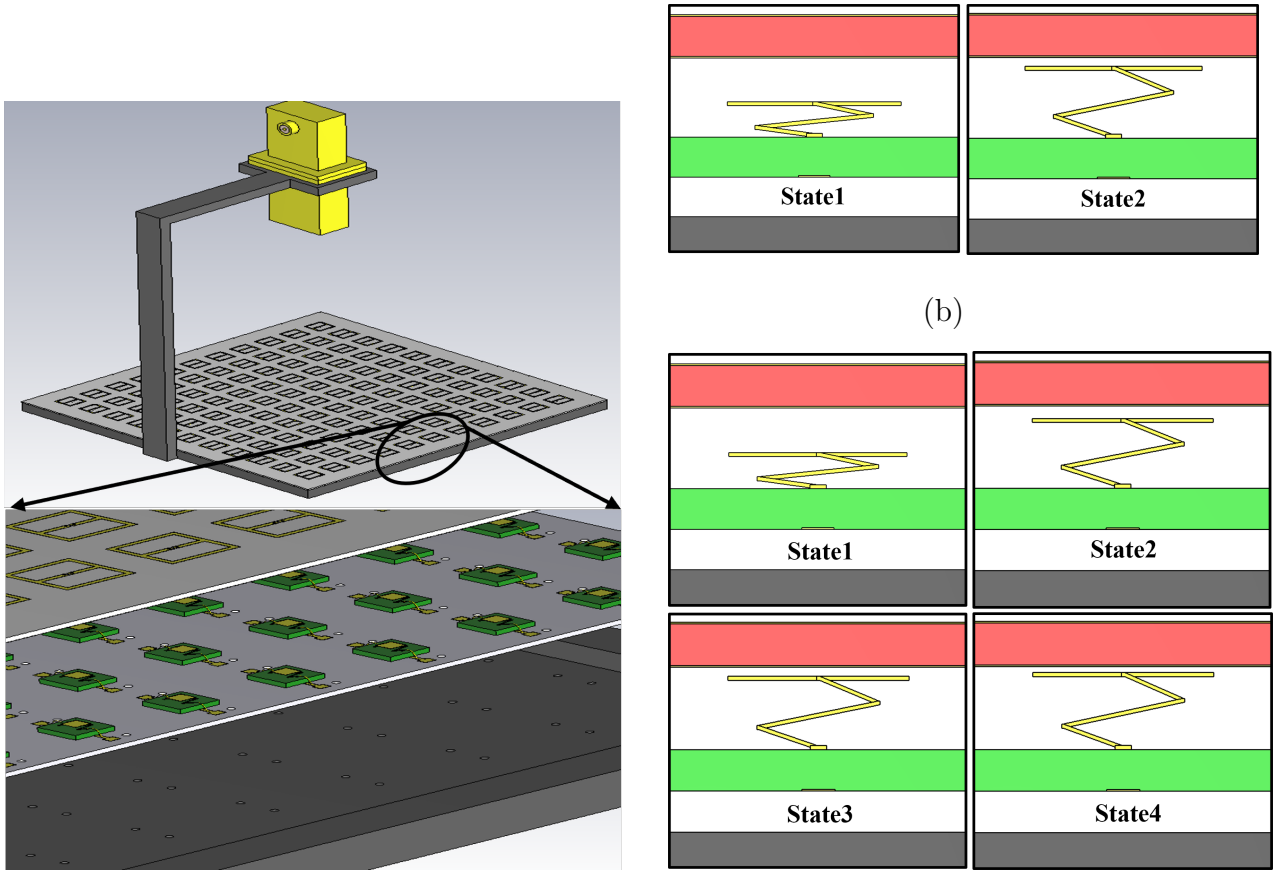
Ref.	Freq. (GHz)	Technology	Control Method	Phase Range
[84]	4.8	Motor	Manual	324°
[83]	5.8	Magnetic tuning	Analog	190°
[82]	13	Piezoelectric actuator	Analog	178°
[87]	5.2	MEMS actuator	Analog	200°
This Work	13.2	MEMS actuator	Analog	260°

To evaluate the array performance more precisely, 1-bit and 2-bit phase quantization are applied alongside the analog phase distribution to investigate their effects on the radiation characteristics. Different schemes can be employed for phase quantization. In the following design, the schemes shown below are used for 1-bit and 2-bit phase quantization, respectively.

$$\varphi_{\text{1-bit}} = \begin{cases} 0, & -180^\circ < \phi_R \leq 0^\circ \\ -180^\circ, & -360^\circ < \phi_R \leq -180^\circ \end{cases} \tag{5.3}$$

$$\varphi_{\text{2-bit}} = \begin{cases} 0, & -90^\circ < \phi_R \leq 0^\circ \\ -90^\circ, & -180^\circ < \phi_R \leq -90^\circ \\ -180^\circ, & -270^\circ < \phi_R \leq -180^\circ \\ -270^\circ, & -360^\circ < \phi_R \leq -270^\circ \end{cases} \tag{5.4}$$

where ϕ_R is the continuous reflection phase expressed in Equation 3.4.



(a) (b) (c)

Figure 5.10: (a) Array structure usign the proposed unit cell. Discrete movement of actuators for (b) 1-bit phase distribution and (c) 2- bit phase distribution.

To implement the required analog phase distribution, the actuators move continuously within the 0.45 mm–0.95 mm range to provide the required reflection phase for each unit cell. For the 1-bit and 2-bit phase distributions, the actuators move in discrete steps, as depicted in Figure 5.10(b)–(c). The array is designed at a center frequency of 13.2 GHz to radiate at two different angles: $\theta_0 = 0^\circ$ and $\theta_0 = 30^\circ$ in the x–z plane. For each angle,

three different phase distributions are used. The required phase distributions and the corresponding radiation patterns for each design are shown in Figure 5.11 and Figure 5.12, respectively.

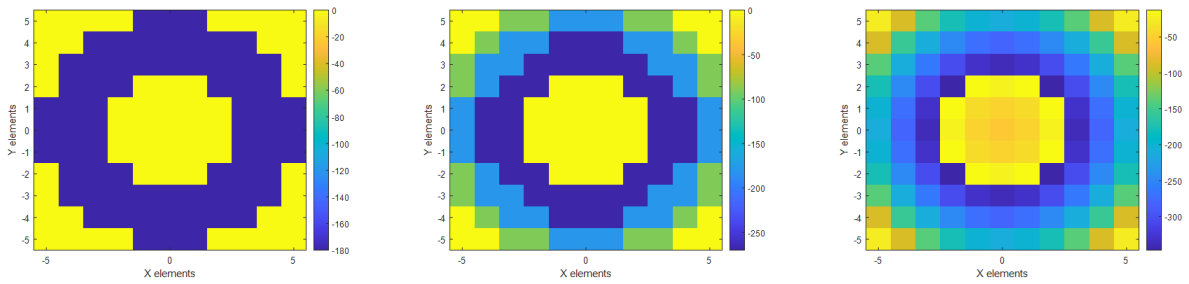
Simulation results show that the radiation pattern is directed to the specified angle in all cases. The gain in the beam direction is 17.8 dBi, 16.5 dBi, and 14.3 dBi for the analog, 1-bit, and 2-bit phase distributions, respectively. As expected, phase quantization reduces the gain and increases the side-lobe level (SLL). At both angles, the 1-bit and 2-bit phase distributions exhibit degradation in both gain and SLL. Beam steering itself also degrades the radiation characteristics, which can be observed by comparing the radiation patterns at the two angles for each phase distribution individually.

5.5 Discussion and Conclusion

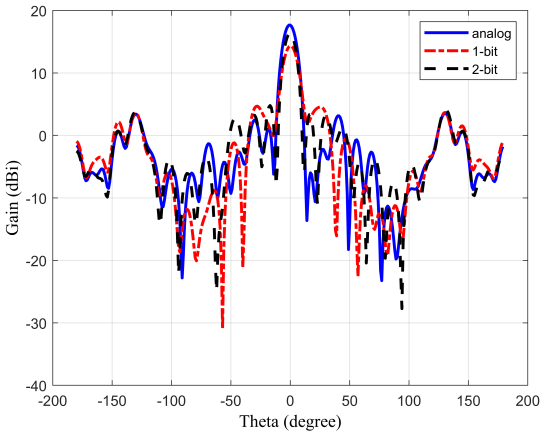
The proposed unit cell presented in this chapter effectively demonstrates the potential of using MEMS actuators in reconfigurable reflective antenna design. Alongside other tuning techniques, MEMS actuators can be employed to achieve dynamic reflection phase control, which is required in various applications. At higher frequency bands in particular, they can address limitations associated with semiconductor-based tuning elements.

Using the actuator in a distinct layer, rather than integrating it directly within the unit-cell layer or employing it as a movable unit cell, simplifies the fabrication process and reduces potential issues related to single-layer manufacturing. Furthermore, the proposed structure is capacitively coupled to the unit-cell layer without direct contact, which helps mitigate issues related to contact reliability.

From a practical point of view, 1-bit and 2-bit array designs utilizing MEMS actuators

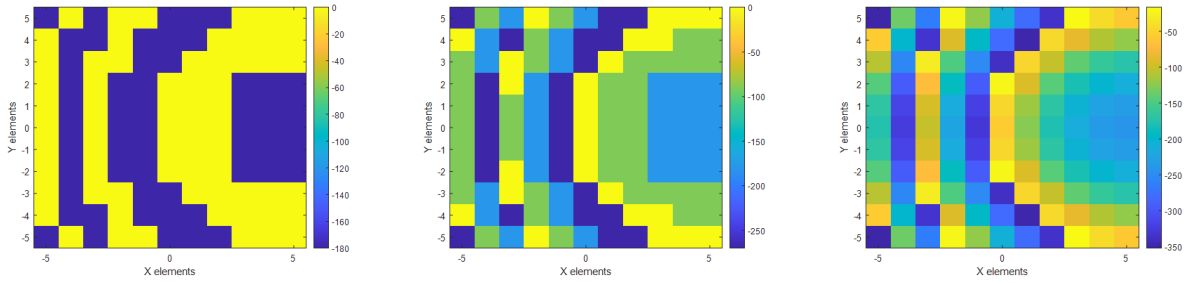


(a) (b) (c)

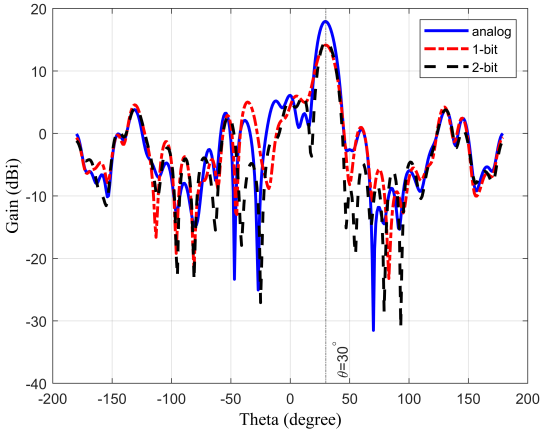


(d)

Figure 5.11: (a) 1-bit phase distribution. (b) 2-bit phase distribution. (c) analog phase distribution. (d) Simulated radiation patterns for $\theta_0 = 0^0$.



(a) (b) (c)



(d)

Figure 5.12: (a) 1-bit phase distribution. (b) 2-bit phase distribution. (c) analog phase distribution. (d) Simulated radiation patterns for $\theta_0 = 30^0$.

are of interest. In a typical 2-bit array design using PIN diodes, numerous issues arise, such as control system complexity, the impact of DC bias on RF characteristics, and implementation challenges. Although MEMS actuator fabrication and reliability still face challenges, the above array design shows that different phase states can be obtained simply by altering DC voltages.

Despite the promising results, several challenges remain. The current consumption

of the actuator is relatively high due to the nature of bimorph structures, which require substantial DC current for actuation. In this design, the actuator consumes 10 mA at a maximum voltage of 7 V. The choice of this actuator was primarily to demonstrate the concept. However, for large arrays, a more efficient actuator structure may be required. Additionally, while the design demonstrates the feasibility of using MEMS actuators, issues related to their fabrication and long-term reliability require further investigation.

Future work can focus on optimizing the actuator design to reduce power consumption and improve efficiency. Investigating the application of this technology at higher frequency bands, such as millimeter-wave and sub-terahertz, where traditional semiconductor-based tuning elements are less effective, is another promising direction. These advancements could pave the way for more versatile and efficient reconfigurable antenna array designs in the next generation of communication systems.

Chapter 6

Conclusion and Future Work

6.1 Conclusion

Reconfigurable Intelligent Surfaces (RISs) have emerged as a key enabling technology for the next generation of wireless systems, offering passive and low power control of the propagation environment. Conceptually, an RIS is a programmable metasurface composed of sub-wavelength unit cells that impose spatially varying reflection or transmission coefficients (phase, amplitude, and polarization), thereby engineering the boundary conditions experienced by an incident electromagnetic wave. This capability enables a wide range of functions, including passive beam steering, beam shaping, anomalous reflection and refraction, near field focusing, blockage mitigation, interference suppression, and coverage enhancement. Such functionalities are particularly valuable at mmWave and THz frequencies, where path loss and shadowing are severe. Beyond communications, RIS technology supports localization and sensing, enables joint communication and sensing (JCAS), and improves energy efficiency by avoiding additional active RF chains at the aperture. Com-

mon tuning mechanisms include semiconductor switches, varactors, MEMS actuators, and phase change materials, each offering different trade offs in loss, bandwidth, linearity, and power consumption.

This thesis investigated RIS unit cell and array design using semiconductor switches and MEMS actuators in order to achieve dual polarization control, wideband operation, and practical pathways toward fabrication and measurement. The work began with the development of a wideband dual polarized reflective unit cell that achieves two phase states with a stable $180^\circ \pm 2^\circ$ separation while sharing a single control signal for both polarizations, which significantly reduces biasing complexity. The unit cell was integrated into a reflectarray that was fabricated and experimentally characterized. Measurements demonstrated beam steering up to $\theta_0 = 50^\circ$, with a 1 dB gain bandwidth of 13.7% (12.2 GHz to 14 GHz), showing good agreement with simulation.

A wideband dual polarized transmissive 1-bit unit cell was then introduced for transmitarray applications. Its performance was verified through array level full wave simulations, demonstrating its suitability for refractive RIS implementations. Finally, a MEMS actuated reflective unit cell was developed to explore its potential in beam steering and RIS design. Measurements of the fabricated prototype showed a 260° reflection phase tuning range at 13.2 GHz. Array level simulations further verified the beam steering capability. MEMS actuators are particularly attractive for mmWave applications because of their low loss and high linearity, and because semiconductor technologies face limitations at higher frequency bands.

Contributions. The main contributions of this thesis are as follows:

1. A dual polarized wideband reflective unit cell with two robust 1 bit phase states and a simplified single line biasing network, experimentally validated through a fabricated

reflectarray [34], [97].

2. A dual polarized wideband transmissive unit cell suitable for refractive RIS applications, verified at array level through full wave simulations.

3. A MEMS actuated reflective unit cell that demonstrates large analog phase tuning and beam steering capability, indicating a path toward RIS design at mmWave frequency bands [36].

Collectively, these contributions advance RIS unit cell and array technologies toward practical, scalable, and polarization diverse implementations.

6.2 Future Work

While significant progress has been made, several extensions can further improve performance, practical implementation, and system readiness.

6.2.1 New unit cell structure design and development

There is always room to improve unit cell characteristics in terms of bandwidth, miniaturization, polarization diversity, and control system design. Therefore, employing different techniques and topologies in unit cell design is of great interest to achieve further improvements.

6.2.2 Higher order phase quantization and analog control

Extending the unit cell beyond 1 bit to 2 bit (four states) or higher resolution phase control can reduce quantization lobes, improve beam fidelity, and lower scan loss. Future work will focus on designing 2 bit unit cells that increase array efficiency, improve beam control accuracy, and remove the symmetric radiation pattern that appears when the array is used for anomalous reflection applications.

6.2.3 Fabrication and measurement of the transmitarray (RTA)

The proposed RTA has been validated in array simulation but has not yet been fabricated. A natural next step is to realize a prototype panel, including feed integration, mechanical stack up, and low loss bias routing, followed by anechoic chamber characterization (gain, efficiency, radiation patterns, polarization, and bandwidth) to verify agreement between simulation and measurement.

6.2.4 Scaling to larger apertures and anomalous reflection

Deploying the proposed unit cells in larger arrays for anomalous reflection applications will demonstrate their capability in a more robust way. Key aspects include the ability to change the direction of far field incident waves, the range of beam manipulation, and the achievable array bandwidth.

6.2.5 Fabrication of MEMS based arrays

Building on the MEMS unit cell concepts, full array fabrication should be pursued. Priorities include wafer level packaging, environmental sealing, bias network co design, and

reliability testing (lifetime cycling, shock and vibration, humidity, and temperature). Metrics such as actuation voltage, switching speed, linearity, and RF loss should be measured and balanced against control complexity.

6.2.6 Application driven demonstrations

Finally, system level demonstrations relevant to 6G, such as indoor coverage enhancement, vehicular links, satellite to terrestrial relays, and wireless power transfer, should be pursued using the proposed RIS, reflectarray, and transmitarray platforms. These studies can link array level performance to end to end system metrics such as link reliability, throughput, and latency.

References

[1] T. Mshvidobadze, "Evolution mobile wireless communication and lte networks," in *2012 6th International Conference on Application of Information and Communication Technologies (AICT)*, 2012, pp. 1–7.

[2] A. R. Mishra, *Fundamentals of Cellular Network Planning and Optimisation: 2G/2.5G/3G... Evolution to 4G*. John Wiley & Sons, Ltd, 2004. [Online]. Available: https://onlinelibrary.wiley.com/doi/book/10.1002/0470862696

[3] P. Popovski, K. F. Trillingsgaard, O. Simeone, and G. Durisi, "5g wireless network slicing for embb, urllc, and mmtc: A communication-theoretic view," *IEEE Access*, vol. 6, pp. 55 765–55 779, 2018.

[4] D. Lake, N. Wang, R. Tafazolli, and L. Samuel, "Softwarization of 5g networks–implications to open platforms and standardizations," *IEEE Access*, vol. 9, pp. 88 902–88 930, 2021.

[5] K. B. Letaief, W. Chen, Y. Shi, J. Zhang, and Y.-J. A. Zhang, "The roadmap to 6g: Ai empowered wireless networks," *IEEE Communications Magazine*, vol. 57, no. 8, pp. 84–90, 2019.

[6] M. Giordani, M. Polese, M. Mezzavilla, S. Rangan, and M. Zorzi, "Toward 6g networks: Use cases and technologies," *IEEE Communications Magazine*, vol. 58, no. 3, pp. 55–61, 2020.

[7] M. Z. Chowdhury, M. Shahjalal, S. Ahmed, and Y. M. Jang, "6g wireless communication systems: Applications, requirements, technologies, challenges, and research directions," *IEEE Open Journal of the Communications Society*, vol. 1, pp. 957–975, 2020.

[8] Samsung, "The next hyper-connected experience for all," Jul. 2020, [Online]. Available: https://cdn.codeground.org/nsr/downloads/researchareas/6G%20Vision.pdf.

[9] Q. Wu and R. Zhang, "Towards smart and reconfigurable environment: Intelligent reflecting surface aided wireless network," *IEEE Communications Magazine*, vol. 58, no. 1, pp. 106–112, 2020.

[10] S. Gong, X. Lu, D. T. Hoang, D. Niyato, L. Shu, D. I. Kim, and Y.-C. Liang, "Toward smart wireless communications via intelligent reflecting surfaces: A contemporary survey," *IEEE Communications Surveys Tutorials*, vol. 22, no. 4, pp. 2283–2314, 2020.

[11] Y. Liu, X. Liu, X. Mu, T. Hou, J. Xu, M. Di Renzo, and N. Al-Dhahir, "Reconfigurable intelligent surfaces: Principles and opportunities," *IEEE Communications Surveys Tutorials*, vol. 23, no. 3, pp. 1546–1577, 2021.

[12] E. Basar, M. Di Renzo, J. De Rosny, M. Debbah, M.-S. Alouini, and R. Zhang, "Wireless communications through reconfigurable intelligent surfaces," *IEEE Access*, vol. 7, pp. 116 753–116 773, 2019.

[13] Y.-C. Liang, R. Long, Q. Zhang, J. Chen, H. V. Cheng, and H. Guo, "Large intelligent surface/antennas (lisa): Making reflective radios smart," *Journal of Communications and Information Networks*, vol. 4, no. 2, pp. 40–50, 2019.

[14] M. Di Renzo, A. Zappone, M. Debbah, M.-S. Alouini, C. Yuen, J. de Rosny, and S. Tretyakov, "Smart radio environments empowered by reconfigurable intelligent surfaces: How it works, state of research, and the road ahead," *IEEE Journal on Selected Areas in Communications*, vol. 38, no. 11, pp. 2450–2525, 2020.

[15] N. Yu, P. Genevet, M. A. Kats, F. Aieta, J.-P. Tetienne, F. Capasso, and Z. Gaburro, "Light propagation with phase discontinuities: Generalized laws of reflection and refraction," *Science*, vol. 334, no. 6054, pp. 333–337, 2011.

[16] R. Leberer and W. Menzel, "A dual planar reflectarray with synthesized phase and amplitude distribution," *IEEE Transactions on Antennas and Propagation*, vol. 53, no. 11, pp. 3534–3539, 2005.

[17] F. Yang and Y. Rahmat-Samii, Eds., *Surface Electromagnetics: With Applications in Antenna, Microwave, and Optical Engineering*. Cambridge: Cambridge University Press, 2019.

[18] K. Achouri and C. Caloz, *Electromagnetic Metasurfaces: Theory and Applications*. Hoboken, NJ, USA: John Wiley & Sons, Inc., 2021.

[19] C. L. Holloway, E. F. Kuester, J. A. Gordon, J. O'Hara, J. Booth, and D. R. Smith, "An overview of the theory and applications of metasurfaces: The two-dimensional equivalents of metamaterials," *IEEE Antennas and Propagation Magazine*, vol. 54, no. 2, pp. 10–35, 2012.

[20] A. Li, S. Singh, and D. Sievenpiper, "Metasurfaces and their applications," *Nanophotonics*, vol. 7, no. 6, pp. 989–1011, 2018, https://www.degruyter.com/downloadpdf/journals/nanoph/7/6/article-p989.pdf. [Online]. Available: https://app.dimensions.ai/details/publication/pub.1104414761

[21] D. Sievenpiper, J. Schaffner, H. Song, R. Loo, and G. Tangonan, "Two-dimensional beam steering using an electrically tunable impedance surface," *IEEE Transactions on Antennas and Propagation*, vol. 51, no. 10, pp. 2713–2722, 2003.

[22] B. Zhu, J. Zhao, and Y. Feng, "Active impedance metasurface with full 360° reflection phase tuning," *Scientific Reports*, vol. 3, p. 3059, 2013.

[23] C. Della Giovampaola and N. Engheta, "Digital metamaterials," *Nature Materials*, vol. 13, no. 11, pp. 1115–1121, 2014. [Online]. Available: https://doi.org/10.1038/nmat4082

[24] T. J. Cui, M. Qi, X. Wan, J. Zhao, and Q. Cheng, "Coding metamaterials, digital metamaterials and programmable metamaterials," *Light: Science & Applications*, vol. 3, p. e218, 2014. [Online]. Available: https://doi.org/10.1038/lsa.2014.99

[25] C. Liaskos, S. Nie, A. Tsioliaridou, A. Pitsillides, S. Ioannidis, and I. Akyildiz, "A new wireless communication paradigm through software-controlled metasurfaces," *IEEE Communications Magazine*, vol. 56, no. 9, pp. 162–169, 2018.

[26] S. Li, F. Xu, X. Wan, T. J. Cui, and Y.-Q. Jin, "Programmable metasurface based on substrate-integrated waveguide for compact dynamic-pattern antenna," *IEEE Transactions on Antennas and Propagation*, vol. 69, no. 5, pp. 2958–2962, 2021.

[27] J. Huang and J. A. Encinar, *Reflectarray Antennas*. Hoboken, NJ, USA: Wiley, 2008.

[28] C. Huang, A. Zappone, G. C. Alexandropoulos, M. Debbah, and C. Yuen, "Reconfigurable intelligent surfaces for energy efficiency in wireless communication," *IEEE Transactions on Wireless Communications*, vol. 18, no. 8, pp. 4157–4170, 2019.

[29] P. Nayeri, F. Yang, and A. Z. Elsherbeni, *Reflectarray Antennas: Theory, Designs and Applications*. Hoboken, NJ: John Wiley & Sons, 2018.

[30] P. Aghabeyki, Y. Cai, G. Deng, Z.-H. Tan, and S. Zhang, "A dual-polarized reconfigurable reflectarray with a thin liquid crystal layer and 2-d beam scanning," *IEEE Transactions on Antennas and Propagation*, vol. 71, no. 4, pp. 3282–3293, Apr 2023.

[31] G. Perez-Palomino, M. Barba, J. A. Encinar, M. Freire, R. Gomez-Villanueva, F. Gonzalez, T. K. Fernandez, O. Quevedo-Teruel, F. G. Sanchez, and J. Rodriguez, "Design and demonstration of an electronically scanned reflectarray antenna at 100 ghz using multiresonant cells based on liquid crystals," *IEEE Transactions on Antennas and Propagation*, vol. 63, no. 8, pp. 3722–3727, Aug 2015.

[32] S. V. Hum, M. Okoniewski, and R. J. Davies, "Modeling and design of electronically tunable reflectarrays," *IEEE Transactions on Antennas and Propagation*, vol. 55, no. 8, pp. 2200–2210, Aug 2007.

[33] H. Kamoda, T. Iwasaki, J. Tsumochi, T. Kuki, and O. Hashimoto, "60-ghz electronically reconfigurable large reflectarray using single-bit phase shifters," *IEEE Transactions on Antennas and Propagation*, vol. 59, no. 7, pp. 2524–2531, 2011.

[34] J. Tayebpour and R. R. Mansour, "A wideband dual-polarized 1-bit unit cell for reconfigurable intelligent surface applications," in *2024 18th European Conference on Antennas and Propagation (EuCAP)*, 2024, pp. 1–5.

[35] C.-C. Cheng, B. Lakshminarayanan, and A. Abbaspour-Tamijani, "A programmable lens-array antenna with monolithically integrated mems switches," *IEEE Transactions on Microwave Theory and Techniques*, vol. 57, no. 8, pp. 1874–1884, Aug 2009.

[36] J. Tayebpour and R. R. Mansour, "Reconfigurable unit cell design using mems actuator for beam-steering applications," *IEEE Transactions on Antennas and Propagation*, vol. 73, no. 3, pp. 1346–1354, 2025.

[37] S. V. Hum and J. Perruisseau-Carrier, "Reconfigurable reflectarrays and array lenses for dynamic antenna beam control: A review," *IEEE Transactions on Antennas and Propagation*, vol. 62, no. 1, pp. 183–198, 2014.

[38] M. Riel and J.-J. Laurin, "Design of an electronically beam scanning reflectarray using aperture-coupled elements," *IEEE Transactions on Antennas and Propagation*, vol. 55, no. 5, pp. 1260–1266, 2007.

[39] H. Yang, F. Yang, S. Xu, M. Li, X. Cao, J. Gao, and Y. Zheng, "A study of phase quantization effects for reconfigurable reflectarray antennas," *IEEE Antennas and Wireless Propagation Letters*, vol. 16, pp. 302–305, 2017.

[40] B. Wu, A. Sutinjo, M. E. Potter, and M. Okoniewski, "On the selection of the number of bits to control a dynamic digital mems reflectarray," *IEEE Antennas and Wireless Propagation Letters*, vol. 7, pp. 183–186, 2008.

[41] J. Han, L. Li, G. Liu, Z. Wu, and Y. Shi, "A wideband 1 bit 12 $\times$ 12 reconfigurable beam-scanning reflectarray: Design, fabrication, and measurement," *IEEE Antennas and Wireless Propagation Letters*, vol. 18, no. 6, pp. 1268–1272, 2019.

[42] S.-G. Zhou, G. Zhao, H. Xu, C.-W. Luo, J.-Q. Sun, G.-T. Chen, and Y.-C. Jiao, "A wideband 1-bit reconfigurable reflectarray antenna at ku-band," *IEEE Antennas and Wireless Propagation Letters*, vol. 21, no. 3, pp. 566–570, 2022.

[43] H. Rajagopalan, Y. Rahmat-Samii, and W. A. Imbriale, "Rf mems actuated reconfigurable reflectarray patch-slot element," *IEEE Transactions on Antennas and Propagation*, vol. 56, no. 12, pp. 3689–3699, 2008.

[44] T. Debogovic and J. Perruisseau-Carrier, "Low loss mems-reconfigurable 1-bit reflectarray cell with dual-linear polarization," *IEEE Transactions on Antennas and Propagation*, vol. 62, no. 10, pp. 5055–5060, 2014.

[45] Q. Zhang, M. Zhang, X. Shi, S. Gao, Q. Luo, L. Chen, J. Wan, and X. Wang, "A low-profile beam-steering reflectarray with integrated leaky-wave feed and 2-bit phase resolution for ka-band satcom," *IEEE Transactions on Antennas and Propagation*, vol. 70, no. 3, pp. 1884–1894, 2022.

[46] Y. Yin, C. Deng, X. Cao, Y. Hao, Y. Hou, H. Xu, and K. Sarabandi, "Design of a 2-bit dual-polarized reconfigurable reflectarray with high aperture efficiency," *IEEE Transactions on Antennas and Propagation*, vol. 72, no. 1, pp. 542–552, 2024.

[47] Q. Chen, "Reflectarray development for improving nlos radio channel," in *2013 Asia-Pacific Microwave Conference Proceedings (APMC)*, 2013, pp. 654–656.

[48] X. Pei, H. Yin, L. Tan, L. Cao, Z. Li, K. Wang, K. Zhang, and E. Björnson, "Ris-aided wireless communications: Prototyping, adaptive beamforming, and indoor/outdoor field trials," *IEEE Transactions on Communications*, vol. 69, no. 12, pp. 8627–8640, 2021.

[49] A. Araghi, M. Khalily, M. Safaei, A. Bagheri, V. Singh, F. Wang, and R. Tafazolli, "Reconfigurable intelligent surface (ris) in the sub-6 ghz band: Design, implementation, and real-world demonstration," *IEEE Access*, vol. 10, pp. 2646–2655, 2022.

[50] NTT DOCOMO. (2020, Jan.) Docomo conducts world's first successful trial of transparent dynamic metasurface. [Online; accessed 2025-08-09]. [Online]. Available: https://www.nttdocomo.co.jp/english/info/media_center/pr/2020/0117_00.html

[51] Q. Ma, Q. Xiao, Q. R. Hong, X. Gao, V. Galdi, and T. J. Cui, "Digital coding metasurfaces: From theory to applications," *IEEE Antennas and Propagation Magazine*, vol. 64, no. 4, pp. 96–109, 2022.

[52] G. C. Trichopoulos, P. Theofanopoulos, B. Kashyap, A. Shekhawat, A. Modi, T. Osman, S. Kumar, A. Sengar, A. Chang, and A. Alkhateeb, "Design and evaluation of reconfigurable intelligent surfaces in real-world environment," *IEEE Open Journal of the Communications Society*, vol. 3, pp. 462–474, 2022.

[53] H. Yang, X. Cao, F. Yang, J. Gao, S. Xu, M. Li, X. Chen, and Y. Zhao, "A programmable metasurface with dynamic polarization, scattering and focusing control," *Scientific Reports*, vol. 6, p. 35692, 2016. [Online]. Available: https://doi.org/10.1038/srep35692

[54] X. Wan, M. Qi, T. Chen, and T. J. Cui, "Field-programmable beam reconfiguring based on digitally-controlled coding metasurface," *Scientific Reports*, vol. 6, p. 20663, 2016. [Online]. Available: https://doi.org/10.1038/srep20663

[55] C. Huang, B. Sun, W. Pan, X. Ma, T. J. Cui, and Q. Zheng, "Dynamical beam manipulation based on 2-bit digitally-controlled coding metasurface," *Scientific Reports*, vol. 7, p. 42302, 2017. [Online]. Available: https://doi.org/10.1038/srep42302

[56] N. Zhang, K. Chen, J. Zhao, Q. Hu, K. Tang, J. Zhao, T. Jiang, and Y. Feng, "A dual-polarized reconfigurable reflectarray antenna based on dual-channel programmable metasurface," *IEEE Transactions on Antennas and Propagation*, vol. 70, no. 9, pp. 7403–7412, 2022.

[57] H. Yang, F. Yang, S. Xu, Y. Mao, M. Li, X. Cao, and J. Gao, "A 1-bit 10×10 reconfigurable reflectarray antenna: Design, optimization, and experiment," *IEEE Transactions on Antennas and Propagation*, vol. 64, no. 6, pp. 2246–2254, 2016.

[58] S. Liu, T. J. Cui, L. Zhang, Q. Xu, Q. Wang, X. Wan, J. Q. Gu *et al.*, "Convolution operations on coding metasurface to reach flexible and continuous controls of terahertz beams," *Advanced Science*, vol. 3, no. 10, p. 1600156, 2016.

[59] C. A. Balanis, *Antenna Theory: Analysis and Design*, 3rd ed. Hoboken, NJ: John Wiley & Sons, 2005, ch. 12, pp. 701–715.

[60] J. Yin, Q. Wu, Q. Lou, H. Wang, Z. N. Chen, and W. Hong, "Single-beam 1 bit reflective metasurface using prephased unit cells for normally incident plane waves," *IEEE Transactions on Antennas and Propagation*, vol. 68, no. 7, pp. 5496–5504, 2020.

[61] D. Pozar, "Bandwidth of reflectarrays," *Electronics Letters*, vol. 39, pp. 1490–1491, 2003. [Online]. Available: https://digital-library.theiet.org/doi/abs/10.1049/el%3A20030990

[62] B. J. Xiang, X. Dai, and K.-M. Luk, "A wideband low-cost reconfigurable reflectarray antenna with 1-bit resolution," *IEEE Transactions on Antennas and Propagation*, vol. 70, no. 9, pp. 7439–7447, 2022.

[63] H. Luyen, Z. Zhang, J. H. Booske, and N. Behdad, "Wideband, beam-steerable reflectarray antennas exploiting electronically reconfigurable polarization-rotating phase

shifters," *IEEE Transactions on Antennas and Propagation*, vol. 70, no. 6, pp. 4414–4425, 2022.

[64] H. Yang, F. Yang, S. Xu, M. Li, X. Cao, and J. Gao, "A 1-bit multipolarization reflectarray element for reconfigurable large-aperture antennas," *IEEE Antennas and Wireless Propagation Letters*, vol. 16, pp. 581–584, 2017.

[65] N. Zhang, K. Chen, J. Zhao, Q. Hu, K. Tang, J. Zhao, T. Jiang, and Y. Feng, "A dual-polarized reconfigurable reflectarray antenna based on dual-channel programmable metasurface," *IEEE Transactions on Antennas and Propagation*, vol. 70, no. 9, pp. 7403–7412, 2022.

[66] B. Xi, Y. Xiao, K. Zhu, Y. Liu, H. Sun, and Z. Chen, "1-bit wideband reconfigurable reflectarray design in ku-band," *IEEE Access*, vol. 10, pp. 4340–4348, 2022.

[67] M.-T. Zhang, S. Gao, Y.-C. Jiao, J.-X. Wan, B.-N. Tian, C.-B. Wu, and A.-J. Farrall, "Design of novel reconfigurable reflectarrays with single-bit phase resolution for ku-band satellite antenna applications," *IEEE Transactions on Antennas and Propagation*, vol. 64, no. 5, pp. 1634–1641, 2016.

[68] P. Li, K. Lau, and K. Luk, "A study of the wide-band l-probe fed planar patch antenna mounted on a cylindrical or conical surface," *IEEE Transactions on Antennas and Propagation*, vol. 53, no. 10, pp. 3385–3389, 2005.

[69] A. Yu, F. Yang, A. Z. Elsherbeni, J. Huang, and Y. Rahmat-Samii, "Aperture efficiency analysis of reflectarray antennas," *Microwave and Optical Technology Letters*, vol. 52, no. 2, pp. 364–372, Feb 2010. [Online]. Available: https://onlinelibrary.wiley.com/doi/abs/10.1002/mop.24949

[70] J. R. Reis, M. Vala, and R. F. S. Caldeirinha, "Review paper on transmitarray antennas," *IEEE Access*, vol. 7, pp. 94 171–94 188, 2019.

[71] A. H. Abdelrahman, F. Yang, A. Z. Elsherbeni, and P. Nayeri, *Analysis and Design of Transmitarray Antennas*, ser. Synthesis Lectures on Antennas. Springer Cham, 2017. [Online]. Available: https://doi.org/10.1007/978-3-031-01541-0

[72] A. Clemente, L. Dussopt, R. Sauleau, P. Potier, and P. Pouliguen, "Wideband 400-element electronically reconfigurable transmitarray in x band," *IEEE Transactions on Antennas and Propagation*, vol. 61, no. 10, pp. 5017–5027, 2013.

[73] Y. Xiao, B. Xi, M. Xiang, F. Yang, and Z. Chen, "1-bit wideband reconfigurable transmitarray unit cell based on pin diodes in ku-band," *IEEE Antennas and Wireless Propagation Letters*, vol. 20, no. 10, pp. 1908–1912, 2021.

[74] X. Dai, G.-B. Wu, and K.-M. Luk, "A wideband low-profile reconfigurable transmitarray using magnetoelectric dipole elements," *IEEE Transactions on Antennas and Propagation*, vol. 70, no. 9, pp. 8008–8019, 2022.

[75] I. Munina, P. Turalchuk, A. Verevkin, V. Kirillov, D. Zelenchuk, and A. Shitvov, "A study of c-band 1-bit reconfigurable dual-polarized transmitarray," in *2019 13th European Conference on Antennas and Propagation (EuCAP)*, 2019, pp. 1–5.

[76] W. Pan, C. Huang, X. Ma, B. Jiang, and X. Luo, "A dual linearly polarized transmitarray element with 1-bit phase resolution in x-band," *IEEE Antennas and Wireless Propagation Letters*, vol. 14, pp. 167–170, 2015.

[77] Y. Wang, S. Xu, F. Yang, and D. H. Werner, "1 bit dual-linear polarized reconfigurable transmitarray antenna using asymmetric dipole elements with parasitic bypass

dipoles," *IEEE Transactions on Antennas and Propagation*, vol. 69, no. 2, pp. 1188–1192, 2021.

[78] K. Luk and H. Wong, "A new wideband unidirectional antenna element," *Int J Microwave Opt Technol*, vol. 1, 01 2006.

[79] K.-M. Luk and B. Wu, "The magnetoelectric dipole—a wideband antenna for base stations in mobile communications," *Proceedings of the IEEE*, vol. 100, no. 7, pp. 2297–2307, 2012.

[80] G. M. Rebeiz, K. Entesari, I. C. Reines, S.-j. Park, M. A. El-tanani, A. Grichener, and A. R. Brown, "Tuning in to rf mems," *IEEE Microwave Magazine*, vol. 10, no. 6, pp. 55–72, 2009.

[81] O. Bayraktar, O. A. Civi, and T. Akin, "Beam switching reflectarray monolithically integrated with rf mems switches," *IEEE Transactions on Antennas and Propagation*, vol. 60, no. 2, pp. 854–862, 2012.

[82] M. Mavridou and A. P. Feresidis, "Dynamically reconfigurable high impedance and frequency selective metasurfaces using piezoelectric actuators," *IEEE Transactions on Antennas and Propagation*, vol. 64, no. 12, pp. 5190–5197, 2016.

[83] L. Lu, C. Liu, X. Liu, and Y. Huang, "A mechanical reconfigurable reflectarray based on magnetic force tuning," *IEEE Antennas and Wireless Propagation Letters*, vol. 23, no. 2, pp. 528–532, 2024.

[84] X. Yang, S. Xu, F. Yang, M. Li, H. Fang, Y. Hou, S. Jiang, and L. Liu, "A mechanically reconfigurable reflectarray with slotted patches of tunable height," *IEEE Antennas and Wireless Propagation Letters*, vol. 17, no. 4, pp. 555–558, 2018.

[85] P. Pitchappa, A. Kumar, R. Singh, C. Lee, and N. Wang, "Terahertz mems metadevices," *Journal of Micromechanics and Microengineering*, vol. 31, no. 11, p. 113001, Nov. 2021.

[86] X. Liu *et al.*, "Terahertz beam steering concept based on a mems-reconfigurable reflection grating," *Sensors*, vol. 20, no. 10, p. 2874, May 2020.

[87] J. Gianvittorio and Y. Rahmat-Samii, "Reconfigurable patch antennas for steerable reflectarray applications," *IEEE Transactions on Antennas and Propagation*, vol. 54, no. 5, pp. 1388–1392, 2006.

[88] M. Sterner, D. Chicherin, A. Raisenen, G. Stemme, and J. Oberhammer, "Rf mems high-impedance tuneable metamaterials for millimeter-wave beam steering," in *2009 IEEE 22nd International Conference on Micro Electro Mechanical Systems*, 2009, pp. 896–899.

[89] D. Schurig, J. J. Mock, and D. R. Smith, "Electric-field-coupled resonators for negative permittivity metamaterials," *Applied Physics Letters*, vol. 88, no. 4, p. 041109, 01 2006. [Online]. Available: https://doi.org/10.1063/1.2166681

[90] T. H. Hand, J. Gollub, S. Sajuyigbe, D. R. Smith, and S. A. Cummer, "Characterization of complementary electric field coupled resonant surfaces," *Applied Physics Letters*, vol. 93, no. 21, p. 212504, 11 2008. [Online]. Available: https://doi.org/10.1063/1.3037215

[91] T. H. Hand and S. A. Cummer, "Reconfigurable reflectarray using addressable metamaterials," *IEEE Antennas and Wireless Propagation Letters*, vol. 9, pp. 70–74, 2010.

[92] R. Awadallah, D. Shrekenhamer, R. Schmid, A. Mills, and J. Nanzer, "An x-band binary reflectarray with sub-wavelength elc resonator elements," in *2017 IEEE In-*

ternational Symposium on Antennas and Propagation USNC/URSI National Radio Science Meeting, 2017, pp. 2075–2076.

[93] R. Marin, "Investigations on liquid crystal reconfigurable unit cells for mm-wave reflect arrays," Ph.D. dissertation, Technische Universität Darmstadt, Darmstadt, Germany, 2008.

[94] S. Targonski and D. Pozar, "Analysis and design of a microstrip reflectarray using patches of variable size," in *Proceedings of IEEE Antennas and Propagation Society International Symposium and URSI National Radio Science Meeting*, vol. 3, 1994, pp. 1820–1823 vol.3.

[95] A. Cowen, B. Hardy, R. Mahadevan, and S. Wilcenski, *PolyMUMPs Design Handbook*, MEMSCAP Inc., 2005, revision 11.0.

[96] W. D. Yan and R. R. Mansour, "Tunable dielectric resonator bandpass filter with embedded mems tuning elements," *IEEE Transactions on Microwave Theory and Techniques*, vol. 55, no. 1, pp. 154–160, 2007.

[97] J. Tayebpour and R. R. Mansour, "A wideband dual-polarized reconfigurable reflectarray using polarization rotation technique," *IEEE Access*, vol. 13, pp. 106 906–106 915, 2025.